Cold Neutral Atoms in Optical Lattices

by

Rui Zhang

A dissertation submitted in partial fulfillment
of the requirements for the degree of
Doctor of Philosophy
(Physics)
in The University of Michigan
2008

Doctoral Committee:

Professor Georg A. Raithel, Chair
Professor Paul R. Berman
Professor Duncan G. Steel
Associate Professor Luming Duan
Assistant Professor Aaron Edward Leanhardt

To my wife and my parents

ACKNOWLEDGEMENTS

I would like to thank Professor Georg Raithel for his wonderful advices and instructions throughout my Ph.D years here in Michigan. His wide knowledge and enormous enthusiasm in this amazing field of laser cooling and neutral atom trapping have impressed me ever since my first day in the lab. Especially when we came across some problems or failed to understand certain phenomena in the lab, he always came down to help and gave us correct answers and right directions. I am also grateful to his support during the time when I had a visa issue and had to stay in China for almost one year. His decision to keep me as a member of the group and provide me with the financial support (together with the department) certainly played a big role in solving my visa issue. I will always remember this.

When I started my first project in the lab, I also worked with professor Paul Berman on theoretical calculations. He is such an inspiring instructor that any profound physical concepts can be explained in a simple way. I really enjoyed working with him and taking his Quantum Optics class.

There are so many students and postdocs whom I have interacted with in the lab and want to say "Thank you". I am probably not able to describe specific reasons for my gratefulness concerning each one of them. However, I do want to mention their names at least: Brynle Barrett, Katie Crimmins, Jae-Hoon Choi, Tara Cubel, David Feldbaum, Jeff Guest, Cornelius Hempel, Eberhart Hansis, Brenton Knuffman, Huijun Kong, Natalya Morrow, Rahul Mhaskar, Spencer Olson, Eric Paradis, Alex

Povilus, Aaron Reinhard, Rachel Sapiro, Kevin Teo, Mallory Traxler, Varun Vaidya, Kelly C. Younge, Alisa Walz-Flannigan and Xuhuai Zhang.

In my first couple of months in the lab, I received enormous help from Kevin, Tara, Jeff, Alisa, Spencer and David. They are fun and friendly persons and made me feel comfortable working in the lab. After I came back from China, I am so fortunate to have Natalya working in the same project as me. I learned so many things from her that I may not be able to list all of them in two pages. When we started the BEC project, Rachel joined the group. She is a big reason why we can achieve the BEC in one and half years. I wish her best luck in future work regarding the BEC.

Our group always has lots of members and we have a good time together. Aaron, Brenton, Rahul, and I joined the group about the same time. In four years, we not only have fun working together and learning from each other, but also enjoy talking to each other in many non-physics subjects, especially in sports. Later on, Eric joined the group. Our conversations started to cover broader range, such as hockey. I want to thank all these guys for making the life in the lab much more entertaining.

Recently, Kelly, Mallory, Varun, and Andrew became new members of our group. They are all nice people to work with. I wish them best luck in the future. I also want to thank Rachel, Eric, and Kelly for proof-reading this thesis. I really appreciate it!

Life is not easy for foreign students because they have to study at a place far away from their families and old friends. Fortunately, I made lots of friends the first day I came to Ann Arbor. I want to thank Bin, Hao, Hailing, Ming, Meng, Song, Xiaodong, and their families. Without them, all these Chinese holidays in my five years here in Ann Arbor would be really lonely.

At last I want to thank my families, especially my parents and my wife, for their

support throughout all these years. What I appreciate most about my parents is how they raised me and educated me. They never asked anything from me. They never set any goals for me. They never put any pressure on me. All they want is that I try my best and do what I enjoy. That is one of the most important reasons why I am what I am today! My wife and I were high school classmates. We spent four years together in the same college and got engaged one year after our graduation. Her support is a huge part of my decision to come to U.S.A to pursue my Ph.D degree. Even though she is in China, I can always seek encouragement and comfort from her. Thank you! My lover!

TABLE OF CONTENTS

LIST OF FIGURES

Figure

LIST OF APPENDICES

Appendix

ABSTRACT

In this thesis, I study the properties of cold neutral atoms, including Bose-Einstein condensates (BEC), inside periodic light-shift potentials created by optical lattices. In the first part, a new optical-lattice scheme, employing Raman transitions, hereafter referred to as a Raman Optical Lattice (ROL), is investigated. This optical lattice possesses a novel sub-Doppler cooling mechanism and a reduced periodicity. Both theoretical and experimental results confirm these two characteristics of the ROL. In the second half of the thesis, instead of thermal atoms, optical lattices are loaded with condensate atoms. Our BEC apparatus and the procedure towards forming a BEC are described in detail. After the achievement of the BEC, a 1D far-detuned optical lattice is applied to the BEC. A number of phenomena are observed, including Kapitza-Dirac diffraction, thermal atom interference, atom interferometry, Bloch oscillations, and a superfluid to Mott-insulator transition. Finally a brief discussion about future work is given.

CHAPTER I

Introduction

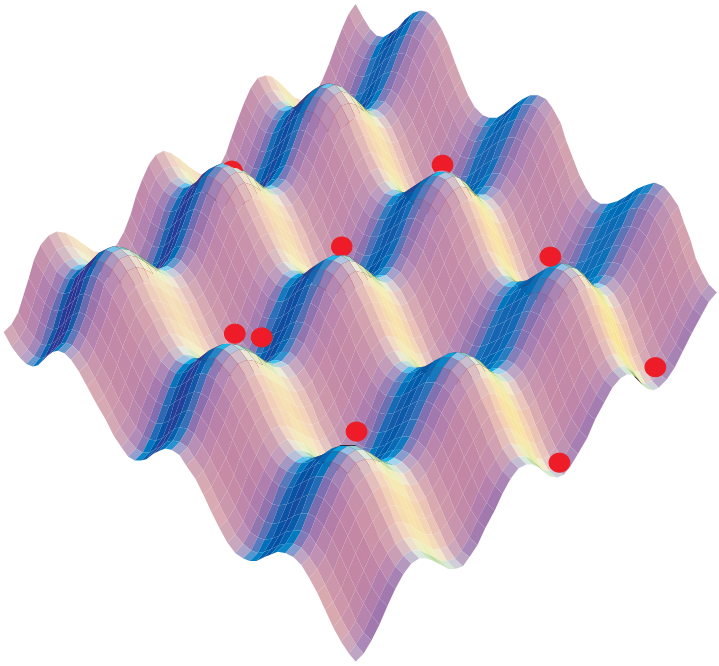

Figure 1.1: Potential wells of a 2-D optical lattice

An optical lattice is a light-shift potential formed by the interference of several laser beams. The interference leads to a perfect periodic structure of potential wells where cold atoms can localize, as shown in Fig. 1.1. Optical lattices display many characteristics associated with solid state crystals, and additionally possess other unique properties. Unlike most solid state crystals, the parameters of optical lattices

are much easier to vary and manipulate experimentally, by changing the light field parameters and applying external magnetic fields. In addition, atoms in optical lattices typically have a much longer coherence time (order of μs) compared with solid state systems where the coherence time is of the order of ns. These unique properties make the optical lattice an excellent alternative in studying many solid state phenomena. Since the first experimental realization in 1987 [1], optical lattices have been used in a number of such experiments including Bragg scattering [2, 3], Bloch oscillations [4], Wannier-Stark ladders [5], wavepacket revivals [6], and tunneling [7, 8]. Applications of optical lattices in quantum information processing have also been proposed [9–11]. More recently, applying optical lattices to Bose-Einstein condensates has led to the observation of a remarkable quantum phenomenon: the superfluid to Mott-insulator transition [12]. In applied fields, such as nano-lithography [13], optical lattices are also of high interest. Although direct deposition is not practical, alkali atoms, normally used in the optical lattice experiments, can be applied in structured arrays on a surface treated with photo-resist, *i.e.*, we can use atoms to develop a desired pattern using lithographic methods.

The origin of the optical lattice comes from the fact that the interaction of a light field with an atom shifts the energy levels of the atom's internal states. The interference of two or more fields can create a spatial modulation of the energy shift, which forms an optical lattice potential. More detailed discussion is presented in the first section of this chapter. In the second section, the layout of the thesis is given, including our motivations for studying a new type of optical lattice and Bose-Einstein condensates in optical lattices.

1.1 Light-shift Potential

The Hamiltonian for an atom in a laser field can be written as $H(t) = H_o + H'(t)$, where H_o represents a field-free, time-independent atomic Hamiltonian and H' describes the interaction with the laser field. Consider eigenstates of H_o, ψ_n, with eigenvalues $E_n \equiv \hbar\omega_n$, then $H_o\psi_n = E_n\psi_n$. Since the eigenstates ψ_n form a complete set, the solution to the Schrödinger equation

$$H(t)\Psi(\vec{r},t) = i\hbar\frac{\partial\Psi(\vec{r},t)}{\partial t} \tag{1.1}$$

can be expanded in terms of ψ_n:

$$\Psi(\vec{r},t) = \sum_n a_n(t)\psi_n(\vec{r})e^{-i\omega_n t}\,, \tag{1.2}$$

where $\vec{r}$ is the electron position. Substituting Eq. 1.2 back into the Schrödinger equation, we get

$$H(t)\Psi(\vec{r},t) = i\hbar(\frac{\partial}{\partial t})\sum_n a_n(t)\psi_n(\vec{r})e^{-i\omega_n t}\,. \tag{1.3}$$

Eq. 1.3 can be simplified by multiplying ψ_n^* on the left and integrating over the spatial coordinate $\vec{r}$. The final equations take the form

$$i\hbar(\frac{da_m}{dt}) = \sum_n a_n(t)H'_{mn}(t)e^{-i\omega_{mn}t}\,. \tag{1.4}$$

The field interaction Hamiltonian $H'(t)$ can be expressed as

$$H'(t) = -e\vec{\varepsilon}(\vec{r},t)\cdot\vec{r} \tag{1.5}$$

where $\vec{\varepsilon}(\vec{r},t)$ is the electric field operator of the laser field. For a plane wave traveling in the z direction,

$$\vec{\varepsilon}(\vec{r},t) = E_o\hat{\epsilon}\cos(kz-\omega_l t)\,, \tag{1.6}$$

In matrix form, the Hamiltonian $H'(t)$ is written as

$$H'(t) = 2\hbar \begin{pmatrix} 0 & \chi\cos(kz-\omega_l t) \\ \chi\cos(kz-\omega_l t) & 0 \end{pmatrix}, \tag{1.7}$$

where the Rabi frequency χ, defined by

$$\chi \equiv \frac{-eE_o}{\hbar}\langle e|r|g\rangle \tag{1.8}$$

is assumed to be real. Note that the electric dipole approximation is made here to neglect the variation of $\vec{\varepsilon}(\vec{r},t)$ over the wavefunction region of the atomic states $|g\rangle, |e\rangle$. With this matrix form of the Hamiltonian, Eqs. 1.4 becomes

$$i\hbar\frac{da_g(t)}{dt} = 2\hbar a_e \chi\cos(kz-\omega_l t)e^{-i\omega_a t} \tag{1.9a}$$

$$i\hbar\frac{da_e(t)}{dt} = 2\hbar a_g \chi\cos(kz-\omega_l t)e^{i\omega_a t} \tag{1.9b}$$

where $\omega_a = \omega_e - \omega_g$ is the atomic resonance frequency. Under the rotating wave approximation (RWA), fast oscillating terms, $e^{\pm i(\omega_a+\omega l)t}$, are to be neglected. Equations. 1.9 then become

$$i\hbar\frac{da_g(t)}{dt} = \hbar a_{e(t)}\chi e^{i\Delta t} \tag{1.10a}$$

$$i\hbar\frac{da_e(t)}{dt} = \hbar a_g(t)\chi e^{-i\Delta t} \tag{1.10b}$$

Here Δ is the field detuning from the atomic resonance frequency, $\Delta = \omega_l - \omega_a$. In a rotating frame where

$$c_g(t) \equiv a_g(t) \tag{1.11a}$$

$$c_e(t) \equiv a_e(t)e^{i\Delta t}, \tag{1.11b}$$

Eqs. 1.10 can be further simplified as

$$i\hbar\frac{dc_g(t)}{dt} = c_e(t)\hbar\chi \tag{1.12a}$$

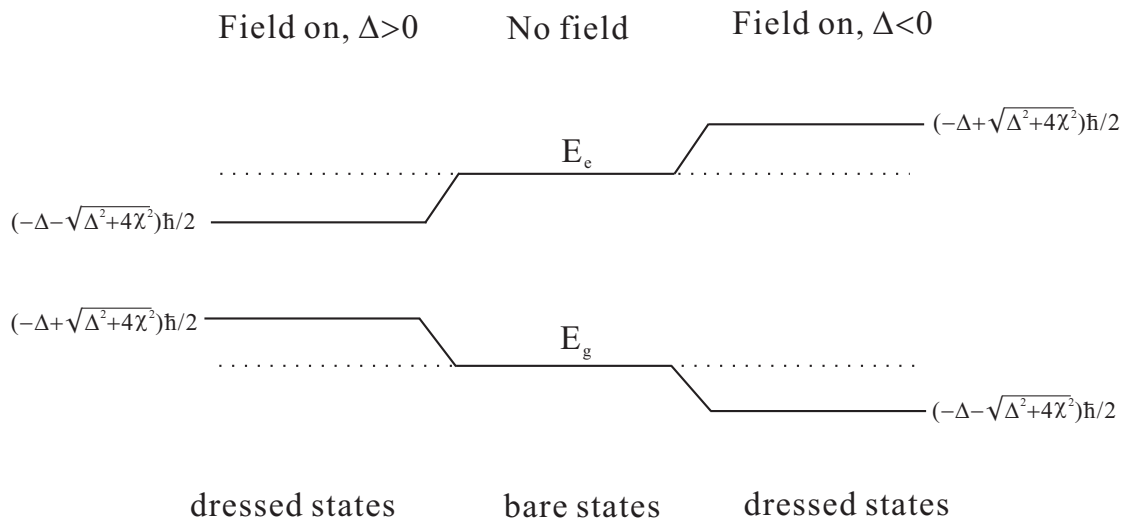

Figure 1.2: The energy shifts caused by the atom-light interaction for blue-detuned ($\Delta > 0$) and red-detuned ($\Delta < 0$) light.

$$i\hbar\frac{dc_e(t)}{dt} = c_g(t)\hbar\chi - c_e(t)\hbar\Delta\,. \tag{1.12b}$$

The full Hamiltonian is now expressed in a matrix form by

$$H = \hbar\begin{pmatrix} 0 & \chi \\ \chi & -\Delta \end{pmatrix}\,. \tag{1.13}$$

The eigenvalues of this new Hamiltonian are calculated to be

$$E_\pm = \frac{\hbar}{2}(-\Delta \pm \sqrt{\Delta^2 + 4\chi^2})\,. \tag{1.14}$$

The corresponding new eigenstates are called semi-classical dressed states. Note that in the original interaction representation before diagonalizing the new Hamiltonian, the ground state has 0 energy, $E_g = 0$, and the excited state has an energy of $-\hbar\Delta$, $E_e = -\hbar\Delta$. When the light field is turned on, the value of the new excited state energy depends on the sign of the detuning Δ. (The new excited state energy is always the one that is closer to the original excited state energy $-\Delta$.) For $\Delta < 0$, $E_{e'} = E_+$, $E_{g'} = E_-$; For $\Delta > 0$, $E_{e'} = E_-$, $E_{g'} = E_+$, as show in Fig. 1.2.

In the limit where $|\Delta| \gg \chi$ (the rest of this thesis deals with this limit except

otherwise mentioned), the energies are shifted by

$$\begin{aligned} E_{g'g} &\equiv E_{g'} - E_g = \frac{\hbar\chi^2}{\Delta} \\ E_{e'e} &\equiv E_{e'} - E_e = -\frac{\hbar\chi^2}{\Delta}\,. \end{aligned} \tag{1.15}$$

Since χ^2 is proportional to the light intensity, this energy shift is called light shift, also known as the AC Stark shift. As indicated by Eqs. 1.15, the energy separation between the ground and excited states becomes larger when the light field is red-detuned, $\Delta < 0$, and smaller when blue-detuned, $\Delta > 0$. When another counter-propagating light field, with the same frequency and polarization, is added to this system, a standing wave is formed. The light intensity is no longer homogeneous spatially. Instead it is periodically modulated with a period of $\lambda/2$, where λ is the wavelength of the light. As a result, the light shift potential of the atom is also spatially modulated with the same period. This periodic light shift potential is also called an optical lattice.

When it comes to real atoms, this simple two-level model does not work since atoms have multiple levels in the ground and excited states. Transitions between the ground and excited states, in general, involve many sub-levels and become much more complicated. Nevertheless, the basic physics of optical lattices is as illustrated here.

1.2 Motivations and Thesis Outline

The importance of optical lattices lies in their ability to create a perfect periodic structure. As discussed in the previous section, traditionally this structure has a period of half the wavelength of the laser beams underlying the optical lattice. Since in some applications, like wave-packet tunneling and atom-lithography, a smaller period optical lattice may be more useful, an important question arises: can this pe-

riod be reduced? In our recent work [14], we proposed a new optical lattice geometry based on the two-photon Raman transition to achieve a $\lambda/4$ period optical lattice. We refer to this optical lattice as a "Raman Optical Lattice" (ROL). In addition to its reduced periodicity, the ROL also gives rise to a new type of sub-Doppler laser cooling, which has never previously been explored. In Chapter II, I will first present the theoretical model of the ROL to show the origin of the reduced periodicity. Then the sub-Doppler cooling effect will be verified from two approaches: semi-classical calculations and Quantum Monte Carlo wavefunction simulations (QMCWF). The experimental realization of the ROL will be described in Chapter III, which includes demonstrations of both the sub-Doppler laser cooling and the $\lambda/4$ periodicity of the ROL.

In the ROL experiment, the lattice is applied to atoms in a magneto-optical trap (MOT). Even after an additional molasses cooling, the atoms only reach a temperature of around 50 μK. Recently, more and more lattice experiments switch to a much colder and denser atomic ensemble: Bose-Einstein Condensate (BEC). The BEC is a sample of bosonic atoms that are cooled to such a low temperature that they all occupy the same lowest quantum state and display macroscopic quantum properties. The combination of BECs with optical lattices leads to an exciting new frontier of physics research, which appeals to both atomic and condensed matter physicists. Therefore, after the ROL experiment, we started our BEC project. In Chapter IV, I will describe our achievement of the BEC in a dilute ^{87}Rb gas. Observations of many unique quantum phenomena involving BECs in optical lattices will be presented in Chapter V.

CHAPTER II

Theory of the Raman Optical Lattice (ROL)

As discussed in the previous chapter, the basic periodicity of an optical lattice produced by a laser field having wavelength λ is $\lambda/2$. However, recently a number of papers have been published on the possibility to reduce this basic periodicity to $\lambda/4$ or smaller [15–18] by modifying the atom-field geometry. In particular, we point out that sub-Doppler cooling occurs for one such scheme [14], which we refer to as a Raman Optical Lattice (ROL). In this chapter, the ROL geometry will be explored theoretically.

2.1 Theoretical Model of the Raman Optical Lattice

The basic transition diagram of the ROL is shown schematically in Fig. 2.1. Two pairs of counter-propagating laser fields are involved in driving two-photon Raman transitions between ground states 1 and 2 through excited state 3. Consider first the pair of fields E_1 and E_2, which have propagation vectors $\mathbf{k}_1 = -\mathbf{k}_2 = \mathbf{k} = (2\pi/\lambda)\hat{\mathbf{z}}$. An atom initially in state 1 can absorb one photon from field E_1, re-emit a photon into field E_2, and end up in state 2. In this process, the atom receives a momentum kick equal to $2\hbar\mathbf{k}$. Thus, the transition between states 1 and 2 can be considered to be driven by an effective Raman field with a propagation vector $2\mathbf{k}$. The fields E_3 and E_4 couple the two states in a similar manner but have directions opposite to those

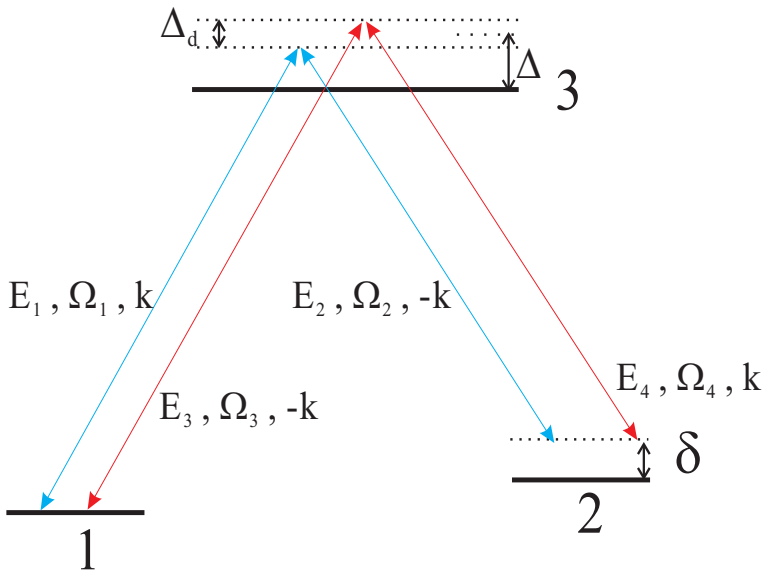

Figure 2.1: Raman configuration that can be used to produce an effective two-photon standing wave field on the $1-2$ transition.

of fields E_1 and E_2, respectively. Thus, the pair of fields E_3 and E_4 is equivalent to a Raman field with propagation vector $-2\mathbf{k}$. The two counter-propagating Raman fields interfere in driving transitions between the states 1 and 2. To lowest order in the Raman field strength, this leads to a modulation of ground state population difference and coherence that varies as $\cos(4kz)$. In this manner, a density grating with a period of $\lambda/4$ can be created.

It should be pointed out that in order to achieve the results mentioned in the previous paragraph, we have to neglect any effects related to E_1 (E_3) driving the 1-3 transition or field E_2 (E_4) driving the 2-3 transition. It is also assumed that fields E_1 and E_3 (or E_2 and E_4) do not interfere in driving single-photon transitions, nor do fields E_1 and E_4 (or E_2 and E_3) drive two-photon Raman transitions between states 1 and 2. The first requirement can be met owing to polarization selection rules, while the second is ensured by a frequency difference Δ_d introduced between E_1 and E_3 (or E_2 and E_4).

2.2 Sub-Doppler Laser Cooling of the Raman Optical Lattice

In the previous section, we have shown that a reduced-period optical lattice is possible in an effective Raman field scheme. The experimental realization of such an optical lattice, however, might be difficult unless some sub-Doppler laser cooling effect is present in this lattice configuration. In this section, we present theoretical evidence for the existence of sub-Doppler laser cooling in the case of the two-photon resonance of the Raman fields, $\delta = \Omega_1 - \Omega_2 - \omega_{21} = 0$, where Ω_i represents the laser frequency of the ith lattice beam. The friction force and diffusion coefficients are calculated using a semiclassical approach and are shown to be very similar to those obtained in standard Sisyphus cooling. A dressed atom picture is introduced to help facilitate the comparison of the ROL cooling with conventional Sisyphus cooling. The calculation is repeated using a quantum Monte-Carlo Wave-function simulation.

2.2.1 Semi-classical Calculations

To simplify the calculations, we consider a somewhat unrealistic level scheme in which states 1 and 2 in Fig. 2.1 have angular momentum $J = 0$, while state 3 has angular momentum $J = 1$. The basic physics remains unchanged for different angular momentum states. We then make further assumptions. First, the Rabi frequencies χ (assumed real) associated with all the atom-field transitions are assumed to be equal. In addition, we assume the same decay rate of state 3 to each of states 1 and 2, Γ_{31}=Γ_{32}=$\Gamma/2$. Finally, All fields are taken to be linearly polarized in the same direction; there is no polarization gradient. The results would remain unchanged if all the fields were σ_+ (or σ_-) polarized.

Under the rotating-wave approximation and neglecting spontaneous emission, the

Hamiltonian for the atom-field system is

$$\begin{aligned} H = &\textstyle\sum_{j=1}^{3} \hbar\omega_j \left|j\right\rangle \left\langle j\right| + \hbar\chi \left[\left|1\right\rangle \left\langle 3\right| \left(e^{-i(kz-\Omega_1 t)} + e^{-i(-kz-\Omega_3 t)}\right)\right. \\ &\left. + \left|2\right\rangle \left\langle 3\right| \left(e^{-i(-kz-\Omega_2 t)} + e^{-i(kz-\Omega_4 t)}\right) + \text{adj}\right] , \end{aligned} \tag{2.1}$$

where $\hbar\omega_j$ is the energy of state j and "adj" stands for adjoint. If the atom-field detunings are sufficiently large to satisfy

$$\Omega_1 - \omega_{31} \approx \Omega_3 - \omega_{31} \approx \Omega_2 - \omega_{32} \approx \Omega_4 - \omega_{32} \equiv \Delta \gg \Gamma, \chi, kv \tag{2.2}$$

it is possible to adiabatically eliminate the population in state 3 and obtain an effective two-state Hamiltonian

$$H_{eff} = \sum_{j=1}^{2} \hbar\omega_j \left|j\right\rangle \left\langle j\right| + 2\hbar\cos(2kz) \left(\chi^2/\Delta\right) \left[e^{i(\delta+\omega_{21})t} \left|1\right\rangle \left\langle 2\right| + e^{-i(\delta+\omega_{21})t} \left|2\right\rangle \left\langle 1\right|\right] , \tag{2.3}$$

where

$$\delta = \Omega_1 - \Omega_2 - \omega_{21} = \Omega_3 - \Omega_4 - \omega_{21}, \tag{2.4}$$

is the two-photon Raman detuning. The above analysis neglects a common Stark shift of ground states. As justified in the previous section, interference between fields E_1 and E_3 (or E_2 and E_4) in driving single-photon transitions is not considered here, nor is the combined action of fields E_1 and E_4 (or E_2 and E_3) in driving Raman transitions between states 1 and 2.

This effective Hamiltonian is used to obtain the equations of motion for density matrix elements ρ_{ij} in a field interaction representation. For classical center-of-mass motion ($d\rho_{ij}/dt = \partial\rho_{ij}/\partial t + v\partial\rho_{ij}/\partial y$), one finds the steady-state equations of motion for density matrix elements to be

$$\alpha\frac{\partial w}{\partial x} = -w(x) + 2i\sigma\left(\rho_{21} - \rho_{12}\right)\cos x\,, \tag{2.5a}$$

$$\alpha\frac{\partial \rho_{12}}{\partial x} = -\left(1 + i\frac{d}{2}\right)\rho_{12} - i\sigma w\cos x - \frac{1}{2}\cos x\,, \tag{2.5b}$$

where $w = \rho_{22} - \rho_{11}$ is the population difference of levels 2 and 1,

$$x = 2kz, \tag{2.6a}$$

$$d = \frac{\delta}{\Gamma'} \tag{2.6b}$$

$$\alpha = kv/\Gamma', \tag{2.6c}$$

$$\sigma = \Delta/\Gamma, \tag{2.6d}$$

$$\Gamma' = \chi^2\Gamma/\Delta^2 \tag{2.6e}$$

Here Γ' is an optical pumping rate, and v is the z-component of the atomic velocity.

Before we solve Eqs.(2.5), several comments should be addressed about the equations. First, for $\delta \neq 0$, Eqs. (2.5) must be solved numerically; however, an analytical solution is possible if $\delta = 0$. Note that Eq.(2.5b) contains a source term, $-\frac{1}{2}\cos x$, that can be traced to the fact that $-\frac{1}{2}\cos x * (\rho_{11} + \rho_{22}) = -\frac{1}{2}\cos x$ since the total population, $(\rho_{11} + \rho_{22})$, of the atoms is conserved. Steady state is reached on a time scale $\Gamma'^{-1} \gg \Gamma^{-1}$. The parameter σ is actually independent of field strength in these dimensionless units. Finally, for zero velocity atoms, $\alpha = 0$, and for zero detuning $d = 0$, the population difference w vanishes (since the lattice configuration becomes symmetric regarding level 1 and 2) while the coherence $\rho_{12} = -\frac{1}{2}\cos x$ is spatially modulated. This is in contrast to traditional Sisyphus cooling, where the coherence vanishes while the population difference is spatially modulated.

2.2.1.1 Fokker-Planck Equation

In the Appendix of our published paper [14], Eqs. (2.5) are modified to include diffusion resulting from changes in atomic momentum associated with stimulated emission and absorption, as well as spontaneous emission. The total population $S = \rho_{11} + \rho_{22}$ now becomes a function of momentum and position, although the

dependence of S on position is neglected [19]. The modified equations are

$$\alpha\frac{\partial}{\partial x}\begin{pmatrix} u \\ v \\ w \end{pmatrix} = \begin{pmatrix} -1 & d/2 & 0 \\ -d/2 & -1 & -2\sigma\cos x \\ 0 & 2\sigma\cos x & -1 \end{pmatrix}\begin{pmatrix} u \\ v \\ w \end{pmatrix} - \begin{pmatrix} \cos x\, S + 2\sigma\hbar k \sin x \frac{\partial S}{\partial p} \\ 0 \\ 0 \end{pmatrix}, \tag{2.7}$$

$$\frac{\partial S}{\partial t} = \frac{7}{5}\hbar^2 k^2 \Gamma'\frac{\partial^2 S}{\partial p^2} - \frac{4\chi^2}{\Delta}\hbar k \sin x \frac{\partial u}{\partial p} - \frac{3}{5}\hbar^2 k^2 \Gamma' \cos x \frac{\partial^2 u}{\partial p^2}, \tag{2.8}$$

where $u = \rho_{12} + \rho_{21}$ and $v = i\,(\rho_{21} + \rho_{12})$. Each of the parameters u, v, w are now functions of the momentum $p = mv$ as well as position x. Equations (2.7) are solved for u, v, w and the solution for u is inserted into Eq. (2.8) for S. The resultant equation is averaged over a wavelength

$$\frac{\partial S}{\partial t} = \frac{7}{5}\hbar^2 k^2 \Gamma'\frac{\partial^2 S}{\partial p^2} - \frac{4\chi^2}{\Delta}\hbar k\overline{\sin x \frac{\partial u}{\partial p}} - \frac{3}{5}\hbar^2 k^2 \Gamma'\overline{\cos x \frac{\partial^2 u}{\partial p^2}}, \tag{2.9}$$

where the bar indicates a spatial average ($\bar{S} = S$, by assumption). In this work, only the limit of zero Raman detuning, $\delta = 0$, is considered.

If $d = 0$ (because $\delta = 0$), the equation for u is decoupled from the others and can be solved analytically.

$$\begin{aligned} u &= -\tfrac{1}{\alpha}\textstyle\int_{-\infty}^{x} dx' e^{-(x-x')/\alpha}\left(\cos x'\, S + 2\sigma\hbar k \sin x' \frac{\partial S}{\partial p}\right) \\ &= -\tfrac{1}{1+\alpha^2}\left\{S(\cos x + \alpha \sin x) + 2\sigma\hbar k \tfrac{\partial S}{\partial p}(\sin x - \alpha \cos x)\right\}. \end{aligned} \tag{2.10}$$

When this solution is substituted into Eq. (2.8) and the resulting equation is compared with the Fokker-Planck equation

$$\frac{\partial S}{\partial t} = \frac{\partial}{\partial p}\left[-\bar{F}\, S + \bar{D}_{ind}\frac{\partial S}{\partial p} + \frac{\partial}{\partial p}\left[\bar{D}_{sp} S\right]\right], \tag{2.11}$$

one can identify the spatially averaged friction force

$$\bar{F} = -\frac{2\chi^2}{\Delta}\hbar k \frac{\alpha}{1+\alpha^2}, \tag{2.12}$$

and the spatially averaged diffusion coefficients

$$\bar{D}_{sp} = \hbar^2 k^2 \Gamma' \left(\frac{7}{5} + \frac{3}{10} \frac{1}{1+\alpha^2} \right) , \tag{2.13}$$

$$\bar{D}_{ind} = \hbar^2 k^2 \frac{4\chi^2}{\Delta} \frac{\sigma}{1+\alpha^2} = \hbar^2 k^2 \frac{4\chi^2}{\Gamma} \frac{1}{1+\alpha^2} , \tag{2.14}$$

$$\bar{D}_{tot} = \hbar^2 k^2 \Gamma' \left\{ \frac{7}{5} + \frac{3}{10} \frac{1}{1+\alpha^2} + \frac{4\chi^2}{\Delta\Gamma'} \frac{\sigma}{1+\alpha^2} \right\} , \tag{2.15}$$

where $\alpha = kp/m\Gamma'$ and m is the atomic mass. These results are very similar to those found in conventional Sisyphus cooling [19].

2.2.1.2 Momentum Distribution

The Fokker-Planck equation, Eq. (2.11), can be solved analytically in steady state with the boundary condition $\partial S/\partial p|_{p=0} = 0$. The solution is given by

$$S(\bar{p}) = S(0) \exp \left[\int_0^p dp' \frac{\left(\bar{F} - \frac{\partial \bar{D}_{sp}}{\partial p'} \right)}{\bar{D}_{ind} + \bar{D}_{sp}} \right] . \tag{2.16}$$

Since $\alpha = kv/\Gamma' = kp/m\Gamma'$,

$$\frac{\partial \bar{D}_{sp}}{\partial p} = -\frac{6}{5} \hbar k \omega_r \frac{\alpha}{(1+\alpha^2)^2} , \tag{2.17}$$

where

$$\omega_r = \frac{\hbar k^2}{2m} , \tag{2.18}$$

is the recoil frequency associated with a one-photon transition. Defining $\alpha' = kp'/m\Gamma'$, the integral in Eq. (2.16) can be rewritten in the form

$$\int_0^p dp' \frac{\left(\bar{F} - \frac{\partial \bar{D}_{sp}}{\partial p'} \right)}{\bar{D}_{ind} + \bar{D}_{sp}} = \int_0^\alpha d\alpha' \frac{\alpha'}{1+\alpha'^2} \cdot \frac{\frac{3}{5} - I'(1+\alpha'^2)}{4\sigma^2 + \frac{7}{5}(1+\alpha'^2) + \frac{3}{10}} , \tag{2.19}$$

where

$$I' = I \frac{4\sigma^2}{1+4\sigma^2}, I = \frac{\chi^2}{\Delta\omega_r}.$$

Combining Eqs. (2.16) and (2.19), the steady state solution of the Fokker-Planck equation Eq. (2.11) is given by

$$S(\bar{p}) = S(0)\left(1+\frac{\bar{p}^2}{\bar{p}_c^2}\right)^{\beta_0} \frac{1}{\left(1+\frac{\bar{p}^2}{\bar{p}_c^2}\beta_1\right)^{\xi+\beta_0}}\,, \tag{2.20}$$

where

$$\bar{p} = p/\hbar k, \qquad \bar{p}_c = \frac{\Gamma'}{2\omega_r} = \frac{I}{2\sigma}\,, \tag{2.21a}$$

$$\beta_0 = \frac{1}{1+\frac{40}{3}\sigma^2} \approx 0\,, \tag{2.21b}$$

$$\beta_1 = \frac{14}{40\sigma^2+17} \approx \frac{7}{20\sigma^2}\,, \tag{2.21c}$$

$$\xi = \frac{5}{14} I \frac{4\sigma^2}{1+4\sigma^2} \approx \frac{5}{14} I\,. \tag{2.21d}$$

The normalized momentum distribution $\bar{S}(\bar{p})$, given by

$$\bar{S}(\bar{p}) = \frac{S(\bar{p})}{\int_{-\infty}^{+\infty} S(\bar{p}')d\bar{p}'} \tag{2.22}$$

is plotted in 3-D as a function of $\bar{p}$ and scaled intensity I for $\sigma = 10$ in Fig. 2.2. As seen in the figure, the narrowest momentum distribution occurs when $I \sim 5$.

From the steady state momentum distribution $S(\bar{p})$, the mean equilibrium kinetic energy can be calculated as

$$E_{eq} = E_r \frac{\int_{-\infty}^{\infty} \bar{p}^2 S(\bar{p})d\bar{p}}{\int_{-\infty}^{\infty} S(\bar{p})d\bar{p}}, \tag{2.23}$$

where $E_r = \hbar\omega_r$ is the recoil energy. The integrals can be evaluated analytically for $I > 21/5$, and together with the approximation made in Eqs. (2.21), the mean equilibrium kinetic energy is given by a simple expression as

$$\frac{E_{eq}}{E_r} = \frac{I^2}{I-\frac{21}{5}}\,. \tag{2.24}$$

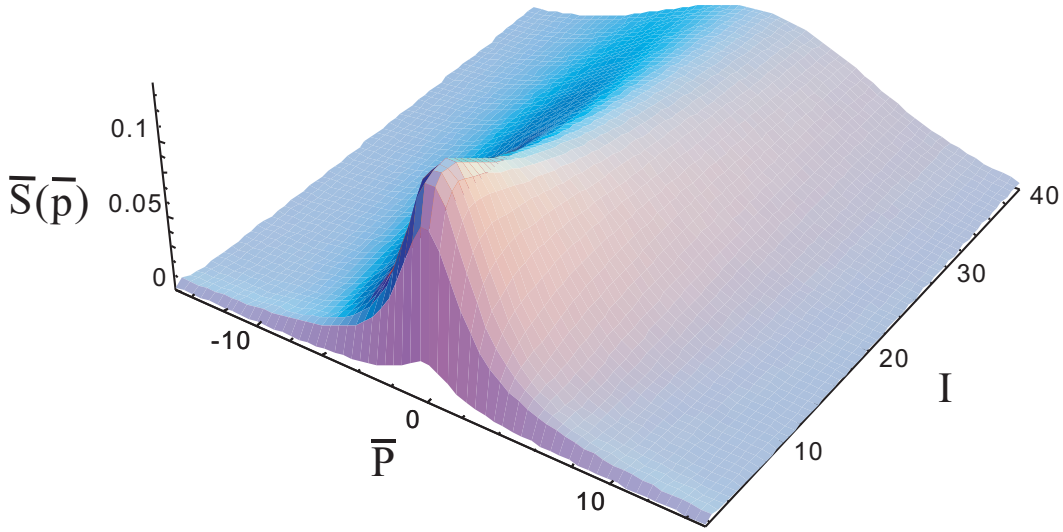

Figure 2.2: Normalized momentum distribution, $\bar{S}(\bar{p})$, as a function of $\bar{p}$ and I for $\sigma = 0$.

This equation indicates the lowest mean kinetic energy is achieved when $I = 8.4$, which is different from where the narrowest momentum distribution occurs as seen in Fig. 2.2. This discrepancy is attributed to insufficient cooling for the low intensity I. As a result, a significant number of atoms still occupy high momentum states, making the mean kinetic energy large despite a narrow momentum distribution around $\bar{p} = 0$. Detailed discussion is presented in the next section.

So far, analytical expressions for the steady-state momentum distribution $S(\bar{p})$ and the mean equilibrium kinetic energy E_{eq} are obtained in a semi-classical approach. These analytical solutions will be compared with the numerical results based on a Quantum Monte Carlo Wave-function Simulation (QMCWF) in the next section.

2.2.2 Quantum Monte Carlo Wave-function Simulations

To gain further insight into the cooling dynamics, we solve the problem using quantum Monte Carlo wavefunction Simulations (QMCWF) [20, 21]. The simulations employ a full quantum-mechanical description of the center-of-mass motion of the atoms and allow us to determine their spatial and momentum distributions.

In the simulation, instead of evaluating the density matrix, we propagate the wave-function directly according to the Schrödinger equation

$$i\hbar\frac{\partial|\Psi\rangle}{\partial t} = H(t)|\Psi\rangle\,. \tag{2.25}$$

Note that the Hamiltonian here is the full Hamiltonian, including the kinetic energy part and the potential operator part: $H = H_{kin} + H_{pot}$, where $H_{kin} = \hat{p}^2/2M$ and H_{pot} describes the interaction between the atoms and light fields. In principle, the QMCWF simulation can deal with the exact H_{pot} that includes the excited state. However, to simplify the simulation procedure, the excited-state components of the wavefunctions are adiabatically eliminated as in the semiclassical approach. Taking the spontaneous decay into account, the matrix elements of the potential operator H_{pot} are of the form

$$\langle z', m'|H_{pot}|z, m\rangle = \frac{\hbar\chi^2}{\Delta + i\Gamma/2}A_{m',m}(z)\delta(z'-z) \tag{2.26}$$

where m', m refer to the two ground state, $m', m \in (1, 2)$. In a conventional interaction representation, the elements $A_{m',m}$ are given by

$$\begin{aligned}
A_{1,1}(z,t) &= 2[1+\cos(2kz - \Delta_d t + \phi_{13})] \\
A_{2,2}(z,t) &= 2[1+\cos(2kz + \Delta_d t + \phi_{42})] \\
A_{1,2}(z,t) &= 2e^{i\theta/2}e^{i\delta t}\cos(2kz-\phi t) + e^{i[(\delta+\Delta_d)t+\phi_{41}]} + e^{i[(\delta-\Delta_d)t+\phi_{23}]} \\
A_{2,1}(z,t) &= A^*_{1,2}(z,t)\,,
\end{aligned} \tag{2.27}$$

where $\Delta_d = \Omega_1 - \Omega_3 = \Omega_2 - \Omega_4$, ϕ_i is the phase of the individual field and $\phi_{ij} = \phi_i - \phi_j$, $\phi = \phi_{21} - \phi_{43}$, $\theta = \phi_{21} + \phi_{43}$. Assuming that $|\Delta_d| \gg \Gamma', |\delta|$, the last two terms in element $A_{1,2}(z,t)$ are fast-oscillating terms compared with the time scale of $1/\Gamma'$ and hence average to zero. The remaining term in $A_{1,2}(z,t)$ contains two phases $\theta/2$ and $\phi/2$. Since $\phi/2$ represents a global shift of the lattice, it can be ignored during the simulation. The phase θ is not important if no other source, such as spontaneous decay, contributes to the creation of coherence between ground states $|1\rangle$ and $|2\rangle$, which is not considered in our model and is not the case experimentally.

The wavefunction $|\Psi_m\rangle$ can be expressed in either spatial or momentum representations. In coordinate space,

$$|\Psi_m\rangle = \sum_{n=-n_{max}}^{n_{max}} \alpha_n |z_n, m\rangle, z_n = n\lambda/4n_{max}\,; \tag{2.28}$$

in momentum space,

$$|\Psi_m\rangle = \sum_{n=-n_{max}}^{n_{max}} \beta_n |p_n, m\rangle, p_n = \hbar(2nk_L + q)\,, \tag{2.29}$$

where $k_L = 2\pi/\lambda$, n is an integer and n_{max} =16 or 32. The continuous momentum variable q, which satisfies $-k_L \leqslant q \leqslant k_L$, is associated with the photon recoil of spontaneous emission. The coefficients α_n and β_n are connected by a discrete Fourier transformation

$$\alpha_n = \frac{1}{\sqrt{2\pi}} \sum_{n=-n_{max}}^{n_{max}} e^{iz_n 2nk_L} \beta_n\,; \tag{2.30}$$

$$\beta_n = \frac{1}{\sqrt{2\pi}} \sum_{n=-n_{max}}^{n_{max}} e^{-iz_n 2nk_L} \alpha_n\,. \tag{2.31}$$

In a small time interval Δt, the evolution of the wavefunction takes the form

$$|\Psi(t+\Delta t)\rangle = e^{-\frac{i}{\hbar}H\Delta t}|\Psi(t)\rangle\,. \tag{2.32}$$

As discussed at the beginning of this section, the Hamiltonian has two components: $H_{kin} = \hat{p}^2/2M$, which is diagonal in momentum space, and H_{pot}, which is diagonal in coordinate space. Thus, we use a split-operator method to propagate the wavefunction. First, in a small time step, Δt, the time evolution operator can be approximated as

$$e^{-\frac{i}{\hbar}H\Delta t} = e^{-\frac{i}{2\hbar}H_{kin}\Delta t}e^{-\frac{i}{\hbar}H_{pot}\Delta t}e^{-\frac{i}{2\hbar}H_{kin}\Delta t}. \tag{2.33}$$

Now the kinetic energy operator and the potential operator are separated. We can apply H_{kin} and H_{pot} to the wavefunction in the momentum and coordinate spaces, respectively. The transformation between these two bases is done using fast Fourier transformations (FFT).

We notice that the Hamiltonian is not Hermitian: there is an imaginary part involved according to Eq. 2.26, which causes a gradual decay of the wavefunction norm. At each time step, a random number is generated. The evolution of the wavefunction continues if the norm of the wavefunction is larger than this random number; otherwise, we assume a spontaneous emission occurred. The evolution is interrupted by a quantum jump. In each quantum jump, random numbers are drawn to select the type of transitions (into state $|1\rangle$ or state $|2\rangle$) and the direction of the spontaneously emitted photon, which only affects q. After the quantum jump, the wavefunction is modified in a well-defined way determined by the wavefunction prior to the jump and by the simulated quantum measurement of a spontaneously emitted photon of the selected type. This procedure, including the evolution of the wavefunction and the quantum jump, is carried out several thousand times until steady state is reached. The expectation values of the observables, such as momentum distribution, spatial distribution, mean kinetic energy, and so on, can be obtained from the final wavefunction.

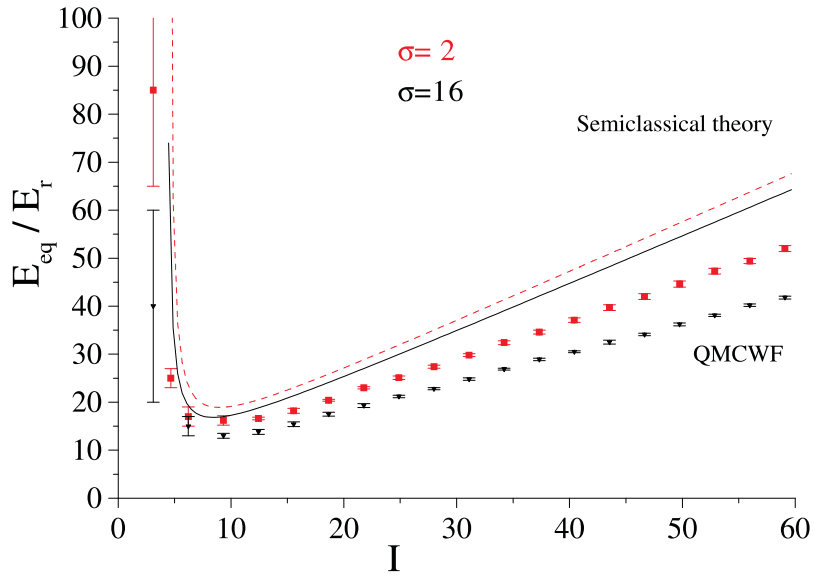

Figure 2.3: Steady-state kinetic energy as function of I for $\sigma = 2, 16$. Dots with error bars are from QMCWF and lines are from the semiclassical calculation, Eq. 2.23.

We first study the dependence of the steady-state kinetic energy E_{eq} as a function of the scaled intensity $I = \frac{\chi^2}{\Delta\omega_r}$. Results from both the simulation and the semiclassical calculation are plotted in Fig. 2.3 in unit of recoil energy, $E_r = \hbar\omega_r$, for $\sigma = \Delta/\Gamma = 2, 16$. As seen in the figure, both results display a linear dependence of E_{eq} on I for $I \gtrsim 10$. The energy values obtained in the QMCWF are about 30% lower than those obtained in the semiclassical calculations. This systematic difference is attributed to the beneficial effect of atomic localization in the lattice wells, which is accounted for in the QMCWF, but not included in the semiclassical calculations.

Fig. 2.4 shows the momentum distributions multiplied by $\bar{p}^2$ for $\sigma = 8$ and several different values of scaled intensity I. It is seen that when the intensity is small, $I = 3.11$, the cooling is not sufficient: there is still a significant population of atoms occupying high momentum states, $\bar{p} > 20$. When the intensity is large, $I = 50$, the two peaks become further apart, which corresponds to a broader momentum distribution. The systematic difference between the semiclassical results and the QMCWF simulation results can again explained by the localization effect of the

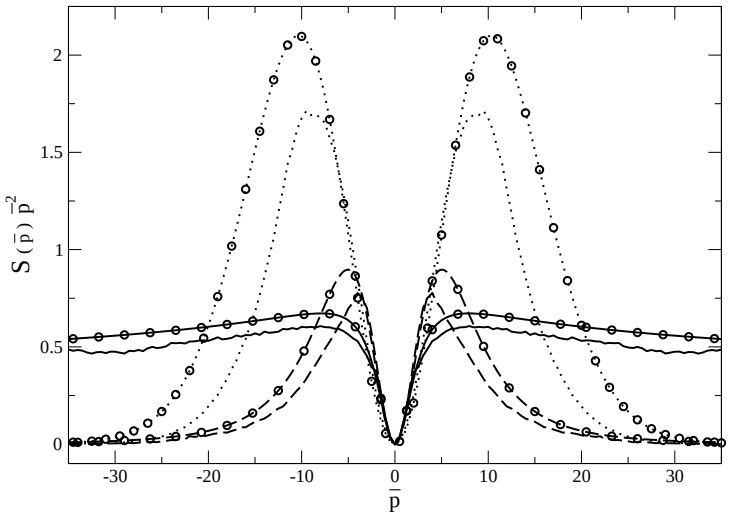

Figure 2.4: The momentum distribution, $S(\bar{p})$, multiplied by $\bar{p}^2$ for $\sigma = 8$ and several different values of I: I=3.11, solid line; I=8.4, dashed line; I=50, dotted line; lines, from semiclassical calculation, Eq. 2.20; lines with circles, from QMCWF.

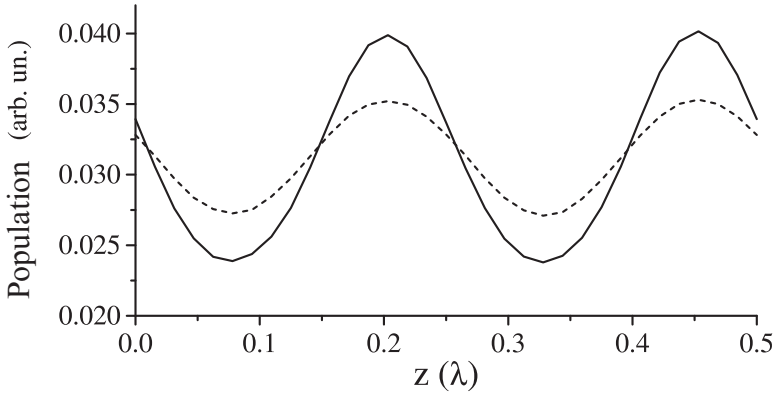

Figure 2.5: Population of atoms at different locations after the application of the ROL with $\sigma = 3$, and $I = 5$ (dashed) and 35 (solid).

atoms in the lattice wells.

The QMCWF simulation also yields the spatial density distribution of the atoms inside the lattice, which is found to have a period of $\lambda/4$, shown in Fig. 2.5, in agreement with the discussion in the previous section. Quantitatively, the simulations show that the modulation depth (defined as the difference between the maximum and minimum densities divided by their sum) increases with the beam intensity I and the atom-field detuning Δ, as shown in Fig. 2.6. A modulation depth of ~ 0.4 can be achieved.

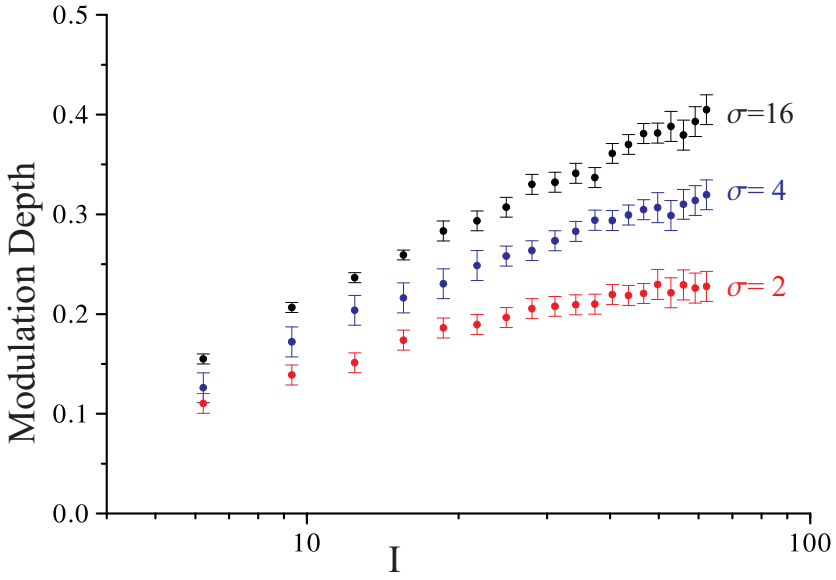

Figure 2.6: Modulation depth of the density distribution of the atoms in the lattice as a function of I for several values of σ.

2.3 Conclusion

In conclusion, we have proposed a new optical lattice scheme using Raman transitions, which leads to a reduced periodicity. Moreover, based on both semi-classical calculations and quantum Monte-Carlo wavefunction (QMCWF) simulations, a sub-Doppler laser cooling mechanism, different from other laser cooling mechanisms, is present in this Raman-optical-lattice (ROL) configuration. From the QMCWF simulations, the ROL produces an atomic density distribution with a period of $\lambda/4$, in agreement with the theoretical prediction.

CHAPTER III

Experimental Realization of the ROL

In the previous chapter, it was established theoretically that there is a sub-Doppler cooling mechanism in the reduced-period Raman Optical Lattice (ROL). Experimental evidence is presented in this chapter to verify both the sub-Doppler cooling and $\lambda/4$ periodicity of a ROL applied to ^{87}Rb atoms. A time-of-flight (TOF) method is employed to measure momentum distributions of the atoms. The sub-Doppler cooling of the ROL is then established by comparing the momentum distributions before and after the application of the ROL. From the momentum distribution, the equilibrium temperature of the atoms can be calculated. Our data shows that the atoms reach a temperature of about 8 μK after the ROL cooling. The dependence of the ROL cooling on different parameters is also characterized. To probe the spatial distribution of atoms in the ROL, a phase-controllable standing wave–an optical mask–is applied to atoms right after the ROL. The number of atoms optically transferred by the mask is measured as a function of relative position between the lattice and the mask. This corresponds to a direct mapping of the spatial distribution of atoms. We first conduct the mask experiment in a $\lambda/2$-period optical lattice and then repeat it in the ROL. By comparing the two experimental results, a clear signature of the $\lambda/4$ periodicity of the ROL is obtained.

3.1 Experimental Setup

3.1.1 Magneto-Optical Trap

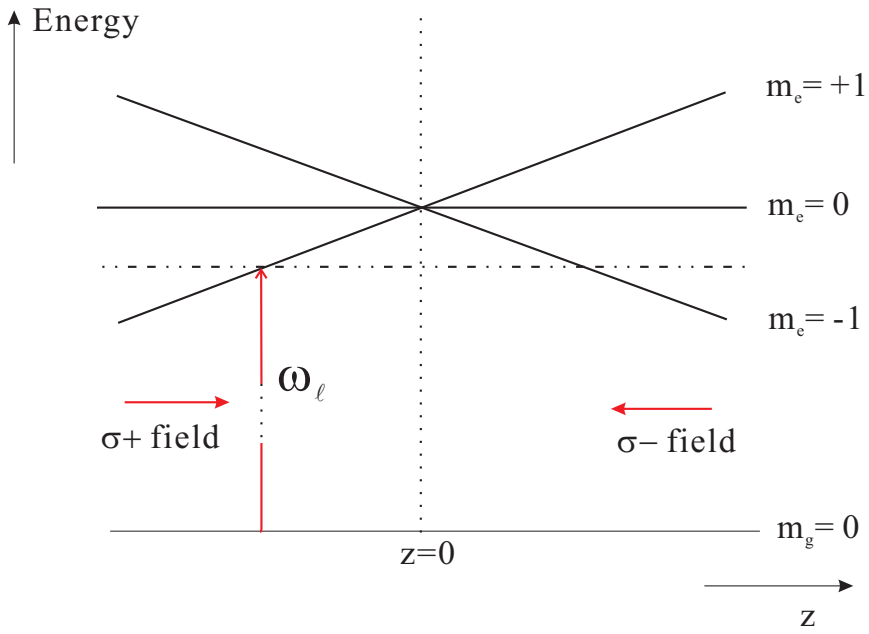

Figure 3.1: A simplified 1-D MOT energy diagram

A standard vapor-cell Magneto-optical trap (MOT) is used to collect an atom cloud, $\sim$ 1.5 mm in diameter, of up to 10^7 ^{87}Rb atoms for the lattice experiment. The basic concept of a MOT can be explained in a simple one dimensional model. For atoms moving in a linearly inhomogeneous magnetic field, B(z)=Az, the magnetic sublevels of the atoms are also linearly shifted. In the simplest case, we assume that the atoms only have two levels: ground state, $J_g = 0$, and excited state, $J_e = 1$. The corresponding energy diagram is shown in Fig. 3.1. Also shown are two counterpropagating laser beams of opposite circular polarization, both red-detuned with respect to unshifted $J_g = 0 \rightarrow J_e = 1$ transition. As seen in Fig. 3.1, when an atom moves left of the center (z=0 and B=0), the $\Delta m = 1$ transition is closer to resonance than the $\Delta m = -1$ transition. Hence, more photons from the $\sigma+$ beam are scattered by the atom than from the $\sigma-$ beam. Due to the radiation-pressure

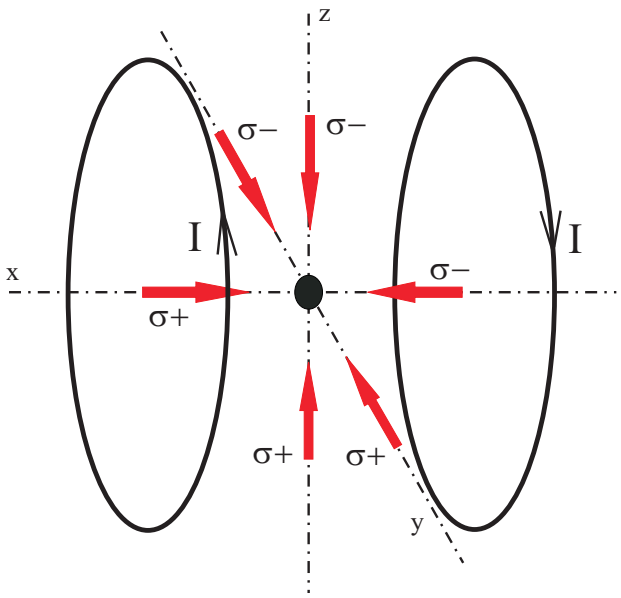

Figure 3.2: The 3-D MOT setup

imbalance, the atom is driven back towards the center. In the opposite case where the atom drifts right, a similar argument yields that it is pushed back by scattering more $\sigma-$ photons. The atom is thus trapped spatially in the vicinity of z=0. At the same time, in velocity space, the atoms experience an analogous situation due to the Doppler effect and concentrate around the zero-velocity region. As a result, trapping and cooling of the atoms are achieved simultaneously in a MOT.

This 1-D MOT scheme can be extended to 3-D, where the trapping magnetic field is provided by two coils in an anti-Helmholtz configuration, and three pairs of counterpropagating beams meet at the center of the trap (B=0) from three orthogonal directions as shown in Fig. 3.2. The beams are red-detuned with respect to the $5S_{1/2}$, $F = 2 \rightarrow 5P_{3/2}$ $F' = 3$ transition of ^{87}Rb atoms. Although the internal states involved in the MOT transition are much more complicated than those discussed in the simple 1-D model, the basic physics remains the same. Since the $5S_{1/2}$ ground state has another level, $F = 1$, a repumper beam, on resonance with the $5S_{1/2}$, $F = 1$ $\rightarrow 5P_{3/2}$ $F' = 2$ transition, is necessary during the MOT operation to pump atoms

back to the $F = 2$ level. The frequency of both the MOT and repumper beams are stabilized to within 1 MHz using the standard saturation spectroscopy method [22].

3.1.2 ROL Transition Diagram

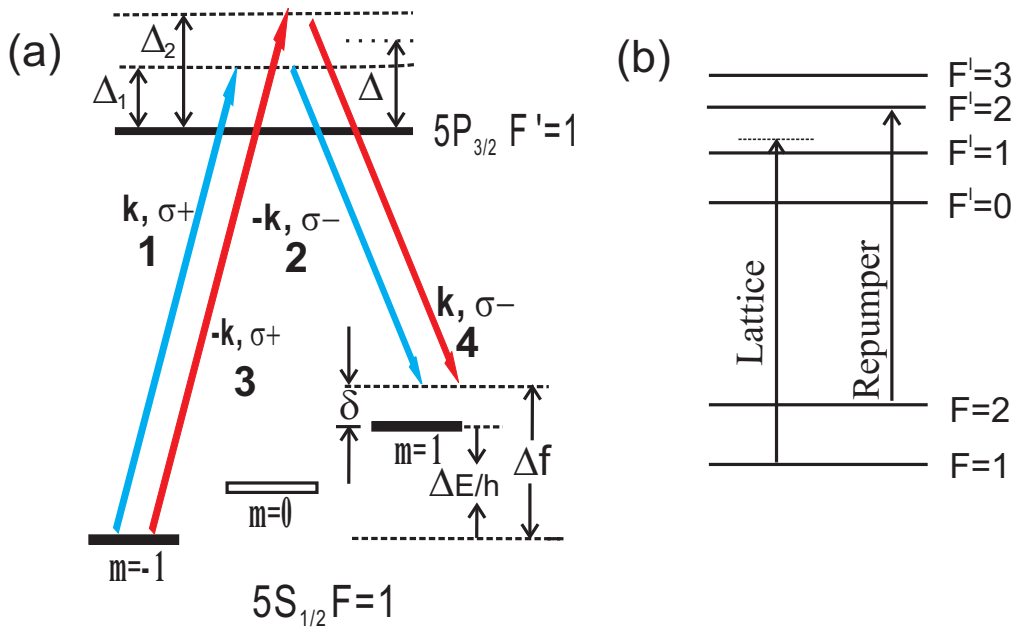

Figure 3.3: (a) Level scheme and field directions and polarizations. (b) Lattice and repumper transitions.

As shown in Fig. 3.3(a), The ROL is formed by two pairs of counter-propagating laser beams driving the $5S_{1/2}$ $F = 1 \rightarrow 5P_{3/2}$ $F' = 1$ transition of ^{87}Rb atoms. Due to their polarizations, fields 1 and 3 drive only $|m = -1\rangle \rightarrow |e\rangle$ transitions and fields 2 and 4 drive only $|m = 1\rangle \rightarrow |e\rangle$ transitions. As discussed in Chapter II, when the average atom-field detuning, Δ, is much larger than the excited state decay rate, Γ (Γ=6MHz is the excited state decay rate), the excited state population can be adiabatically eliminated. Thus, the system can be simplified to a two-level system driven by an effective Raman field with a wave vector $-2\mathbf{k}$. Adding the other pair, fields 3 and 4, introduces another effective Raman field with a wave vector $+2\mathbf{k}$. These two effective Raman fields interfere in driving the $|m = -1\rangle \rightarrow |m = 1\rangle$ transition, which leads to a $\lambda/4$-period optical potential. By introducing a frequency

difference $\Delta_d = \Delta_2 - \Delta_1$ of a few MHz between fields 1 and 3, and between fields 2 and 4, couplings between any other pairs of these four lattice beams are to be neglected, as assumed in the theoretical calculation.

In the experiment, we implement a Δ_d of 4 MHz. The average atom-field detuning, $\Delta = (\Delta_1 + \Delta_2)/2$, can be set between -15Γ and $+16\Gamma$ relative to the $5S_{1/2}$, $F = 1 \rightarrow 5P_{3/2}$ $F' = 1$ transition. In order to optically pump the atoms into the active $F = 1$ state, a repumper beam on-resonance with the $5S_{1/2}$ $F = 2 \rightarrow 5P_{3/2}$ $F' = 2$ transition, as indicated in Fig. 3.3(b), is applied during the ROL phase. In the presently investigated scheme, both Raman transitions possess the same Raman detuning, δ. The value of δ is determined by both the frequency difference between the Raman beams, labeled as Δf in Fig. 3.3 (a), and the energy separation between the $|m = -1\rangle$ and $|m = 1\rangle$ sub-levels, which is tuned by an external magnetic field parallel to the lattice-beam direction.

3.1.3 Lattice Beam Setup

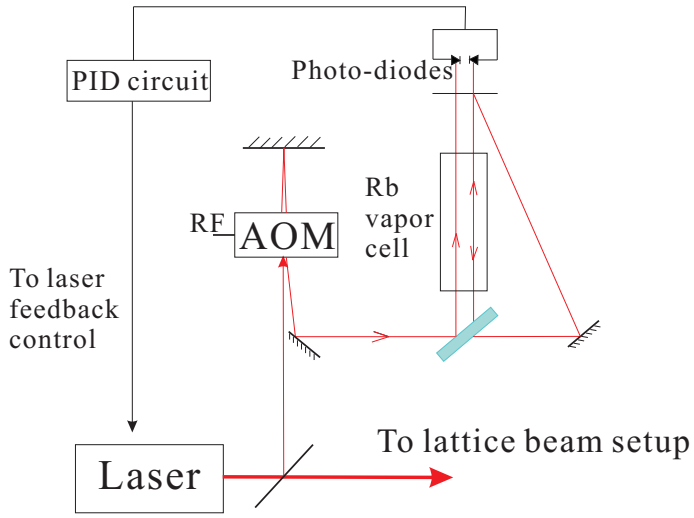

Figure 3.4: The saturation spectroscopy setup for the lattice beams. An AOM is added to the system to shift the frequency of the spectroscopy beam. In this setup we can change the frequency of the lattice beams by varying the RF frequency driving the AOM.

All four ROL beams are derived from a diode laser, the frequency of which is sta-

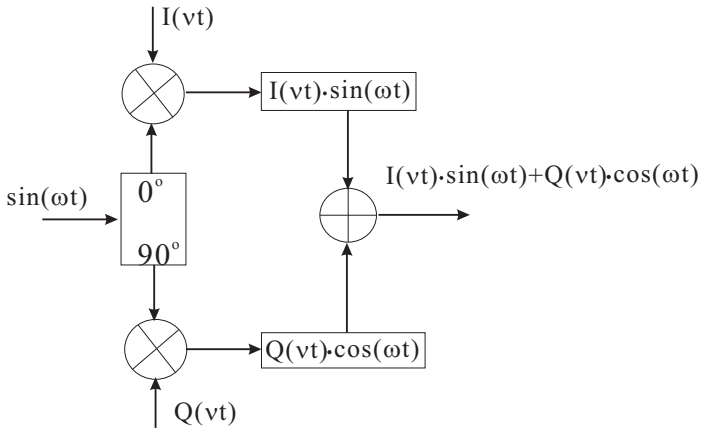

Figure 3.5: The function of the IQ modulator

bilized by the standard saturation spectroscopy method, with a slight modification. The spectroscopy beam, split from the lattice laser, is frequency shifted by passing through an acousto-optic modulator (AOM) twice before entering the standard spectroscopy setup as shown in Fig. 3.4. The frequency of the lattice beams can be varied by changing the frequency of the RF signal driving the AOM. This way, we can vary the lattice beam frequency in small steps over a broad range.

The output beam from the laser is split into four beams, which are frequency-shifted by individual amounts using four AOMs. The AOMs are driven by four RF signals generated by RF signal sources and a custom RF circuit. The main components of this RF circuit are IQ modulators. They can combine the local oscillator signal with the I and Q modulation signals as indicated in Fig. 3.5. Through careful selection of the phase difference between I and Q modulation signals, the IQ modulator can either increase or decrease the input frequency by an amount equal to the modulation frequency. Assuming the output signals of the RF generators are sine waves with no additional phase shift (adding a constant phase will not change the outcome.), according to the RF circuit shown in Fig. 3.6 the modulation signals for the IQ modulators are $\sin(\nu t)$ and $\cos(\nu t)$ for channel 1 and $\sin(\nu t)$ and $-\cos(\nu t)$

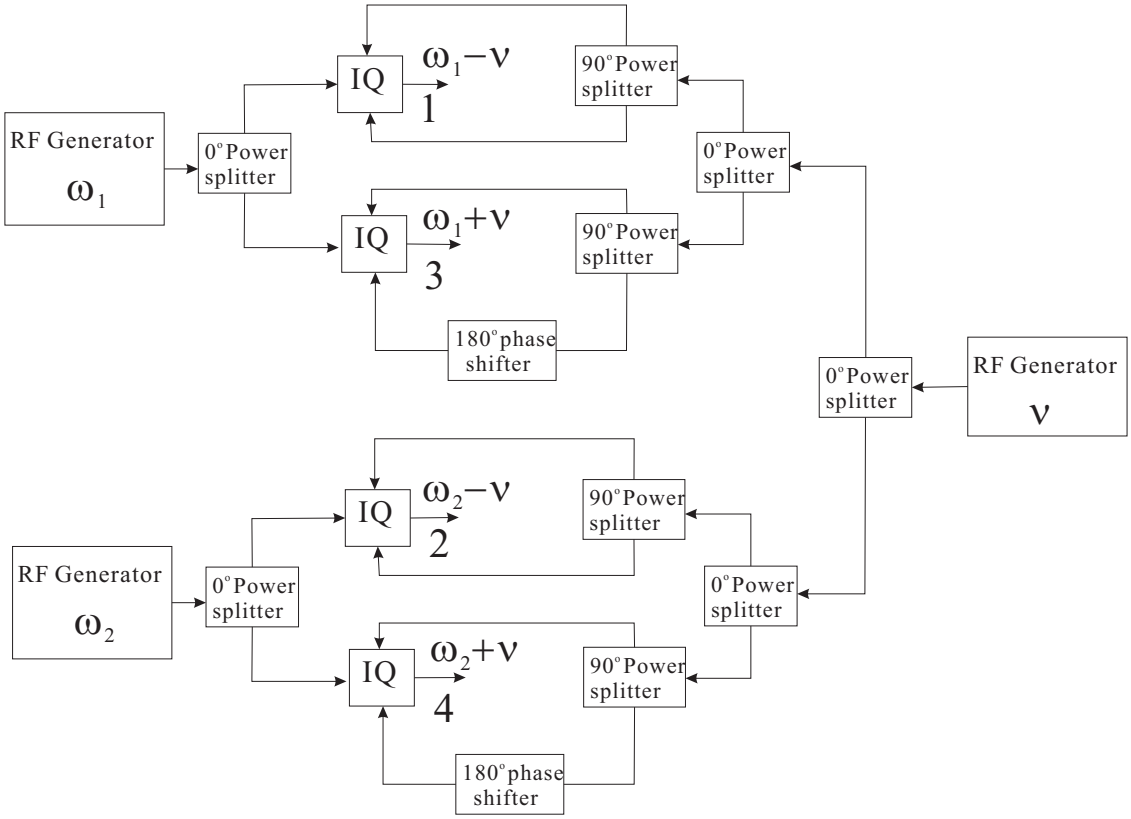

Figure 3.6: Schematic drawing of the RF circuit that is used to generate four RF signals with a stable frequency difference.

for channel 3 (the channel number corresponds to the lattice beam number in Fig. 3.3 (a)). The IQ modulator will combine these modulation signals with the input signal $\sin(\omega_1 t)$ according to Fig. 3.5. Thus, channel 1 and 3 output $\sin(\nu t)\cdot\sin(\omega_1 t)+\cos(\nu t)\cdot\cos(\omega_1 t) = \cos[(\omega_1-\nu)t]$ and $\sin(\nu t)\cdot\sin(\omega_1 t)-\cos(\nu t)\cdot\cos(\omega_1 t) = -\cos[(\omega_1+\nu)t]$, respectively. The frequency of the input signal is either increased or decreased by exactly the same amount. In this scheme, the frequency *differences* of the four ROL beams are very stable, as required for the ROL. The frequency fluctuations of the laser are much less than Γ and affect all ROL beams equally, and therefore do not significantly affect the ROL performance.

Spatial mode-matching of co-propagating pairs of beams (1 with 4 and 2 with 3) is achieved by coupling each beam pair into the two orthogonal modes of a shared

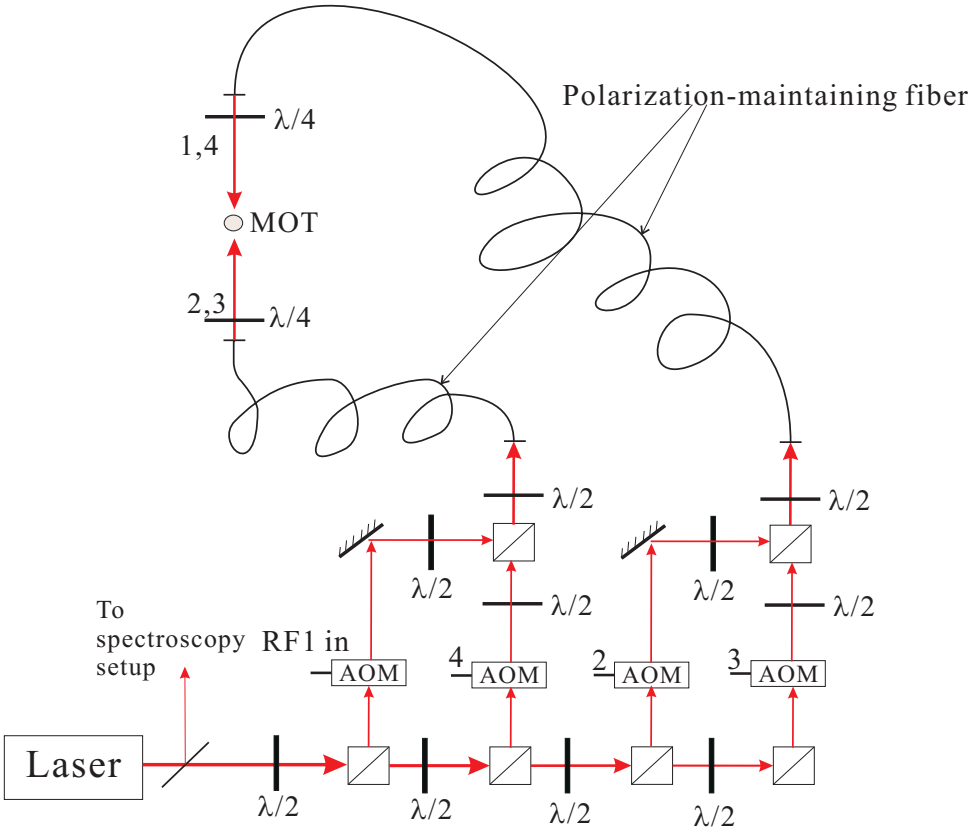

Figure 3.7: Schematic drawing of the lattice beam setup.

polarization-maintaining optical fiber using polarization optics, shown in Fig. 3.7. The combined beams coupled out of the fibers are passed through $\lambda/4$ -waveplates, leading to the polarizations indicated in Fig. 3.3 (a), and are directed vertically from opposite directions into the chamber. The spatial profiles of the beams at the location of the atomic cloud are approximately Gaussian with an intensity full-width-half-maxim (FWHM) of 8 mm.

3.2 Sub-Doppler Laser Cooling

3.2.1 Time-of-Flight Measurement

We probe the laser cooling effect using a time-of-flight (TOF) method [23, 24]. As shown in the top panel of Fig. 3.8, the TOF probing beam is a cylindrically collimated sheet of on-resonant ($5S_{1/2}$ $F = 2 \rightarrow 5P_{3/2}$ $F' = 3$ transition) light $\sim$

0.4 mm thick, located 20 cm below the MOT position. After application of the ROL, all fields are turned off. The atoms fall freely due to the gravity. As they fall through the TOF probe beam, their fluorescence is detected by a large-area photodiode. The photocurrent is then amplified using a transimpedance amplifier and finally recorded and averaged over typically 30 scans by a digital oscilloscope. The lower panel of Fig. 3.8 shows a typical TOF signal. The momentum distribution of the atoms follows from the time dependence of the signal.

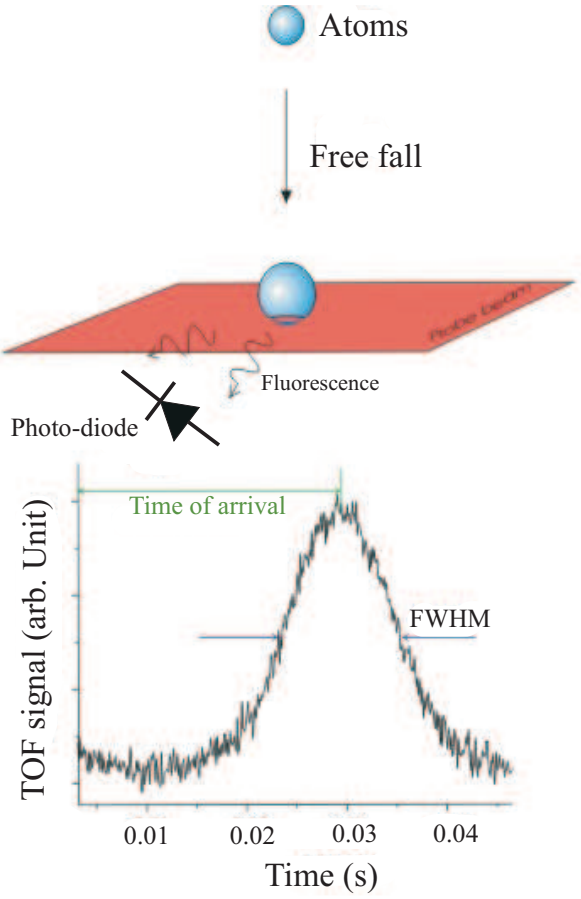

Figure 3.8: Schematic drawing of the time-of-flight method

3.2.2 Momentum Distribution of Atoms after the ROL Cooling

The experimental procedure for demonstrating ROL cooling is as following. The MOT is on for 600 ms to collect about 10^7 ^{87}Rb atoms. The atoms are then further

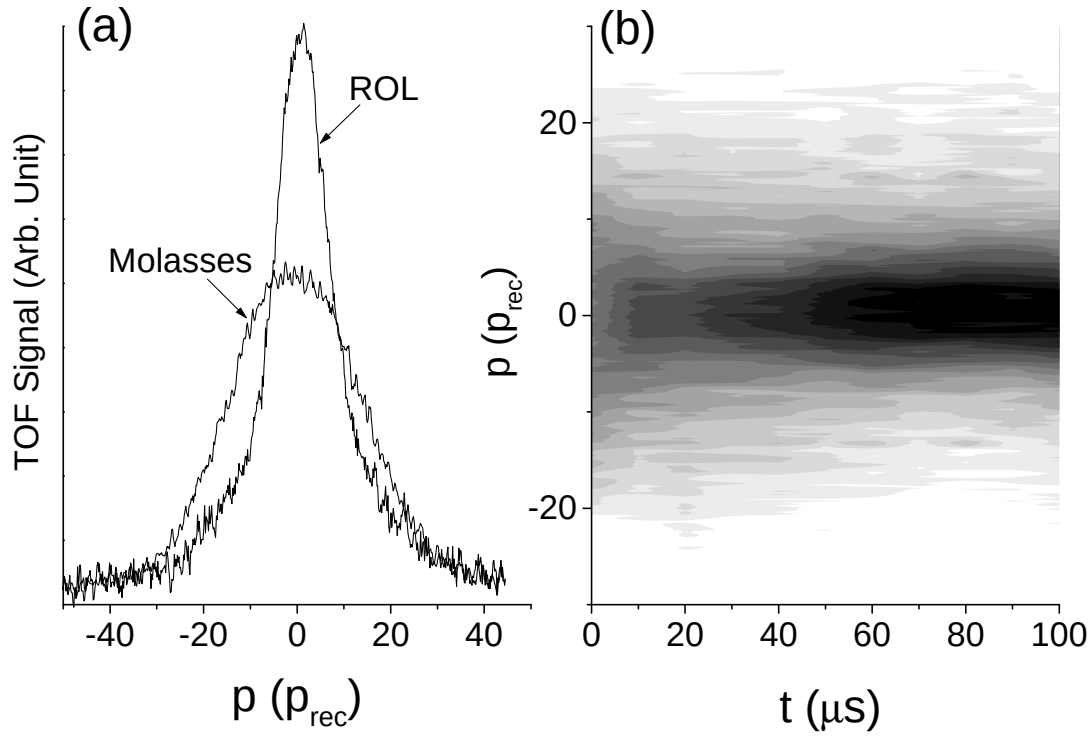

Figure 3.9: (a) Momentum distributions of atoms cooled by optical molasses and by ROL, respectively. (b) 2D plot of momentum distribution of atoms vs. cooling time in ROL.

cooled for 1 ms in an optical molasses to a temperature of $\sim$50 μK. After the molasses cooling, the ROL is applied for durations ranging from a few to 150 μs. Finally the momentum distribution of the atoms is measured using the TOF method. This procedure is repeated at 1 Hz rate. In Fig. 3.9 (a) we compare typical momentum distributions (in units of recoil momentum $p_{\rm rec} = \hbar k$) measured after cooling in a standard six-beam optical molasses and after additional cooling in the ROL (δ=0, $\Delta = 3\Gamma$, 1 mW/cm^2 single-beam intensity, 150 μs lattice duration). A Gaussian fit of the data yields a standard deviation σ_p that is related to the temperature by

$$T = \frac{\sigma_p^2}{M k_B}\,, \tag{3.1}$$

where M is the atomic mass and k_B is the Boltzmann constant. Note that we do not calculate the temperature from the mean kinetic energy (Eq. 2.23) because the unavoidable noise of experimental data, especially for large momenta, would result

in a large error based on the mean kinetic energy approach. Using the Gaussian-fit method, we find that the typical molasses temperature is 50 μK, while the ROL cools the atoms further to 8 μK. The presence of sub-Doppler cooling in the ROL is therefore established. To characterize the speed of the cooling process, we vary the duration of the ROL in steps of 10 μs. The resultant momentum distributions are assembled in a two-dimensional data set, which is displayed in Fig. 3.9 (b). The darkness represents the height of the TOF signal (or the population of the atoms). For the lattice parameters of Fig. 3.9 it is found that steady state is achieved in about 70 μs.

3.2.3 Intensity Dependence of the ROL Cooling

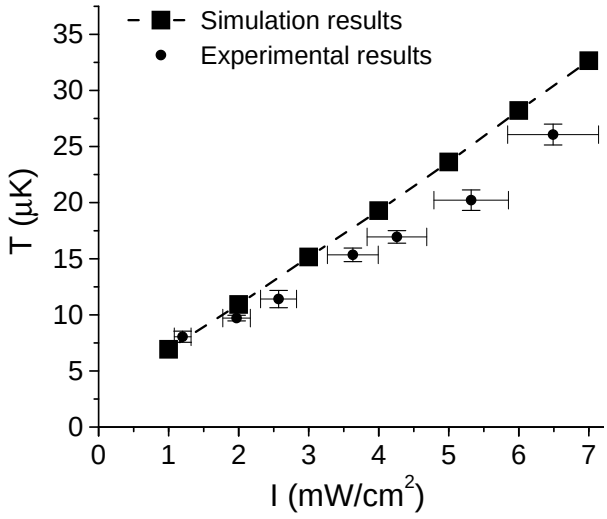

Figure 3.10: Intensity dependence of ROL cooling.

An important characteristic of laser-cooling is the dependence of the steady-state temperature on the intensity of the laser beams. We measure steady-state momentum distributions as a function of the single-beam intensity I at the center of the lattice beams and calculate the equilibrium temperature according to Eq. 3.1. The resultant data is shown by the circles in Fig. 3.10. We compare the experimental

results with the QMCWF simulations [14]. The simulations use the exact atomic and lattice-beam parameters used in the experiment, and hence can be compared directly with the experimental results. The squares in Fig. 3.10 show temperatures obtained from Gaussian fits to the simulated momentum distributions. Both in theory and experiment, we observe a linear relationship between intensity and temperature, and experimental and theoretical results agree to within 20%. The discrepancy may be caused by the Gaussian intensity profile of the laser beams, due to which the average intensity experienced by the atoms is slightly below the intensity I at the beam center. The QMCWF simulations also reproduce the time dependence of laser cooling in the ROL in a satisfactory manner.

3.2.4 Detuning Dependence of the ROL Cooling

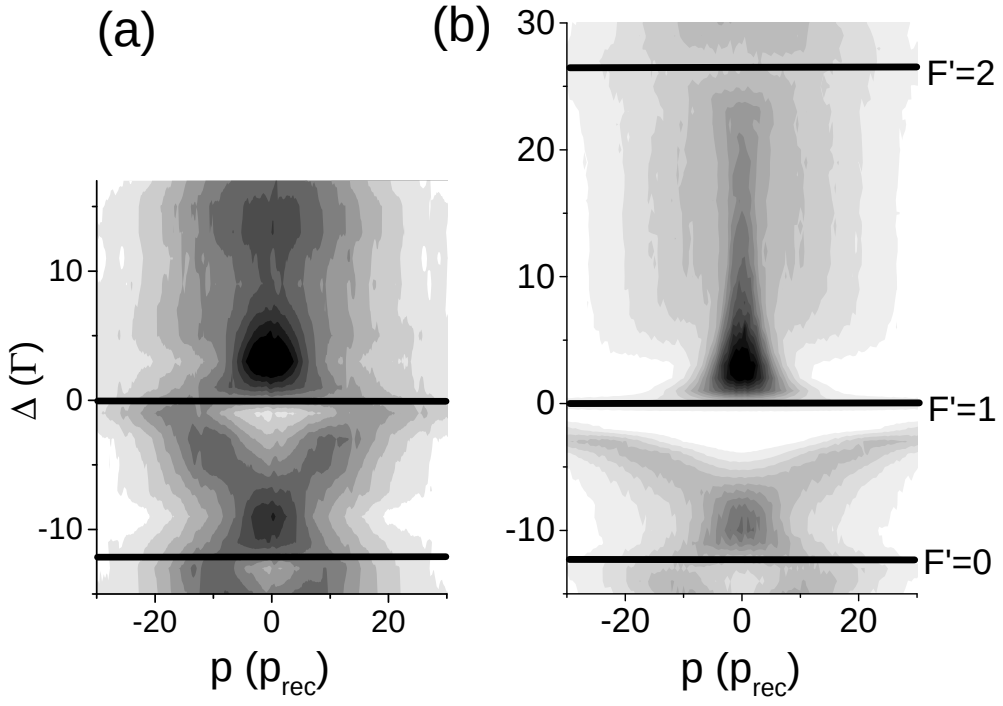

Figure 3.11: (a) 2D-plot of momentum distributions of atoms for different atom-field detunings Δ. (b) Simulation results.

As in standard optical lattices, where the detuning of the laser frequency greatly

affects the Sisyphus cooling [25], in the ROL the atom-field detuning Δ is also very important to the cooling. In Fig. 3.11(a) we show experimental momentum distributions as a function of Δ relative to the $F = 1 \rightarrow F' = 1$ transition, varied in steps of 2 Γ. This is accomplished by changing the frequency of the RF signal driving the AOM in the saturation spectroscopy setup (Fig. 3.4). Figure 3.11(b) offers the corresponding results from the QMCWF simulations. The latter extend beyond the $F' = 2$ level (this was not possible experimentally for technical reasons). Experimental and theoretical results generally agree well. Cooling occurs when the laser fields are slightly blue-detuned relative to the $F = 1 \rightarrow F' = 0$ and $F = 1 \rightarrow F' = 1$ transitions, and clearly works best for the $F = 1 \rightarrow F' = 1$ transition. No cooling is observed for either blue or red detuning from the $F = 1 \rightarrow F' = 2$ transition.

The detuning-dependence observed in the vicinity of the $F = 1 \rightarrow F' = 0$ and $F = 1 \rightarrow F' = 1$ transitions can be qualitatively explained using the result of the semi-classical treatment of the ROL in the previous chapter. There, the spatially averaged friction force on the atoms for $|\Delta| > \Gamma$ is found to be

$$\bar{F} \approx -\frac{2\chi^2}{\Delta}\hbar k \frac{\alpha}{1+\alpha^2}\,, \tag{3.2}$$

where $\alpha \approx \Delta^2 kv/\chi^2\Gamma$, χ is the Rabi frequency, and v is the velocity of the atoms. For positive Δ (blue-detuning), the friction force opposes the direction of motion, leading to sub-Doppler cooling. At small velocities, α is less than 1, and the friction force tends to be $\propto v\Delta$. Thus, lower temperatures should be achieved at larger detunings. In Fig. 3.11, this trend is generally observed for blue-detunings less than $\sim 5\Gamma$ relative to the $F = 1 \rightarrow F' = 0$ and $F = 1 \rightarrow F' = 1$ transitions. Since the velocity capture range v_c of the friction force, identified by $\left[d\bar{F}/dv\right](v_c) = 0$, decreases as $\propto \chi^2/\Delta^2$, the cooling becomes ineffective for larger blue-detunings. For negative Δ (red-detuning), the friction force and v have the same sign. Thus,

atoms will accelerate away from $v = 0$ ("sub-Doppler heating"). The acceleration eventually diminishes, as α increases with v. The net effect is that atoms should emerge with a (non-stationary) two-peak momentum distribution, as observed in Fig. 3.11 for red-detunings less than $\sim 5\Gamma$ relative to the $F = 1 \rightarrow F' = 0$ and $F = 1 \rightarrow F' = 1$ transitions. We have verified that the double-peaked momentum distributions are non-stationary; the separation between the two peaks gradually increases as a function of heating time in the ROL. Furthermore, for large v, α is much larger than 1. Under this condition, the heating force $\bar{F} \propto v\Delta^{-3}$. This explains why the separation between the two peaks is larger for smaller Δ. In a quantitative analysis, momentum diffusion must be considered in addition to friction [14].

To understand the qualitative differences in behavior in the vicinity of different upper-state hyperfine levels F', we need to take into account the magnetic sub-level $|m = 0\rangle$ that is not directly coupled by the fields (see Fig. 3.3). Near the $F = 1 \rightarrow F' = 0$ transition, atoms falling into that state require a long time to be optically pumped back into one of the active $|F = 1,\ m = \pm 1\rangle$ states through off-resonant excitation into $|F' = 1,\ m' = \pm 1\rangle$ and subsequent decay into $|F = 1,\ m = \pm 1\rangle$. The long dwell time of atoms in the inactive state reduces the ROL cooling and heating efficiency. In contrast, near the $F = 1 \rightarrow F' = 1$ transition the σ-polarized lattice beams rapidly re-pump atoms out of the $|m = 0\rangle$ state into one of the active levels. Thus, cooling and heating processes are expected to be more efficient near the $F = 1 \rightarrow F' = 1$ transition, as observed. Finally, the heating effect associated with near-resonant excitation from $|F = 1,\ m = \pm 1\rangle$ into $|F' = 2,\ m' = \pm 2\rangle$ entirely disables the ROL close to the $F = 1 \rightarrow F' = 2$ transition frequency, as evident in Fig. 3.11.

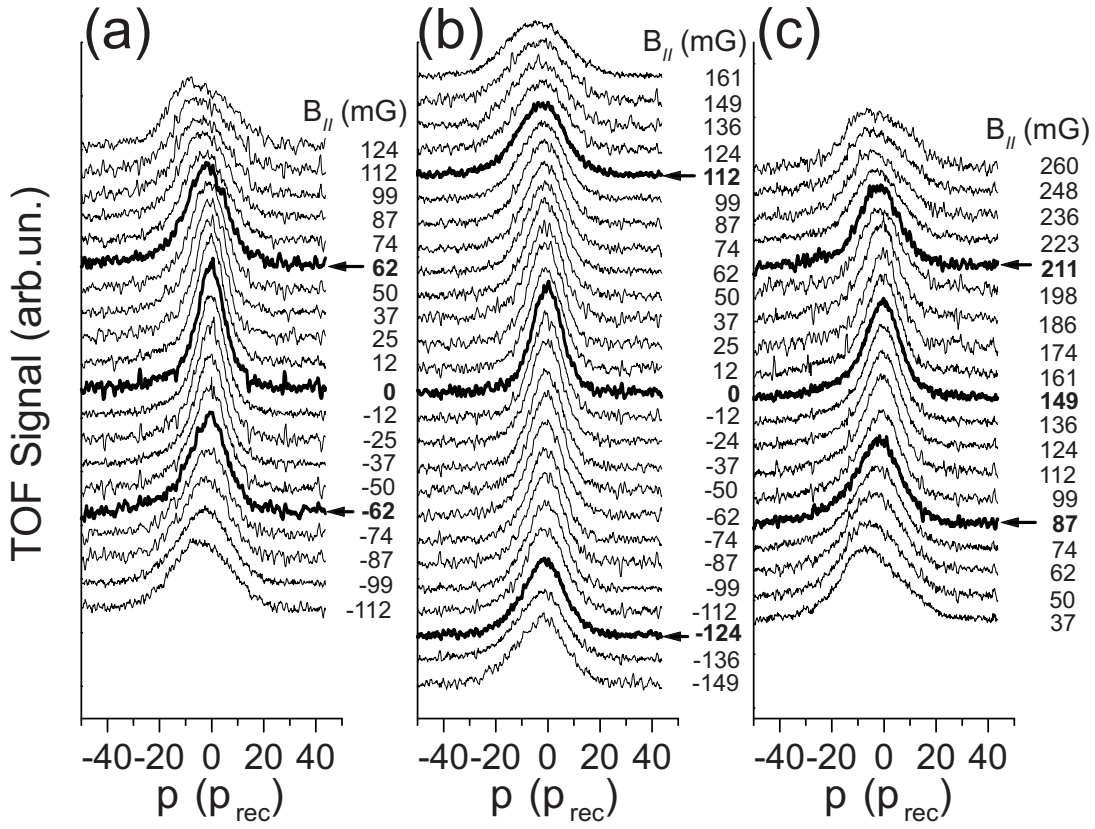

Figure 3.12: (a) Momentum distributions of atoms in the ROL for the indicated longitudinal magnetic fields and $\Delta f = f_1 - f_3 = 0$. Single-beam intensity is 1 mW/cm^2. (b) Same as (a) except the single-beam intensity is 2 mW/cm^2. (c) A frequency difference $\Delta f = -200$ kHz is applied. Single beam intensity is 1 mW/cm^2. The arrows indicate the boundaries of the cooling ranges defined in the text (1 mG corresponds to a change of 1.4 kHz in the detuning δ).

3.2.5 Raman Detuning Dependence of the ROL Cooling

We also study how the ROL cooling depends on δ. In our experiment, $\delta = \Delta f - \Delta E/h$, where $\Delta f = f_1 - f_3 = f_4 - f_2$ is the frequency difference between the beams driving the Raman transitions, and $\Delta E = -\mu_B B$ is the Zeeman splitting between $|m = 1\rangle$ and $|m = -1\rangle$ due to a longitudinal magnetic field B (see Fig. 3.3). Thus, δ can be varied by both Δf and B. We keep the frequency difference Δf fixed and take the TOF signals as a function of B, which is varied in steps of 12.4 mG, equivalent to steps of 17.4 kHz in δ. Figure 3.12(a) and (b) show the measured momentum distributions for $\Delta f = 0$ for single-beam intensities of 1 mW/cm^2 and

2 mW/cm^2, respectively. In both cases, we observe cooling over a certain range of B, and the cooling is symmetric about $B = 0$. Defining the cooling range $-\delta_c < \delta < \delta_c$ as the range of δ over which the temperature is less than twice the temperature at $\delta = 0$, we obtain $\delta_c = 85$ kHz and $\delta_c = 160$ kHz for Figs. 3.12(a) and (b), respectively. This result suggests that the cooling range is proportional to intensity. In Fig. 3.12(c) we apply a frequency difference $\Delta f = -200$ kHz. The cooling range is found to remain almost the same as for $\Delta f = 0$, whereby best cooling occurs at $B = 150$ mG. At this field value, $\delta \approx 0$, *i.e.* the Zeeman shift cancels the applied frequency difference Δf. Thus, laser cooling in the ROL performs best for zero two-photon detuning, $\delta = 0$. This is in contrast to conventional Sisyphus cooling, where a non-zero single-photon detuning is required to avoid excessive light scattering. This contrast in detuning behavior reflects the fact that the two cooling mechanisms are qualitatively different. Simulations are in good agreement with the observations in Fig. 3.12.

3.2.6 Transition of Laser Cooling between Standard and Raman Optical Lattices

As discussed in Chapter II, to establish the ROL configuration, a frequency difference Δ_d has to be introduced between lattice beams 1 and 3, and beams 2 and 4. This frequency difference ensures that we can neglect the coupling effect between field 1 and field 3 (2 and 4) in driving one-photon transitions, and between field 1 and field 4 (2 and 3) in driving Raman transitions. In this section we study the dependence of the ROL cooling on Δ_d.

The detuning difference Δ_d is varied in steps of 100 kHz by changing the modulation frequency. In Fig. 3.13, experimental momentum distributions are displayed in a two-dimensional representation as a function of Δ_d. We observe efficient sub-Doppler cooling for $\Delta_d \lesssim 100$ kHz. In the range 200 kHz $\lesssim \Delta_d \lesssim$ 500 kHz, no cooling

effect is observed; however, in that domain the momentum distributions appear to be modulated by a regular pattern (see dotted lines in Figs. 3.13 and 3.14). Over the range 500 kHz $\lesssim \Delta_d \lesssim$ 800 kHz, sub-Doppler cooling re-develops and reaches a steady level for $\Delta_d \gtrsim$800 kHz.

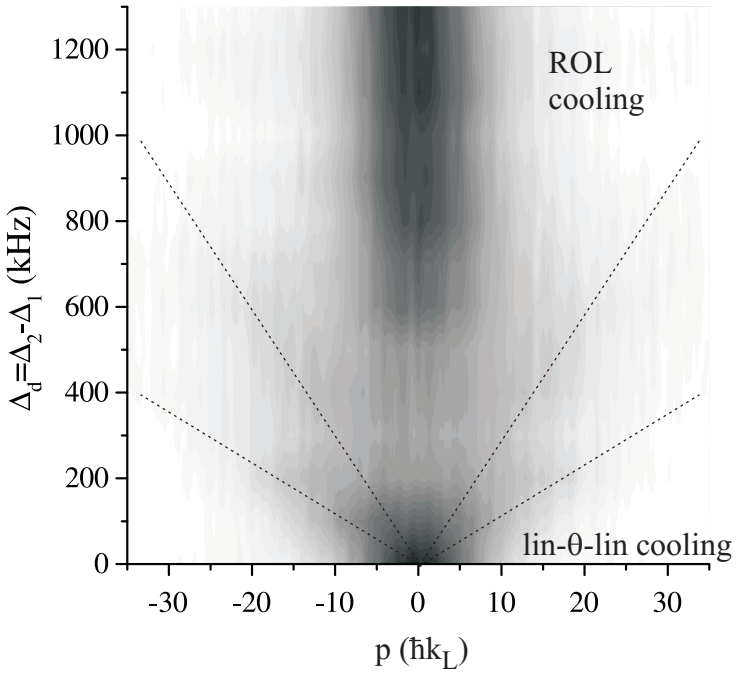

Figure 3.13: Momentum distributions of atoms, obtained from experimental time-of-flight data, as a function of Δ_d. The average lattice detuning Δ is 5 Γ, and the single-beam lattice intensity is 2 mW/cm^2. The atoms are cooled for 150 μs in the lattice. The figure shows two domains of efficient laser cooling, namely $\Delta_d \lesssim$ 100 kHz and $\Delta_d \gtrsim$ 600 kHz, as well as a regular pattern identified by the dotted lines.

The physics of the cooling can be qualitatively explained as follows. The co-propagating, spatially overlapping σ^+ and σ^- lattice beams 1 and 4 are equivalent to a single, linearly polarized net field, the polarization plane of which rotates at a frequency $\Delta_d/2$. Beams 2 and 3 are equivalent to an analogous net field. In a fixed, beam-independent frame, the polarization planes of the net fields rotate in opposite directions. If the rotation period $2/\Delta_d$ is of order of or exceeds the time it takes for an atom to laser-cool in a two-beam lin-θ-lin lattice, the cooling behavior is expected to be similar to that of the lin-θ-lin lattice [26, 27]. For the conditions in Fig. 3.9,

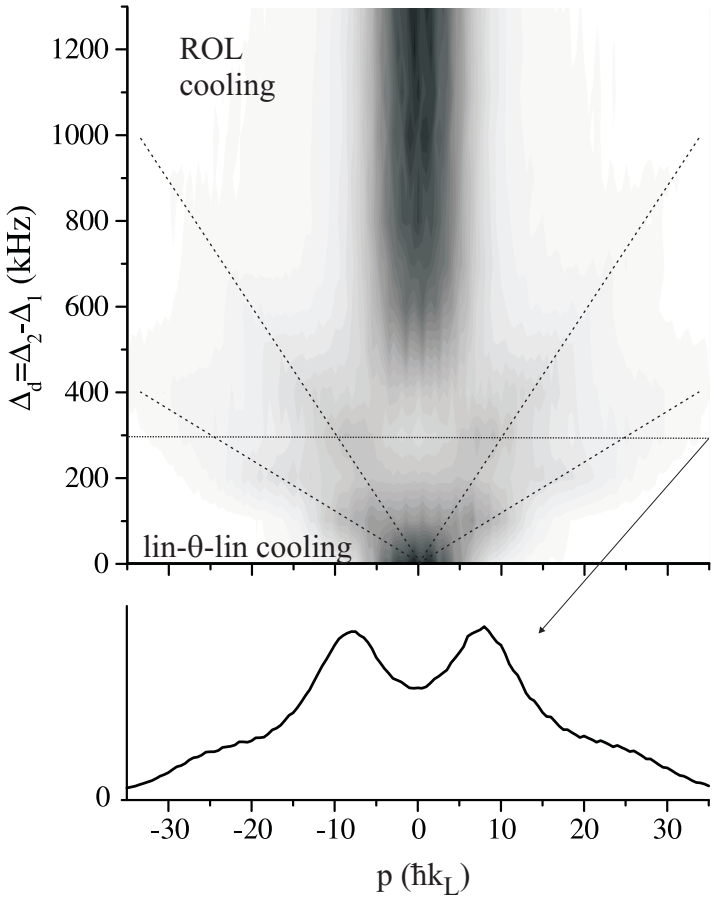

Figure 3.14: Top panel: Simulated momentum distribution of atoms as a function of $\Delta_{\rm d}$ after 150 μs ROL cooling. The average detuning is 5 Γ and the single-beam lattice intensity is 2 mW/cm^2. The simulation agrees well with experimental data displayed in Fig. 3.13. Bottom panel: Momentum distribution at $\Delta_{\rm d} = 300$ kHz.

we find that for the case $\Delta_d = 0$ the time required to cool the atoms is of order 50 μs. This suggests that lin-θ-lin cooling should be effective for detuning differences $\Delta_d \lesssim 50$ kHz. In agreement with this very simple estimate, we find experimentally that the lin-θ-lin cooling is effective for $\Delta_d \lesssim 100$ kHz.

The singular case $\Delta_d = 0$ corresponds to well-known Sisyphus cooling in a stationary lin-θ-lin lattice [26, 27]. In the experiment, the value of θ varies from one repetition of the lattice cooling to the next due to phase variations in the lattice beams caused by thermal and mechanical instabilities and air turbulence. Since the cooling data is typically collected over a period of order one minute, we assume that

the data for $\Delta_d = 0$ represents an average for a uniform probability distribution in θ. During any given repetition of the cooling, the phase θ is approximately constant. We find in the QMCWF simulations that the cooling efficiency and speed do not vary much over a range $\pi/16 \lesssim \theta \leqslant \pi/2$, while in the range $0 \leqslant \theta \lesssim \pi/16$ the cooling is slow and the steady-state temperature is of order twice the θ-averaged temperature. These findings explain another experimental observation: in the case $\Delta_{\rm d} = 0$, the cooling works well in most individual repetitions; in about one out of ten repetitions it apparently fails.

In the range 200 kHz $\lesssim \Delta_d \lesssim$ 500 kHz, the angle between the linear polarizations of the counter-propagating lattice beams rotates too fast for lin-θ-lin cooling to be effective. Also, Δ_d is not large enough for the sub-Doppler cooling mechanism of the ROL to be effective. As a result, in this range no significant cooling occurs. There is, however, some cooling into frames of reference moving at velocities of $v = \pm\lambda\Delta_d/2$ and $v = \pm\lambda\Delta_d/4$, identified by the dotted lines in Figs. 3.9 and 3.10. The accumulation of atoms at these velocities is most clearly seen in the side-structures in the bottom panel of Fig. 3.10.

The case $v = \pm\lambda\Delta_d/2$ can be interpreted as a cooling type similar to magnetic-field-induced laser cooling (MILC) [28], in which atoms are cooled into σ^+- or σ^--standing waves. For instance, the σ^+-standing wave generated by beams 1 and 3 of Fig. 3.3 moves at a velocity of $v = \lambda\Delta_d/2$. The atoms cooled into the light-shift potentials associated with that standing wave move at an average velocity of $\lambda\Delta_d/2$. To obtain Sisyphus-type laser cooling, some mixing is required between the states associated with the light-shift potentials generated by the moving σ^+-standing wave. In MILC, the mixing is provided by a weak transverse magnetic field [28]. In the present case, the mixing is provided by Raman couplings involving pairs of σ^+- and

σ^--beams in Fig. 3.3.

3.3 $\lambda/4$ Periodicity of the Raman Optical Lattice

In the previous section, the sub-Doppler cooling effect of the ROL was demonstrated by the momentum distributions of the atoms obtained from the TOF method. In this section, we provide experimental evidence of the $\lambda/4$ periodicity of the ROL.

3.3.1 Optical Mask Technique

To study the period of optical lattices, traditionally a Bragg scattering method [2, 29] is used. However, this method is virtually impractical in the ROL case since shorter-wavelength probe beams would be required. An alternative method, an optical mask technique, is therefore explored to study the ROL period. Not only can the optical mask technique, in principle, measure structures with periods of $\lambda/2n$, where n is an integer number, also it is relatively straightforward to implement based on the ROL setup.

An optical mask consists of a standing wave with a spatial period of $\lambda/2$ and a frequency close to resonance with an open atomic transition that optically pumps the atoms from an initial state F to an uncoupled state $\tilde{F}$. When applied to the atoms, the mask depletes the population of atoms in state F everywhere except in the narrow vicinity of the nodes of the mask (shown in Fig. 3.15). Assume initially the atomic density distribution has a period of $\lambda/2$. To map out this density distribution, the mask position is translated relative to the atomic spatial distribution. As shown in Fig. 3.15, the number of atoms remaining in state F depends on the mask translation and undergoes a full period when the mask is translated from 0 to $\lambda/2$. Thus, the population of atoms remaining in state F as a function of the mask translation has the same $\lambda/2$ period as the initial atomic spatial distribution. Alternatively, the

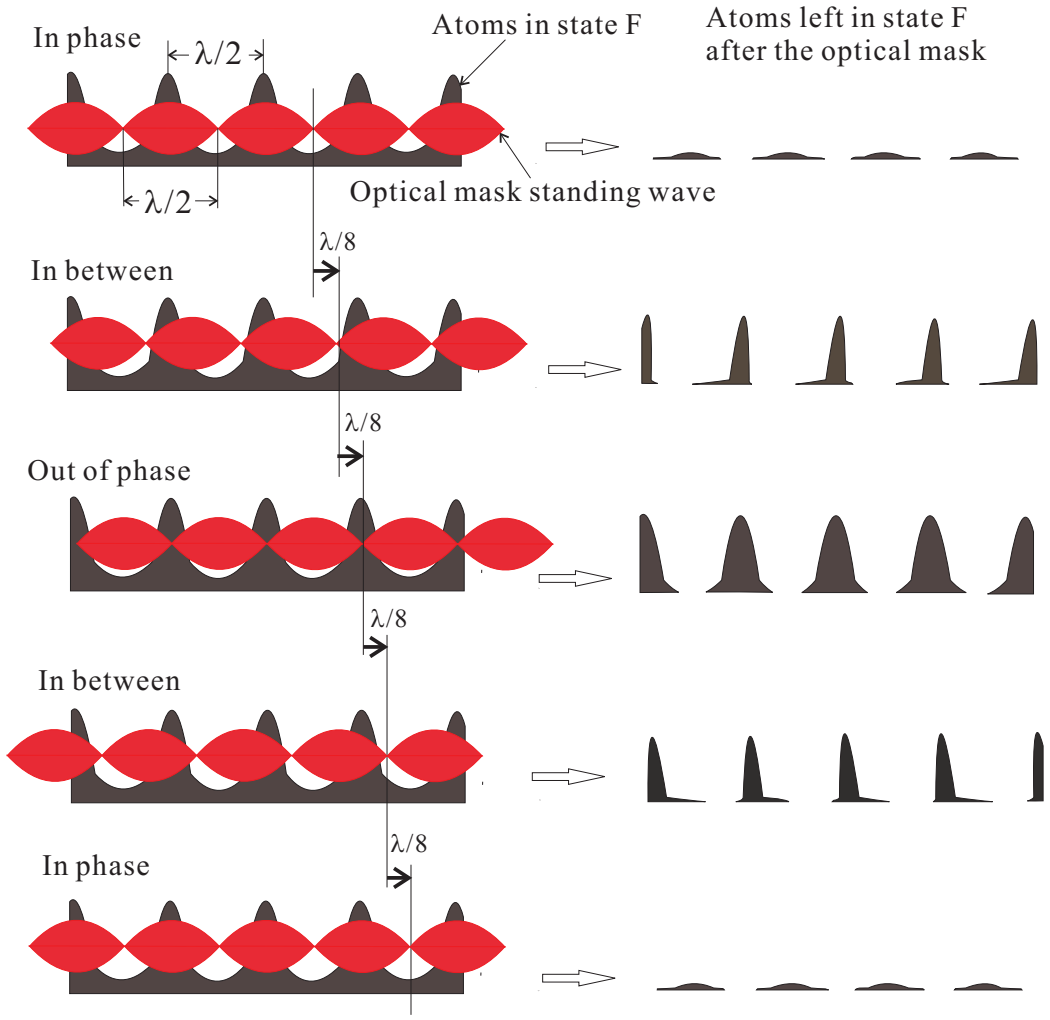

Figure 3.15: Top panel shows the anti-node of the mask standing wave overlaps with the atomic density peaks (in phase). As a result, most atoms in state F will be optically pumped to an uncoupled state $\tilde{F}$. Bottom panel indicates a $\lambda/4$ translation of the mask from that of the top panel (out of phase). In this case most atoms are left in state F since they experience little pump light near the nodes of the mask standing wave.

population transfered into state $\tilde{F}$ can be measured, as reported in our experiments.

The optical-mask technique can also be used to measure atomic distributions with smaller periods as long as the period is an integer fraction of that of the mask, *i.e.* the period is $\lambda/2n$, where n is an integer number. In these cases, the atomic densities at the locations of the mask nodes are always the same. Therefore, only one node of the mask standing wave needs to be considered since the rest should produce exactly the same results. Shown in Fig. 3.16 is the application of the mask to a $\lambda/4$ period

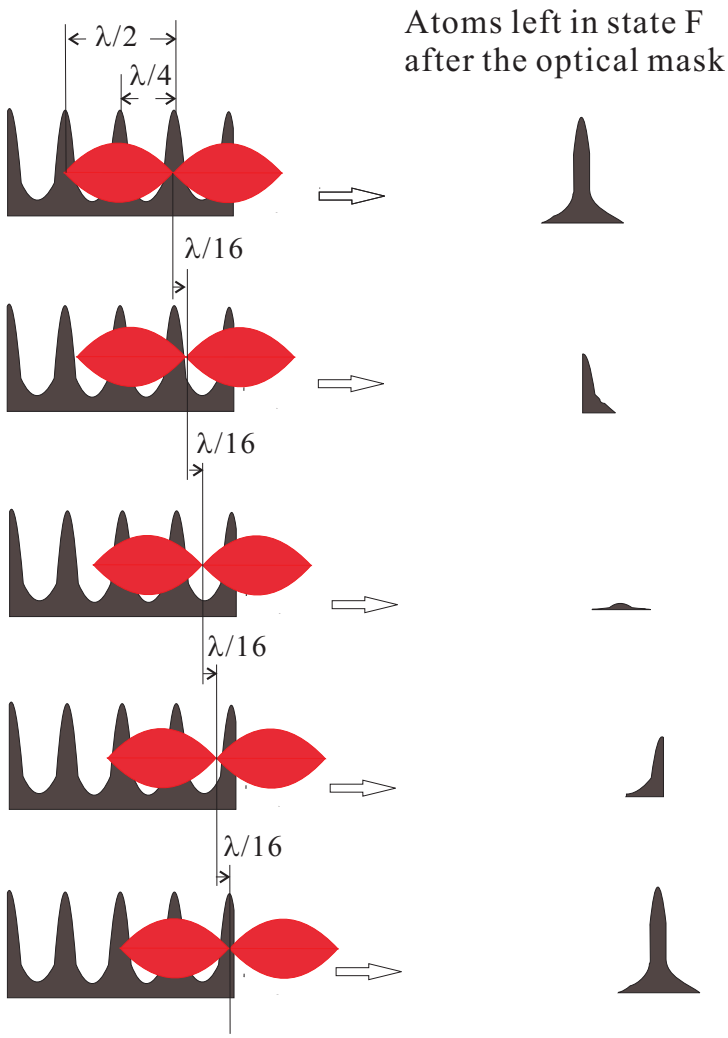

Figure 3.16: In case of applying the optical mask to an atomic distribution with a $\lambda/4$ period, a $\lambda/8$ translation of the mask leads to a half oscillation of atoms left in state F.

structure, where we can see that a $\lambda/4$ translation of one node of the mask standing wave produces a full oscillation of the population of atoms left in state F. The mask can, in principle, be used to measure periods with even larger n provided the standing wave intensity is strong enough, which determines the spatial resolution of the nodes of the standing wave. Using this optical-mask technique, atomic distributions with a period of $\lambda/2$ created by the mask itself [30], with a period of $\lambda/4$ produced by an atom interferometer [31] and with a period as small as $\lambda/10$ created by the Talbot-Lau effect [32], have been successfully imaged experimentally.

3.3.2 Application of the Optical Mask to a $\lambda/2$ Period Optical Lattice

The optical-mask technique is first tested in a $\lambda/2$ period optical lattice formed by magnetic-field-induced laser cooling (MILC). The MILC optical lattice consists of two counter-propagating circularly polarized laser beams with identical direction of field rotation relative to a fixed axis (*e.g.*, a left-circularly and a right-circularly polarized beam). This configuration forms a σ^+- or σ^--polarized standing wave with a period of $\lambda/2$. A weak transverse magnetic field, $B_\perp$, of order 100 mG mixes the magnetic sublevels of the atoms near the nodes of the resultant standing wave. A combination of light-shift-induced electric-dipole forces, magnetic-field-induced coupling near the field nodes and optical pumping leads to Sisyphus sub-Doppler laser cooling.

The MILC optical lattice drives exactly the same transition as the ROL ($5S_{1/2}$ $F = 1 \rightarrow 5P_{3/2}$ $F' = 1$ transition of ^{87}Rb). Hence, beam 1 and beam 3 of the ROL in Fig. 3.3(a) are used to realize the MILC optical lattice, except that now there is no frequency difference between these two beams. All the optics for the ROL remain unchanged for the mask experiment. A different RF circuit, however, is utilized to integrate the application of an optical mask after the optical lattice. The circuit is shown schematically in Fig. 3.17. During the lattice cooling phase, the RF switch in Fig. 3.17 is set to the upper input and the amplitude controllers are set such that each beam has an intensity of 1.5 mW/cm^2 at the location of the atoms. During the mask phase, the RF switch is set to its lower input and the amplitude controllers are set such that each mask beam has an intensity of 6.5 mW/cm^2. The spatial phase of the mask relative to that of the lattice is varied using an electronic phase shifter inserted into the RF-line for the mask (see Fig. 3.17). In this way, properly timed RF signals allow us to use the same beams to form both the lattice and the mask. The mask duration must be sufficiently short that the movement of the atoms is negligible

during the mask application. For a lattice period of 390 nm and atomic speeds of about 4 cm/s, the maximum allowable mask time amounts to about 2 μs. To ensure that masks of that duration generate sufficient optical pumping from $F = 1$ to $F = 2$, the mask fields must have a considerably higher intensity than the lattice fields.

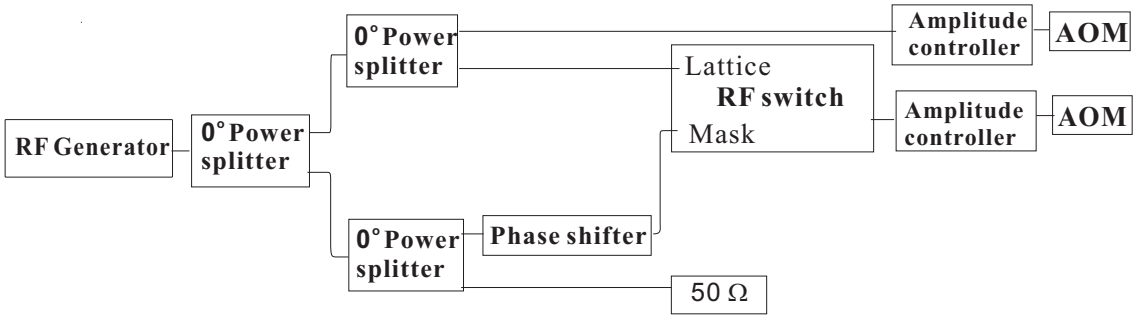

Figure 3.17: RF circuit used to rapidly switch from a MILC optical lattice to an optical mask. The phase difference between the lattice and mask beams is controlled by an electronic phase shifter.

The experiment runs at a repetition rate of 60 Hz. In each cycle, about 10^6 ^{87}Rb atoms are first collected in a 12 ms MOT and pre-cooled to about 50 μK using a 1 ms optical molasses. The MOT beams are switched off after the molasses cooling. The MILC lattice beams are then turned on for 150 μs to create a periodically modulated atomic density. Atoms are cooled to a temperature of about 15 μK, or an average velocity of about 4 cm/s, and localized at a period of $\lambda/2$ in the $F = 1$ ground state. After the lattice cooling, the repumper beams are switched off and the beams forming the lattice are switched from lattice mode into mask mode, as described above. The spatial phase of the mask relative to the MILC lattice is controlled by the phase-shifter. The optical mask is on for about 1 μs. During this time, atoms in the $F = 1$ hyperfine level are optically pumped into the $F = 2$ hyperfine level, unless they are in the vicinity of a node of the standing-wave mask field. To measure the effect of the mask, a traveling-wave probe beam of 15 μs duration and with frequency tuned to the $5S_{1/2}$ $F = 2 \rightarrow 5P_{3/2}$ $F' = 3$ transition is then applied to the atoms. The

resultant atomic fluorescence is collected by a lens (2 inch diameter and focal length) and focused onto a photodiode. The photocurrent is recorded and averaged using a transimpedance amplifier and a digital oscilloscope. The integral of the fluorescence signal is proportional to the number of atoms transferred by the mask into the $F = 2$ state. This state offers a closed probe transition that yields high fluorescence per atom. Since in the MILC lattice a small fraction of the atoms always resides in the probed level $F = 2$, we subtract the fluorescence signal obtained without application of the optical mask from the fluorescence signal obtained with the mask.

We average the fluorescence signals as follows. For each sampled spatial phase of the mask, 180 individual fluorescence traces are taken and averaged on the oscilloscope. These pre-averaged traces are temporarily stored, and the sampling is repeated until, for each sampled mask phase, 20 pre-averaged traces are obtained. The final signal consists of the average of these 20 pre-averaged traces. This averaging procedure minimizes the influence of slow drifts, such as fluctuations of the number of atoms in the MOT.

Two typical background-subtracted, averaged fluorescence signals are shown in Fig. 3.18 (a). Each curve is an average over 3600 individual fluorescence traces, obtained as explained above. When the maxima of the density distribution of the atoms in the $F = 1$ lattice state coincide with the anti-nodes of the mask standing wave (in-phase case), the fluorescence is much stronger than in the case in which the density maxima coincide with the nodes (out-of-phase case). In the in-phase case, the mask optically pumps more atoms into the probed state $F = 2$. The difference between the two cases shows that the atomic density distribution produced by the MILC optical lattice exhibits a significant modulation.

The number of atoms transferred into the $F = 2$ state is proportional to the

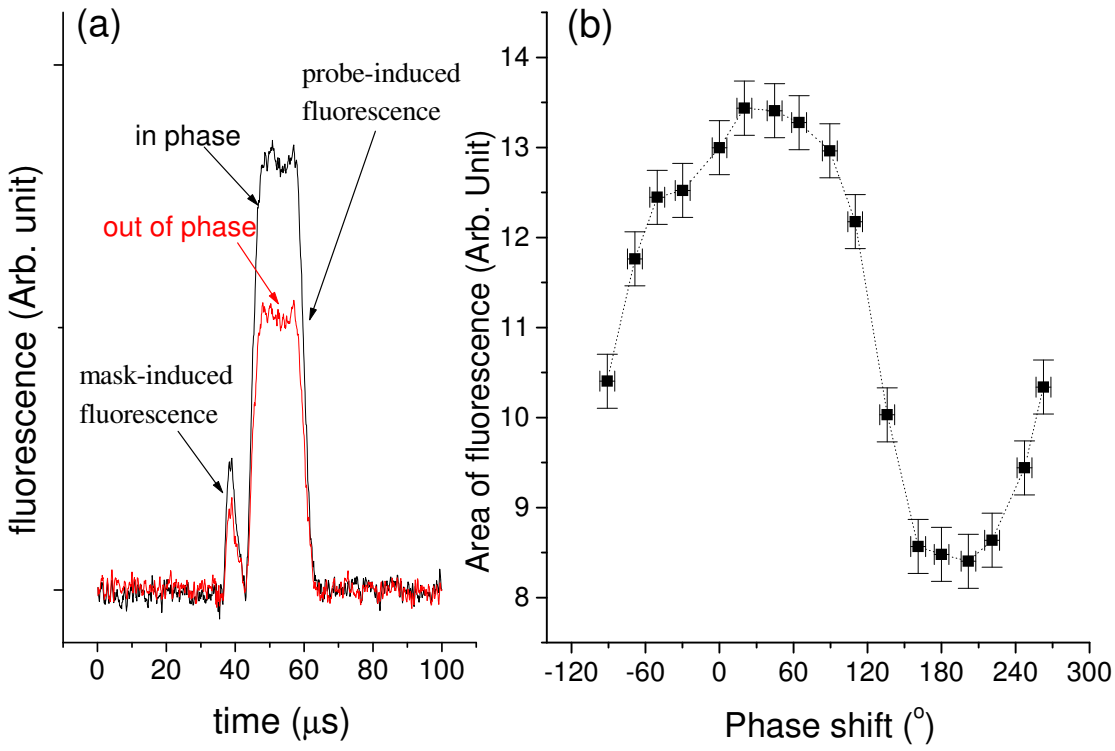

Figure 3.18: Analysis of a MILC optical lattice using an optical mask. The lattice operates on the $F = 1$ hyperfine level of ^{87}Rb, has a single-beam intensity of 1.5 mW/cm^2, a blue-detuning of 12 MHz with respect to the $5S_{1/2}$ $F = 1 \rightarrow 5P_{3/2}$ $F' = 1$ transition, and a magnetic field of 110 mG transverse to the lattice beams. (a) Atomic fluorescence vs time. The small peaks show atomic fluorescence caused by the mask action (*i.e.*, optical pumping from $F = 1$ to $F = 2$). In the in-phase case, the anti-nodes of the mask standing wave coincide with the peaks of the atomic density distribution produced by the MILC lattice. (b) Areas of the fluorescence signals such as those shown in (a) vs phase shift of the mask standing wave.

integral over the fluorescence peaks in Fig. 3.18 (a). In Fig. 3.18 (b) we show the integrals of the fluorescence as a function of the phase shift applied by the phase shifter. The sampled range of the mask phase shift is 360^o, which corresponds to a translation of the mask relative to the lattice by $\lambda/2$. In Fig. 3.18 (b) it is seen that the number of atoms transferred by the mask into $F = 2$ undergoes one oscillation period while the mask is translated by $\lambda/2$. This result shows that the period of the atomic-density modulation produced by the MILC lattice is $\lambda/2$, as expected. The actual shape of the fluorescence vs phase shift is a complicated function of several parameters including mask duration, atomic density distribution, and mask transfer

efficiency.

3.3.3 Application of the Optical Mask to the ROL

In the previous section, the $\lambda/2$ period of the MILC optical lattice is experimentally verified using the optical mask technique. Now we use this technique to investigate the period of the ROL.

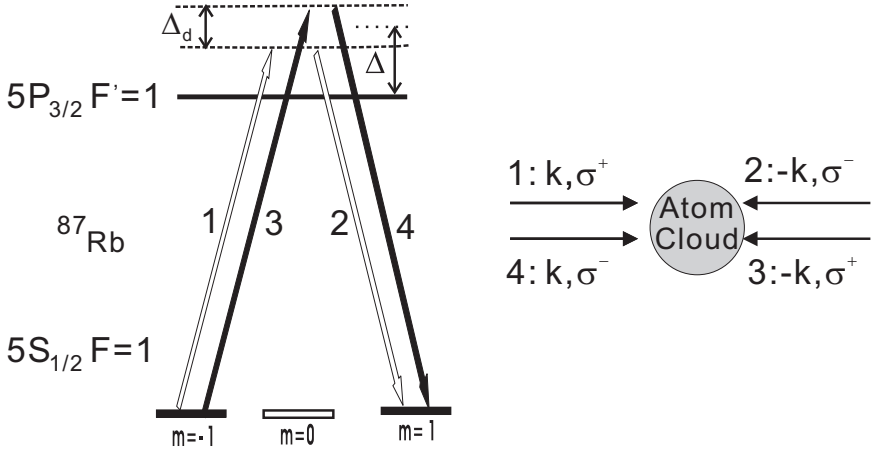

Figure 3.19: Transition diagram of the ROL and fields polarization and propagation.

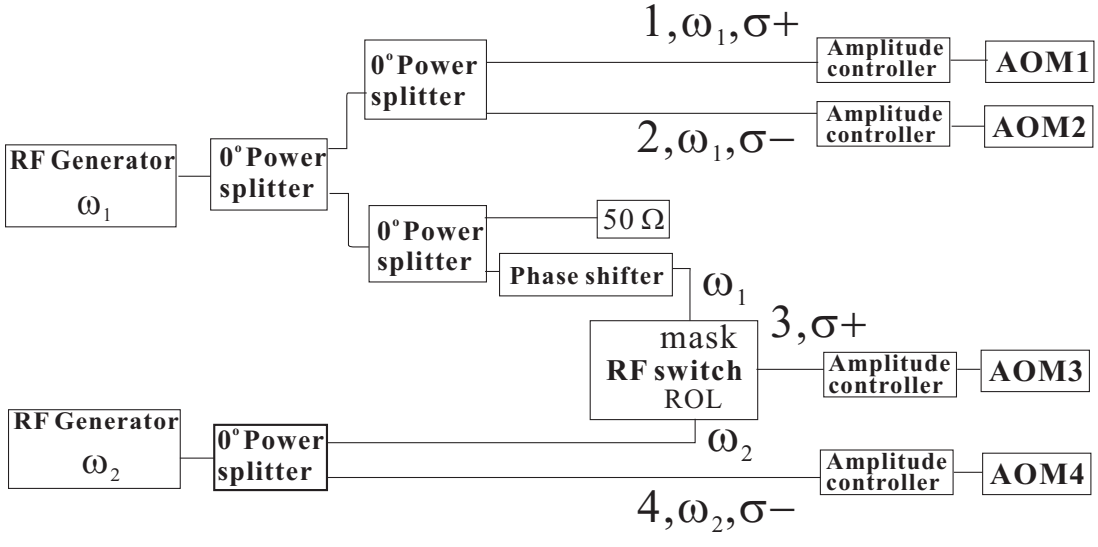

Figure 3.20: Diagram of the RF circuit used to apply an optical mask to the ROL.

Without the external magnetic field, the transition diagram of the ROL can be simplified as in Fig. 3.19. The field polarization and propagation (right panel of

Fig. 3.19) indicates that lattice beam 1 and 3 are suitable to form an optical mask standing wave. However, to satisfy the ROL condition, beam 1 and 3 can not have the same frequency. Therefore, an RF circuit is used to rapidly switch from the ROL beam frequencies to the mask frequency (RF circuit diagram shown in Fig. 3.20). The AOM numbers correspond to the laser beams shown in Fig. 3.11. Each RF line incorporates an amplitude controller; the controllers are used to switch the corresponding laser beams on and off, and to vary their intensities. During the ROL stage, the RF switch connects AOM 3 to the lower RF generator. Therefore, AOMs 1 and 2 are driven with an identical frequency ω_1, while AOMs 3 and 4 are driven with a frequency $\omega_2 = \omega_1 + 1.5$ MHz, in accordance with the ROL scheme in Fig. 3.11. During the optical mask stage, the RF lines driving AOMs 2 and 4 are turned off, while the RF switch connects AOM 3 to the upper RF generator. The resultant standing-wave light field formed by beams 1 and 3 can be used as an optical mask. The switching time of the RF circuit is 20 ns. The position of the mask standing-wave relative to that of the ROL can be varied by an electronically controlled phase-shifter that is located in the RF line driving AOM 3 during the mask phase. The RF power level during the mask phase is chosen such that each mask laser beam has an intensity of 6.5 mW/cm^2.

The steps of collecting and analyzing the mask fluorescence data for the ROL are identical to those used to analyze the MILC lattice. The resulting area of fluorescence vs the phase shift applied to one mask beam is plotted in Fig. 3.21 for six runs (as before, a phase variation of 360 degrees corresponds to a mask translation of $\lambda/2$). Panels (a)-(d) of Fig. 3.21 clearly exhibit two approximately equidistant peaks: when scanned over a distance of $\lambda/2$, the antinodes of the mask standing wave coincide twice with peaks of the atomic density distribution. This is indicative of

a $\lambda/4$ periodicity in the ROL atomic density distribution. The modulation depths of the curves in Fig. 3.21 (a)-(d) are about 5%. This low value is in qualitative accordance with the results of QMCWF simulations, which, for the lattice parameters chosen, indicate a modulation depth in the atom density distribution of about 13%. We believe that the discrepancy between the modulation depths measured in the fluorescence data and in the simulated atom density distribution is partially due to the fact that we use a $\lambda/2$-period mask to probe a structure with a $\lambda/4$-period. Due to the factor-of-two mismatch, during the measurement some spatial averaging will occur, leading to a loss in measured modulation depth. Another reason for a reduction of the modulation depth lies in experimental phase drifts, discussed below.

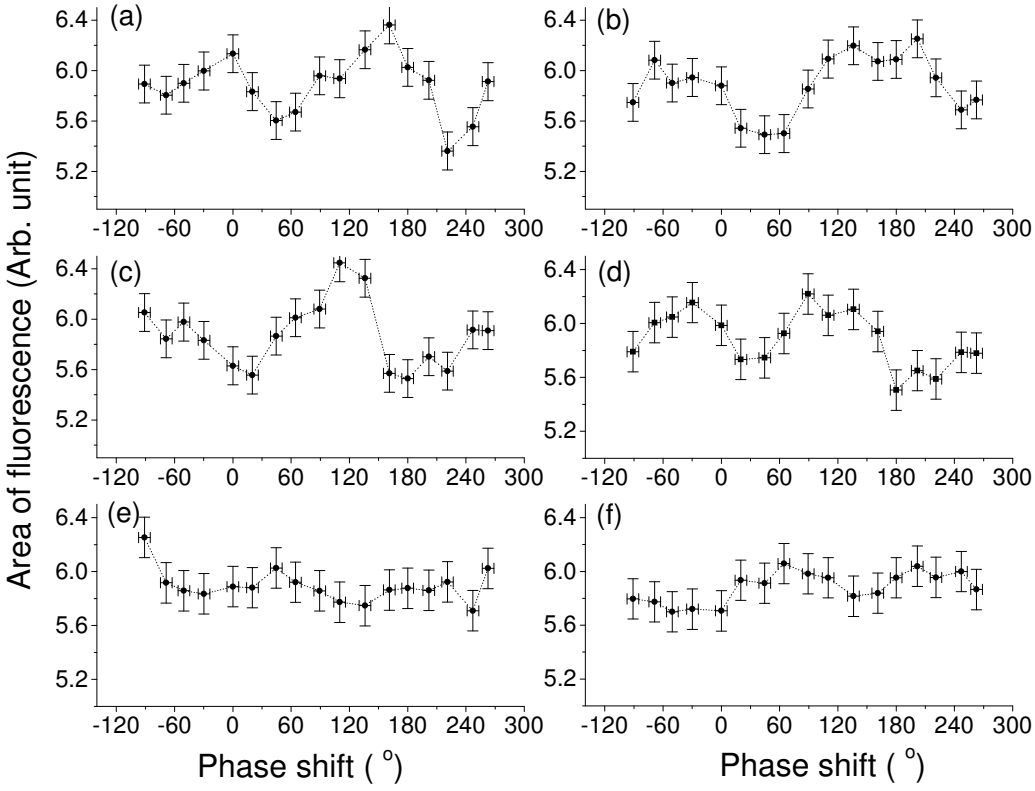

Figure 3.21: Areas of fluorescence vs phase shift of the mask standing wave obtained in the ROL. (a)-(f) are experimental results under the same experimental conditions.

Some measurements show only small modulation (see Fig. 3.21 (e) and (f)). We

think that fluctuations of the relative phases between ROL beams may be the main reason for the occasional loss of modulation. Phase fluctuations also explain why, among the data that do show modulations, the peaks do not line up perfectly from plot to plot (see Fig. 3.21 (a) - (d)). While slow phase variations do not affect sub-Doppler cooling in the ROL, they do shift the atomic distribution. If we assign an individual phase to each lattice beam and neglect decay due to spontaneous emission, we find an effective Hamiltonian for the lattice potential of:

$$\begin{aligned} H_{\text{effective}} &= \frac{\hbar}{2}\begin{pmatrix} \delta & r \\ r & -\delta \end{pmatrix} \\ \text{with} \quad r &= \frac{4\chi^2}{\Delta}\cos(2kz + \frac{\varphi_1 + \varphi_4 - \varphi_2 - \varphi_3}{2}) \end{aligned} \tag{3.3}$$

where φ_i is the phase of the ith lattice beam and δ is the Raman detuning ($\delta = 0$ in this experiment). It is apparent in Eq. 3.3 that the location of the ROL potential is affected by the phase term $\varphi_1 + \varphi_4 - \varphi_2 - \varphi_3$. The subsequent optical mask, however, is formed by beams 1 and 3 alone. Thus, the position of the optical mask is only determined by φ_1 and φ_3', where φ_3' may differ from φ_3 since the respective RF paths in Fig. 3.15 are different. All phases vary in time because the corresponding laser beams have different optical paths and propagate through different fibers or in different fiber modes. The phase variations are caused by thermal and mechanical instabilities and air turbulence. Since the position of the ROL potential depends on the phase combination $\varphi_1 + \varphi_4 - \varphi_2 - \varphi_3$, while the mask position depends on φ_1 and φ_3', the phase fluctuations result in uncontrolled drifts of the mask position relative to that of the ROL potential. Since each data set shown in Fig. 3.21 takes about twenty minutes to accumulate, it is likely that phase fluctuations are the main reason why in some data sets of Fig. 3.21 there is no clear modulation.

3.4 Conclusion

In this chapter, we have demonstrated experimentally both the sub-Doppler cooling [33, 34] and the $\lambda/4$ periodicity of the ROL [35]. The dependence of the ROL cooling on different lattice parameters is characterized and compared with the QM-CWF simulations. We use an optical mask technique to probe the density distribution of atoms inside the ROL. The experimental results show a clear signature of $\lambda/4$ periodicity.

CHAPTER IV

Bose-Einstein Condensate

4.1 Introduction

A Bose-Einstein condensate (BEC) is an ensemble of atoms that is cooled to such a low temperature that they all collapse into the same lowest quantum state. Therefore, although being a many-body system, the BEC can be described by a single wavefunction and hence displays quantum effects on a macroscopic scale. This condensation phenomenon was first predicted by Bose and Einstein in 1925, and was first achieved in dilute alkali gases through a series of experiments in 1995 [36–38].

The condition for the BEC to occur in a free space dilute gas is that the deBroglie wavelength of each atom, λ_{dB}, associated with its thermal motion extends over one another. In other words, the spatial density n of atoms has to satisfy

$$n\lambda_{dB}^3 \geq 2.612\,. \tag{4.1}$$

For atoms confined in a harmonic trap, however, the BEC condition is slightly different and is given by [39]

$$N(\frac{\hbar\bar{\omega}}{k_B T})^3 \geq 1.202\,, \tag{4.2}$$

where N is the atom number, $\bar{\omega}$ is the geometric mean trapping frequency, k_B is the Boltzmann's constant and T is the thermal temperature of the atoms.

Neglecting the interaction between atoms in a condensate, the Schrödinger equation governing the atomic motion is simply a linear one. However, since atoms do interact, this interaction has to be considered in the Schrödinger equation. A widely used approximation is to treat the interaction as a mean-field force. Under this treatment, the potential associated with the interaction is proportional to the local density of atoms. If the BEC is described by the wavefuction $\Psi(\mathbf{r})$, the density is simply $|\Psi(\mathbf{r})|^2$, which means that the Schrödinger equation is no longer linear. The resultant non-linear Schrödinger equation is often referred to as a Gross-Pitaevski equation [40, 41]. It takes the following form

$$i\hbar\frac{\partial\Psi(\mathbf{r},t)}{\partial t} = [-\frac{\hbar^2}{2M}\nabla^2_{\mathbf{r}} + V_{ext}(\mathbf{r}) + NV_{int}|\Psi(\mathbf{r},t)|^2]\Psi(\mathbf{r},t)\,, \tag{4.3}$$

where M is the atomic mass, $V_{ext}(\mathbf{r})$ is the external potential and V_{int} characterizes the strength of the mean field interaction between the atoms, defined as $V_{int} \equiv 4\pi\hbar^2 a/M$, with a being the s-wave scattering length of the atom.

Many properties and behaviors of the BEC inside external potentials can be solved theoretically based on the Gross-Pitaevski equation. This relatively simple model has sparked a considerable amount of theoretical interest in studying BECs in different types of external potentials, such as a harmonic trap [42–44], a light field inducing Raman transitions [45], an optical lattice [46–48] and a polarization potential created by ions [49]. Experimentally, the macroscopic quantum properties of the BEC and its easy manipulation and control by optical or magnetic approaches have triggered even larger excitement. Experiments involving BECs have dealt with fundamental properties of BECs [50–55], BECs in optical lattices (for a review, see Ref. [56]), atom interferometers using BECs [57–60] and the interaction of BECs with other entities [61–63]. The achievement of the BEC has led to a new frontier for physics research.

We have long been aware of the importance of BECs. Starting in 2004, we made our initial plan to build the first BEC apparatus at the University of Michigan. In September 2005, we started the construction of the BEC chamber and in February 2007, we observed the first BEC in our laboratory. In this chapter, I will describe our BEC apparatus and the pathway towards the BEC.

4.2 Experimental Setup

4.2.1 Vacuum Chamber

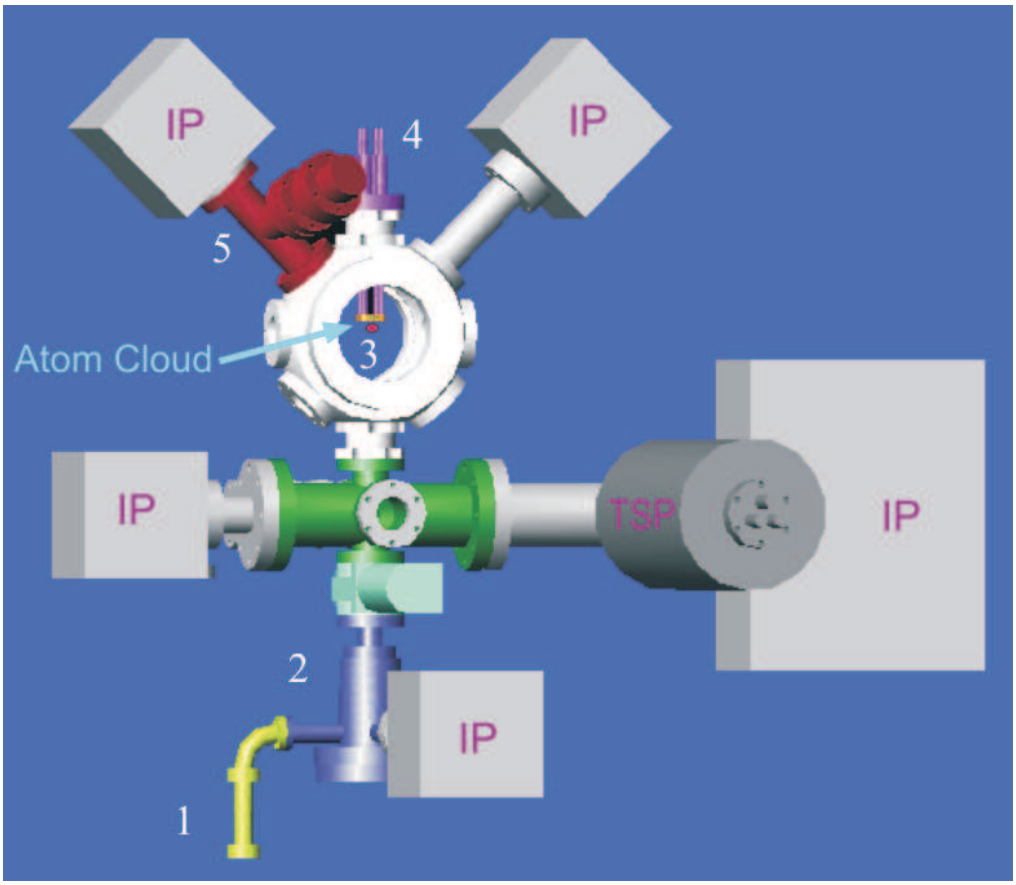

Figure 4.1: The vacuum chamber for the BEC experiment consists of three main parts: the low-vacuum primary chamber (labeled 2), the intermediate pumping stage and the high-vacuum secondary chamber (labeled 3).

The single chamber design of our old vacuum system for the ROL is not compatible to the BEC experiment, because achieving a BEC generally simultaneously requires

a large number of trapped atoms and a low background collision rate. These two are usually conflicting requirements inside a single chamber. Therefore a new vacuum system was constructed for the BEC experiment. Like most other BEC systems, the new vacuum chamber consists of three main parts as shown in Fig. 4.1. The first part is the primary chamber, with components 1 and 2. Component 1 is the rubidium reservoir which provides Rb atoms in vapor form. The background vapor pressure inside the primary chamber is $\sim 10^{-8}$Torr since only one $20L/s$ ion pump pumps the primary chamber directly. About 10^9 ^{87}Rb atoms can therefore be collected by a magneto-optical trap (MOT)inside the component 2. The trapped atoms are transported into the secondary chamber (component 3) after passing a gate valve.

Between the secondary chamber and the primary chamber is a differential pumping stage, which is a combination of two ion pumps and a Titanium sublimation pump. This stage is very important for maintaining the ultra-high-vacuum (UHV), below 2×10^{-11} Torr, inside the top chamber, while the lower chamber is kept at a much higher pressure so that enough atoms can be collected.

Inside the secondary chamber, component 3, is where the BEC is created. Two 20 L/s ion pumps are connected to this chamber, where the vacuum pressure is below 2×10^{-11}Torr. Another magneto-optical trap is set up inside component 3 to recapture the transported atoms from the primary MOT. In this way more than 10^9 ^{87}Rb atoms can be collected while the background pressure is kept below 2×10^{-11}Torr. Component 4 contains four current feedthroughs, which carry currents into the vacuum chamber to create the necessary magnetic fields for the BEC experiment. A detailed discussion about the MOT beam and magnetic field setup is given in the following section.

To reach a vacuum below 10^{-8} Torr, the entire chamber has to be baked around

100^oC for a couple of days. For our secondary chamber, where the vacuum is required to be below 10^{-11} Torr, we baked it at a temperature up to 250^oC for a week. The detailed discussion about baking and vacuum parts cleaning can be found elsewhere [64]. One comment I would like to emphasize regarding the vacuum issue is that if you plan on reaching 10^{-11} Torr vacuum, a Titanium sublimation pump (TSP) is absolutely necessary. Our first trials of the vacuum chamber were without a TSP. No matter how hard we baked the chamber, the vacuum would not go below 8×10^{-10} Torr, even after several months. After the TSP was mounted, the vacuum went down to 3×10^{-11} Torr in one day after the bake-out.

4.2.2 Double MOT Setup

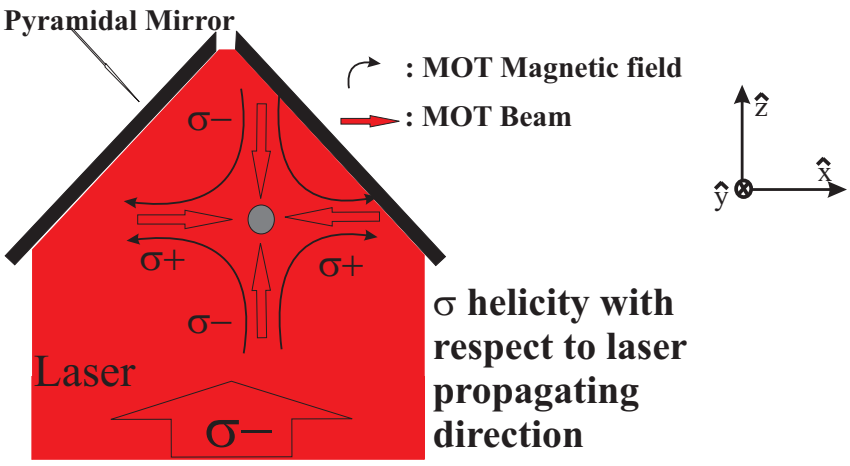

Figure 4.2: The primary pyramidal MOT beam and magnetic field configuration. The six beams are created by a single circularly-polarized incoming field bouncing off four mirrors in a pyramidal structure. The helicity of the beams are automatically satisfied for a MOT configuration. The MOT magnetic field is produced by two anti-Helmholtz coils in vertical (z) direction. Show here is a x-z plane plot of the pyramidal MOT setup. The configuration is the same in y-z plane.

The primary MOT is a so-called pyramidal MOT [65]. A pyramid-shaped metal mirror is located inside component 2 with the reflective sides facing downwards, as shown in Fig. 4.2. A two-inch-diameter laser beam is sent upwards and reflected by the four walls of the pyramidal mirror, creating six counter-propagating beams for the MOT. The incoming beam is circularly polarized and after each reflection changes to

the opposite helicity with respect to its propagation direction. This guarantees that the final 6 MOT beams have the correct polarization. The MOT magnetic field is created by two anti-Helmholtz coils in the vertical (z) direction. Two compensation coils may be required in x- and y-directions to adjust the location of the magnetic field to match that of the 6 MOT beams. At the apex of the pyramidal mirror, a small (about 1 mm in diameter) aperture is drilled. When the MOT is located right under this aperture, due to the radiation pressure imbalance a portion of the trapped atoms will be pushed upwards through the aperture by the upward MOT beam. This produces a cold atom flux for the secondary MOT shown in Fig. 4.3.

The secondary MOT is located underneath a gold-coated silicon mirror [66] attached to a copper structure at the end of the current-feedthrough in the top chamber. Two MOT beams with opposite helicity are brought into the chamber from both sides at 45 degrees with respect to the mirror surface as indicated in Fig. 4.3. After bouncing off the mirror, both beams counter-propagate with each other. These two beams and their reflections, together with another counter-propagating pair of beams in the y-direction, form the optical geometry of the secondary MOT. The magnetic field of the secondary MOT is first created by two external coils placed such that the axis of the coils is aligned with one of the 45^o MOT beams. These 120-turn coils are in an anti-Helmholtz configuration and, with a 5 A current, can provide a magnetic field gradient of about 10 G/cm around the MOT location. This intermediate MOT is on for up to 16 s to capture $\sim 10^9$ atoms.

The MOT magnetic field can also be generated by running a current through a "U" shaped wire and using a uniform bias magnetic field [67]. The U-shaped wire is part of the copper structure mounted to the end of the current-feedthrough as shown in Fig. 4.4 (a). The copper structure is a 1" $\times$ 1" $\times$ 0.25" piece. It has a "H" shaped

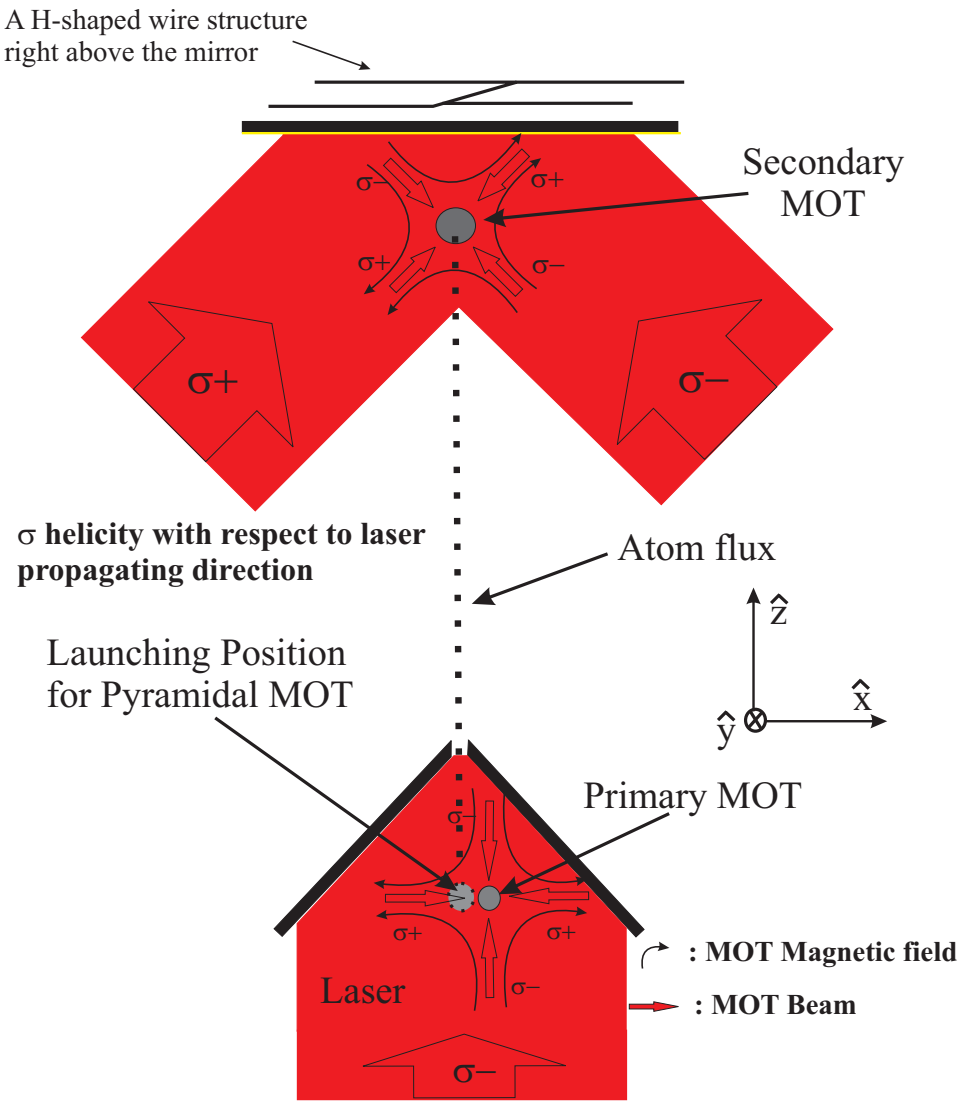

Figure 4.3: The schematic drawing of the secondary MOT setup. The distance between two MOTs is about 35 cm.

square wire at the center with the separation between two legs of either 7mm (1 and 2) or 5mm (3 and 4). The four ends of the "H" wire are connected to the four current feedthroughs with good electric contact. When a current is sent through electrodes 1 and 2, a U-shaped current is generated; when instead 2 and 3 are connected, we can realize a Z-shaped current which will be discussed later. The square wire has a dimension of $1.4mm \times 1.4mm$, which ensures that no significant heat is generated for a current of up to 60A. The H-wire design in our experiment is similar to that

described in Refs. [68, 69].

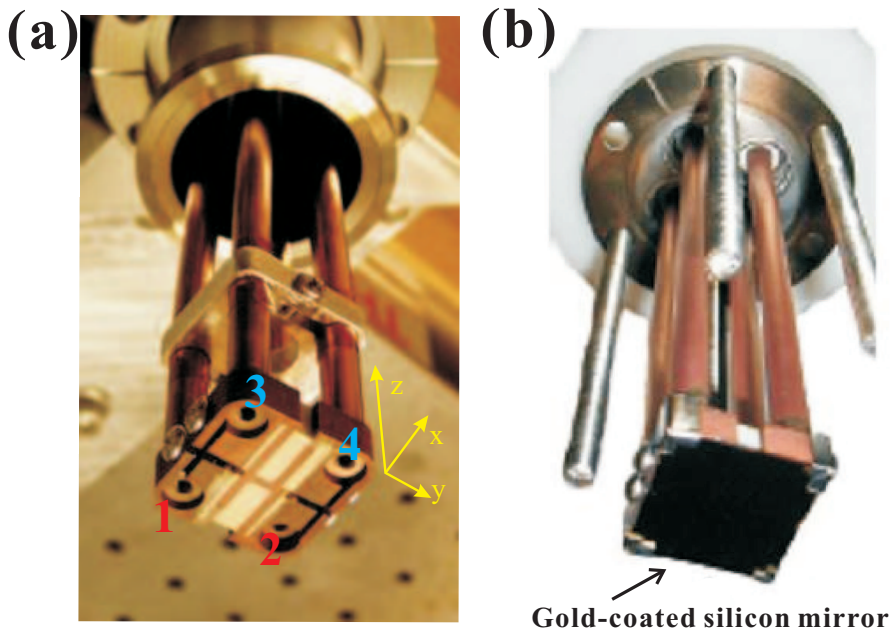

Figure 4.4: (a) A "H" shaped wire is machined at the center of the copper structure. The four ends of "H" are connected to four current feedthroughs. (b) The gold mirror is attached to the bottom of this copper structure.

To understand how the "U" wire trap functions, we first consider the field of a single wire in the y-direction and a uniform bias field B_o in the x-direction. The superposition of these two fields forms a two-dimensional quadrupole potential in the $x-z$ plane, qualitatively shown in Fig. 4.5. To obtain a three-dimensional trap, the wire is bent into a "U" shape. The field due to the two legs has a y component, which provides a trapping potential in the y-direction. Thus a three-dimensional trap is formed and referred to as a U-trap. Note that the field components in y-direction cancel at the center of the trap. Therefore the U-trap is a quadrupole potential with a zero magnetic field at the center. When the copper structure is aligned such that the center bar of the H-wire is along the y-direction and four legs are in the x-direction,

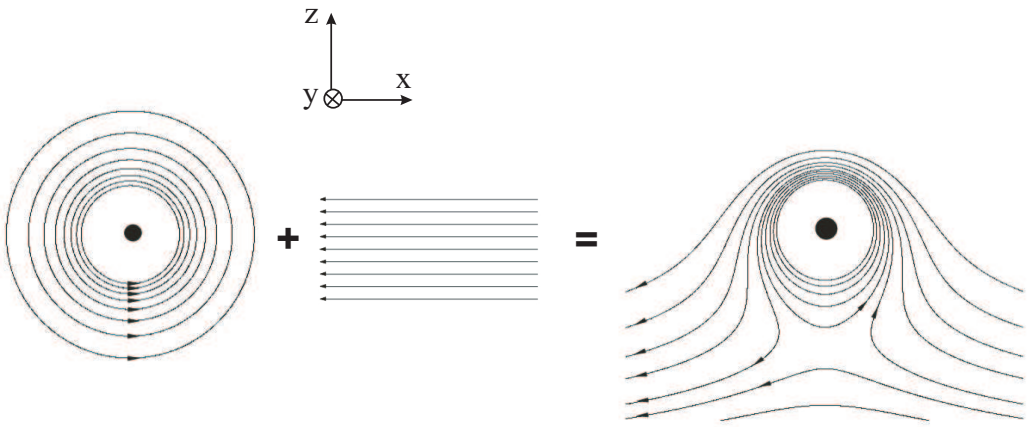

Figure 4.5: The superposition of a uniform field and a field generated by a single wire. As a result a two-dimensional quadrupole potential is formed.

the U-trap has exactly the same topology as the magnetic potential generated by the external coils shown in Fig. 4.3. For a current I and a bias field B_o, the U-trap is located at a distance r_o given by

$$r_o = \frac{\mu_0}{2\pi}\frac{I}{B_o} \tag{4.4}$$

underneath the wire and the magnetic field gradient at the trap center can be calculated to be

$$\nabla B(r_o) = \frac{2\pi}{\mu_0}\frac{B_o^2}{I}\,. \tag{4.5}$$

The U-MOT and the intermediate MOT share the same laser beams due to the same topology of their magnetic field. However the U-trap can have a much higher magnetic field gradient, which leads to a much denser atom cloud. But because of the small dimensions of the U-wire, the U-MOT can only capture a small number of atoms. That is why the intermediate MOT is needed in our experiment.

4.2.3 "Z" Trap

The typical temperature for a BEC transition to occur is around several hundred nano kelvin, which is not attainable by traditional laser cooling methods. Therefore an alternative cooling mechanism, evaporative cooling, is applied. The basic idea of evaporative cooling is to preferentially remove higher energy atoms inside an atomic assembly, and allow the remaining atoms to reach a lower equilibrium temperature by elastic collisions. For atoms trapped by a magnetic field, a straight-forward way to do evaporative cooling is to lower gradually the trap depth. The quadrupole trap described in the previous section, however, is not compatible with evaporative cooling since it has a magnetic field zero at its center. The Majorana spin-flip around a zero magnetic field causes a large atom loss, especially for cold atoms because they tend to stay at the bottom of the trap.

To avoid the Majorana spin-flip, a nonzero magnetic field has to be present at the bottom of a magnetic trap, which can be generated by the Z-shaped current [67] mentioned in the previous section. The "Z" current and the bias field B_o produce the same two-dimensional trap in the x-z plane as the U-trap. In the y-direction, however, contributions from the two legs of the Z-wire add up. As a result, the final field has a nonzero y component at the trap bottom. To obtain a more quantitative understanding, we simulate the Z-trap magnetic field based on the Biot-Savart law. The Z-wire is first divided into 3 straight segments, and each segment is then divided into 9 parallel current elements with smooth current distributions. The feedthroughs, which carry the current into the vacuum chamber, are also each divided into 32 parallel current elements. The magnetic field of each current element is calculated and the final Z-trap field is obtained by summing over all current elements. The effect of gravity is taken into account in the simulation by introducing a constant

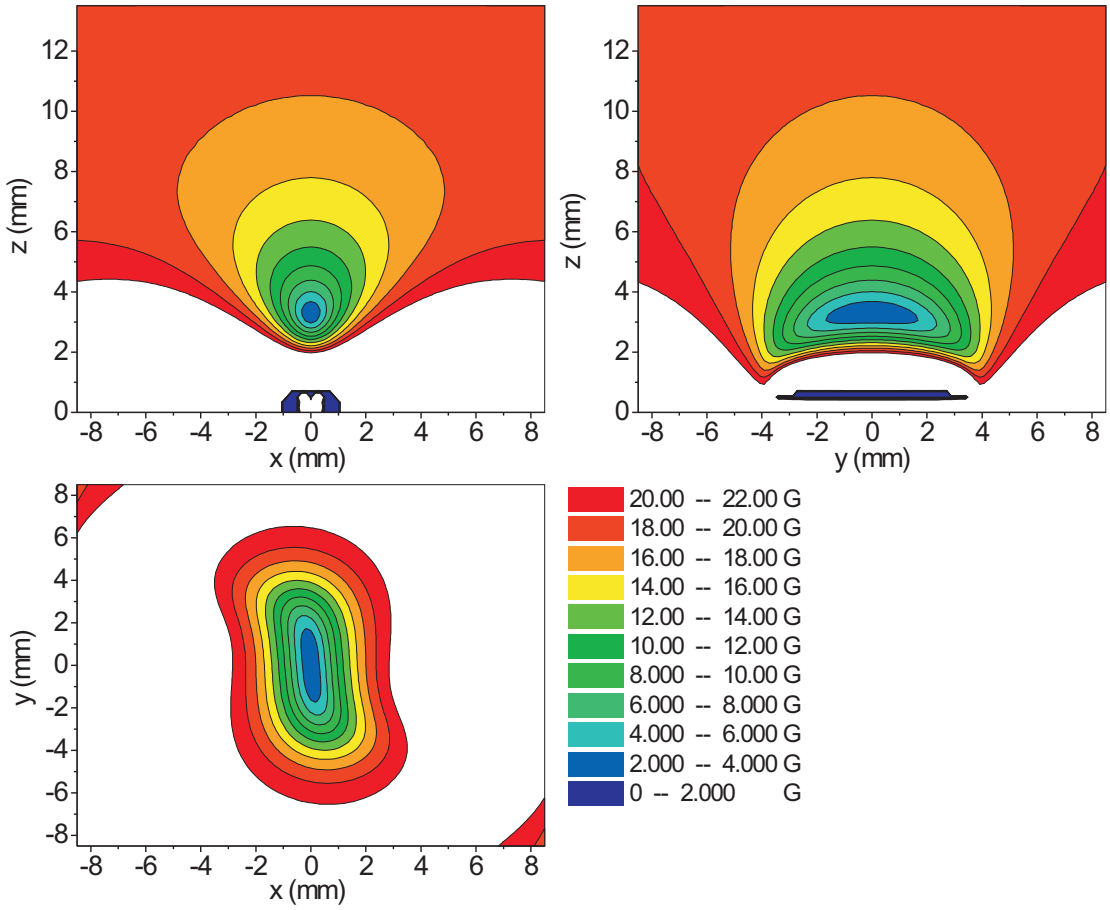

Figure 4.6: The simulated Z-trap magnetic field plotted in 2-D on 3 orthogonal planes. The color represents the magnitude of the magnetic field as indicated by the number of the lower panel. The numbers are in unit of Gauss.

field gradient in the vertical direction. Fig. 4.6 shows the simulated Z-trap field for a current of 54 A and bias magnetic fields of (17 G, 7 G, 0 G) in (x-, y-, z-) directions. The field is plotted in 2-D with the origin located at the center of the Z-wire. The magnitude of the field is represented by colors in steps of 2 Gauss. As seen the Z-trap has a nonzero magnetic field at its minimum and is much tighter in x- and z-direction than in y-direction.

One of the important parameters of a magnetic trap is its oscillation frequency. In the vicinity of the trap center, we can usually treat it as a harmonic trap. Under

this approximation, the trap frequency in a certain direction i is given by

$$\omega_i = \sqrt{\frac{\mu_B \nabla_i^2 B}{M}}, i = x, y, z\,, \tag{4.6}$$

where $\mu_B = 9.274 \times 10^{-24} J \cdot T^{-1}$ is the Bohr magneton, M is the mass of the ^{87}Rb atom. From simulations, we can figure out $\nabla_i^2 B$ at the center of the Z-trap for parameters given in Fig. 4.6. The trap frequencies in (x, y, z) directions are then calculated to be $2\pi\times$(54 Hz, 15 Hz, 54 Hz) based on the Eq. 4.6. In section 4.4, we will show that the trap frequencies can be experimentally measured. By comparison, we are able to prove the accuracy of the simulations.

4.2.4 Laser System and Optics

We have two home-made Tapered Amplifier (TA) systems for the BEC experiment, one for each MOT setup. The TA diode, from Eagleyard Photonics, is designed to have a maximum CW output of 1W. The wavelength of the TA output beam is determined by a master diode laser, which seeds a beam of around 15 mW into the TA diode. The master diode laser is frequency stabilized by the standard saturation spectroscopy method. The TA diode works for a broad range of wavelengths. In fact, for one TA system, we seed both MOT and repumper beam into the TA diode, and both beams get amplified. The detailed information about the TA design is described elsewhere [70]. In addition to the TA systems, we have another diode laser, from New Focus, which provides optical pumping and shadow image beams.

Fig. 4.7 shows schematically the laser systems and the optical setup. As shown, all laser beams, before being directed into the chamber, pass through optical fibers to achieve a gaussian intensity profile. The secondary MOT beam goes through an acousto-optic modulator (AOM) twice before the fiber, which enables us not only to switch the beam but also to control the beam intensity and frequency by changing

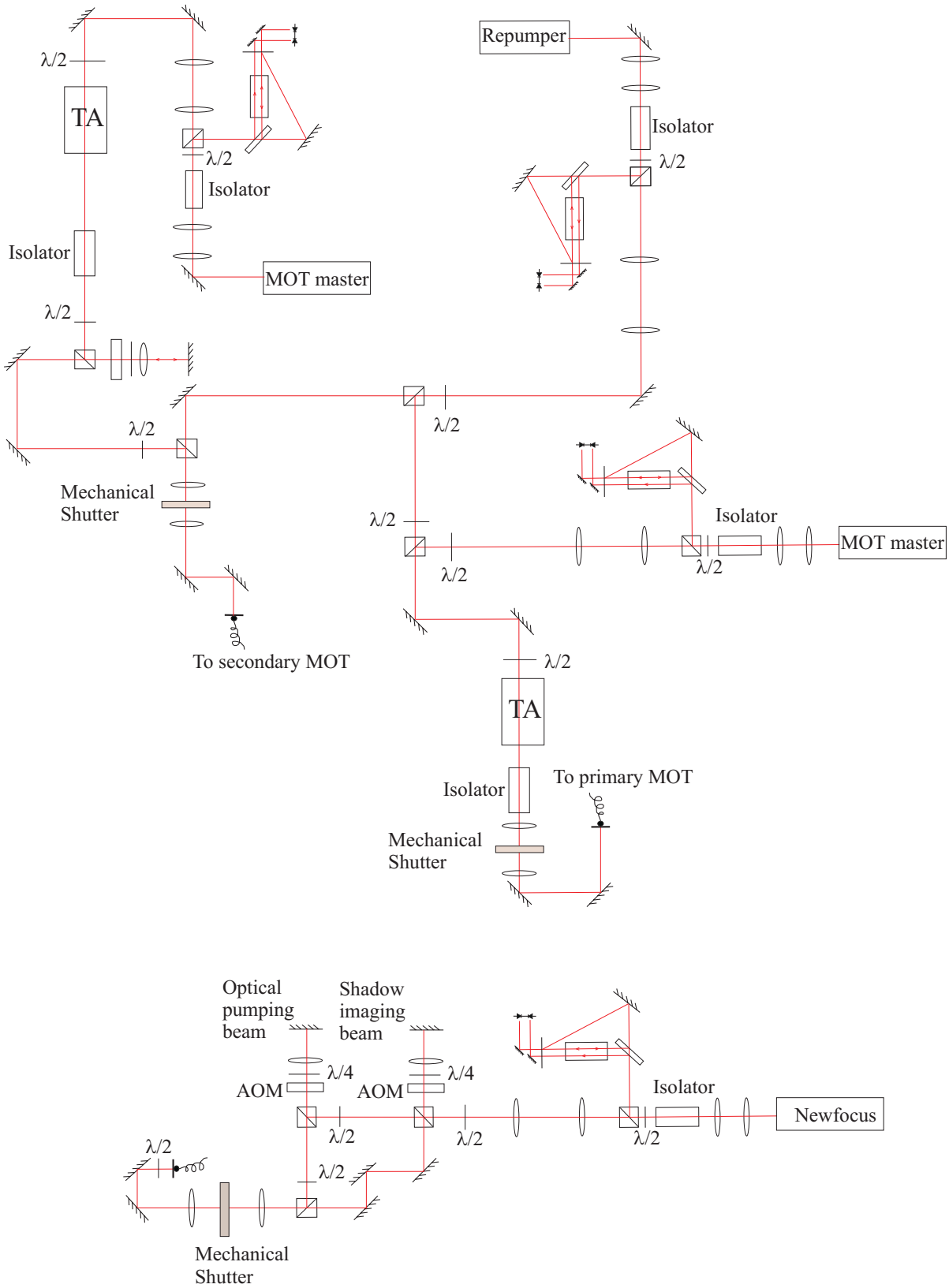

Figure 4.7: The schematic drawing of the optical setup for the BEC experiment

the RF signal driving the AOM. The optical pumping and imaging beams have the same AOM setup. After the AOMs, they are combined by a polarization cube and coupled into two orthogonal modes of a polarization maintaining fiber. To ensure that no near-resonant light leaks into the chamber during the offstage of the beams, mechanical shutters are necessary to back up the AOM switching, since AOMs cannot completely extinguish the light. The repumper light and the primary MOT beam are switched only by mechanical shutters.

4.2.5 Power Supply System

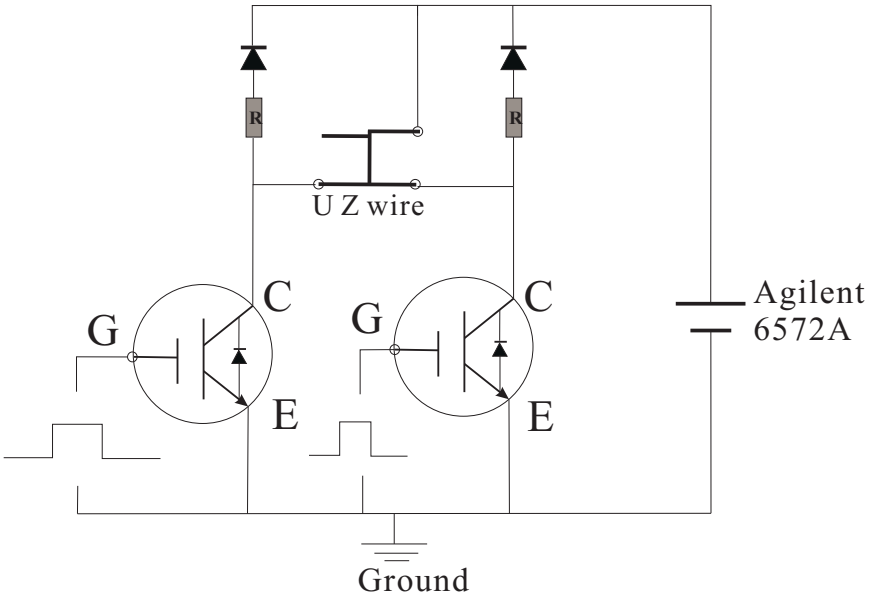

Figure 4.8: The IGBT circuit used in the BEC experiment to switch "U Z" currents. The control signal is applied between Gate and Emitter of the IGBT.

All magnetic fields involved in our experiment are generated by currents. Therefore we need a number of affordable current sources with not only a good stability but also a fast-switching ability. The Kepco ATE power supplies are good candidates. In the fast current-control mode, the typical peak-to-peak output fluctuation is less than 0.1% of the maximum output and the switching time constant is less than $100\mu s$, assuming a load with a small conductance. All currents generating magnetic

fields are controlled by the ATE power supplies except the "UZ" currents. The "UZ" wires are connected to an Agilent DC power supply model 6572A with a 20V-100A maximum output. The DC power supply is set at a constant voltage and its current is switched by insulated-gate bipolar transistors (IGBT). The circuit diagram is displayed in Fig. 4.8. For a certain Collector-Emitter voltage, the Collector-Emitter current of a IGBT is determined by the Gate-Emitter voltage. Therefore when the "H" wire is connected in series with the Collector-Emitter of the IGBT, the "UZ" current can be varied by the voltage applied between the Gate and the Emitter, as shown in Fig. 4.8. The IGBT used in our experiment is model APT100GF60JRD.

4.2.6 Timing-control System

Our main timing-control instrument is a computer-controlled TTL pulse card, PulseBlasterESR-PCI. The card can output 21 independent TTL signals with a 4ns resolution. These TTL signals, however, do not control the other apparatus directly since their amplitude cannot be varied. Instead we built a number of 4-channel multiplexer (MUX) circuits, which accept two TTL signals to select one of the 4 channels as the output. The amplitude of each channel is controlled by a voltage divider. The outputs from the MUX are then used to control most power supplies generating magnetic fields and all AOM drivers switching optical fields. The only disadvantage of the MUX is that it cannot output waveforms other than square-shaped, such as a triangle wave or a sinusoidal wave. To obtain a more complicated control signal, we use an arbitrary function generator, Agilent model 33220A. The arbitrary wave generator is externally triggered by one channel of the TTL card and outputs a user-defined waveform. It is worth mentioning that the Agilent 33220A has only 64 K data points for the arbitrary waveform, which turns out to present a slight problem for our experiment. Since it can take up to 30 s to produce a BEC in the

experiment, the shortest time step for the arbitrary waveform is only about 0.5 ms for a total of 64K data points. However some critical steps in the BEC production are in ms range or even much less, like the $100\mu s$ optical pumping stage. As a result, the 64 K data points cannot always guarantee a timing match-up between the control signals from the MUX circuit and the function generator. In the future, the function generator should be upgraded to at least 512 K memory for the arbitrary waveform. The Agilent 33220A can also produce a linear or logarithmic frequency sweep within its frequency limit, 1 μHz to 20 MHz. Therefore it is also used in our experiment to generate a RF signal for evaporative cooling.

4.3 Useful Experimental Techniques

4.3.1 Absorption Imaging

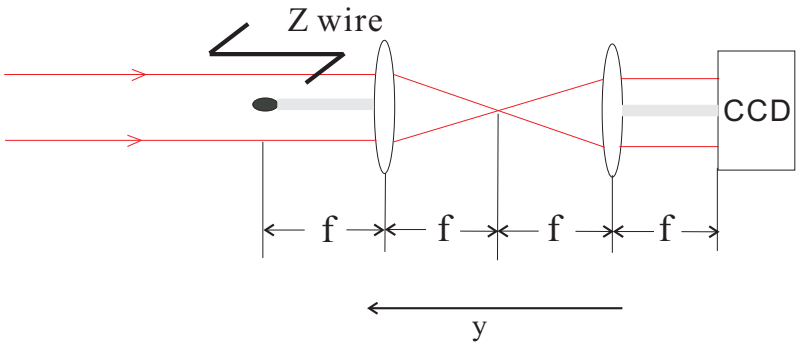

Figure 4.9: A 4-f absorption imaging setup

We image the atom cloud using an absorption imaging technique. The atoms are illuminated by an on-resonant probe beam. The photon scattering of the atoms leaves a shadow in the beam, which is recorded by a charge coupled device (CCD) camera as shown in Fig. 4.9. The optical depth (OD) is related to the intensity of the probe beam as in Eq. 4.7,

$$I = I_0 e^{-OD}\,, \tag{4.7}$$

where I is the probe beam intensity with the atoms and I_0 without the atoms. The

column density of atoms at each point is simply OD/σ, where σ is the scattering cross section.

In the experiment, in addition to I and I_0, a background image I_b is also needed. This background image, taken with the probe beam off and the camera shutter open, will be used to compensate for the camera dark current as well as any stray light not from the probe beam. With these three images, the optical depth OD at a certain pixel site (i, j) is given by

$$OD(i,j) = \ln(\frac{I_0(i,j) - I_b(i,j)}{I(i,j) - I_b(i,j)}\,. \tag{4.8}$$

The total atom number is then simply calculated by

$$N = \frac{1}{\sigma}\sum_{i,j} OD(i,j) S_{pixel}\,, \tag{4.9}$$

where S_{pixel} is the pixel area of the CCD camera. The scattering cross section σ can be expressed as

$$\sigma = \frac{BR}{2}\frac{3\lambda^2}{2\pi} \times (1 + 4\frac{\Delta^2}{\Gamma^2})^{-1}\,, \tag{4.10}$$

where BR is the branching ratio of the probe beam transition, λ is the probe beam wavelength, Δ is the probe beam detuning and Γ is the excited state decay rate. For on-resonant light, $\Delta = 0$ and the branching ratio for our probe beam transition, $|F = 2, m = -2\rangle \rightarrow |F' = 3, m = -3\rangle$, can be looked up in appendix A to be 15/15=1. Hence σ is computed to be $0.1452\mu m^2$ for our imaging setup.

As shown in Fig. 4.7, the image beam comes from a diode laser, which is frequency stabilized by the absorption spectroscopy method. Afterwards the beam frequency is up-shifted twice by an AOM before being coupled into a polarization maintaining fiber. We also use the AOM to switch the probe beam, which pulses for 40 μs in our experiment. The beam is collimated to have a FWHM of about 3 mm after the fiber

and an intensity of about $\frac{I_s}{5}$, where I_s is the saturation intensity 1.6 mW/cm^2. After passing through a $\lambda/4$ waveplate to become circularly polarized, the probe beam is directed to the atoms along the center bar of the "Z" wire (y-direction). On the other side of the chamber, we have a 4-f lens setup to project the beam onto the CCD camera. The 4-f lens setup also works for the fluorescence imaging technique. Our CCD camera is from COOKE Corporation, model PIXELFLY qe, which has a 6.7 μm$\times$6.7 μm pixel size. The camera has a ultra compact design, only about 1.5" $\times$ 1.5" $\times$ 2" in dimension. Two achromatic lenses (1" diameter, 4" focal length) are mounted inside a Thorlab lens tube with the camera attached at the end. The distances between two lenses and between the lens and the camera are variable. The whole imaging package is then attached to a translation stage that offers a fine control over the relative position between the atoms and the imaging setup. Fig. 4.10 shows absorption images taken by our imaging system including image I (left), image I_0 (middle) and the image after the data analysis (right).

Figure 4.10: The images taken by the CCD camera with (left) and without the atom cloud (middle). The right picture shows the atom cloud after the data analysis.

4.3.2 Optical Pumping

The atoms trapped by the MOT are equally distributed among the 5 different magnetic sublevels of the ground state, but only $|F = 2, m = 2\rangle$ atoms can be efficiently transferred into the Z-trap. To improve the transferring efficiency, an optical pumping beam is applied to the atoms before the Z-trap is turned on. The

optical pumping beam, circularly polarized, drives transitions as shown in Fig. 4.11. When atoms reach $|F = 2, m = 2\rangle$ sublevel, they will stay there since the $|F = 2, m = 2\rangle$ sublevel is decoupled from the pumping field. A repumper field, on resonance of $|F = 1\rangle \rightarrow |F' = 2\rangle$ transition, is present during the optical pumping.

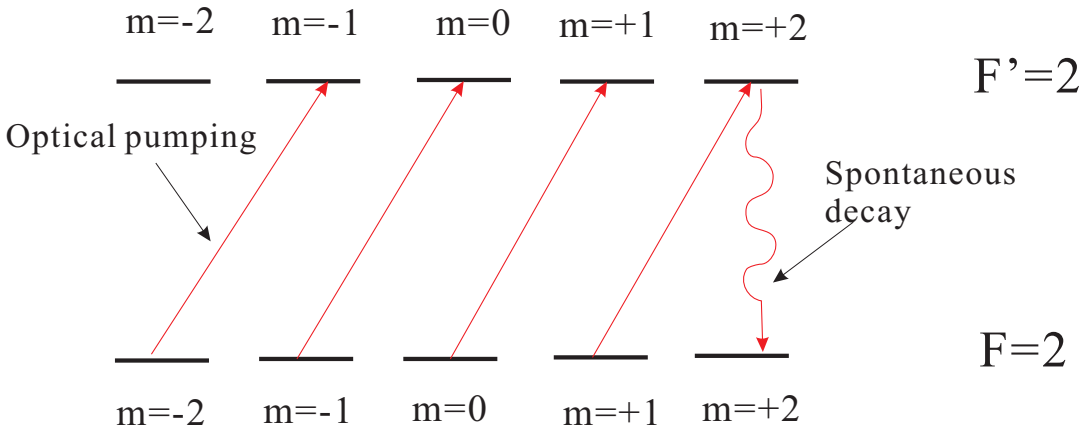

Figure 4.11: The transition diagram for the optical pumping.

The quantized axis of the Z-trap is along the direction of the center bar (y direction). Therefore during the optical pumping, a 3G magnetic field along y-direction is switched on to define the quantization axis. The optical pumping beam is also in the y-direction. As seen in Fig. 4.7, the pumping beam comes from the same laser as the imaging beam and has a very similar optical setup. However, the AOM down-shifts the frequency of the beam twice in the optical pumping case. The beam is then coupled into the same fiber as the imaging beam and shares the same optics and optical path afterwards. The optical pumping beam has an intensity of about $2I_s$ and is on for $100\mu s$.

4.3.3 Evaporative Cooling

After the atoms are transferred into the Z-trap, we start the forced RF evaporative cooling. The evaporative cooling works by preferentially removing most energetic atoms from the Z-trap and at the same time allowing the remaining atoms to reach

a lower temperature by elastic collisions. The removal of the higher energy atoms is done by bathing the Z-trap in a radio frequency magnetic field. This RF field couples atoms in adjacent magnetic sublevels $\Delta m = \pm 1$ with a resonance frequency ν_{rf} given by

$$\nu_{rf} = \frac{\mu_B \cdot B_{trap}}{2h}\,, \tag{4.11}$$

where B_{trap} is the magnetic field of the Z-trap at the location of an atom. At the beginning of the evaporation, ν_{rf} is set at a high value and the resonant B_{trap} for spin-flip is located on an ellipsoidal surface far away from the trap center. Given the fact that higher energy atoms tend to stray away from the center of the trap and penetrate this ellipsoidal surface, they are most likely to be coupled to $|m = 1, 0\rangle$ or even anti-trapped $|m = -1, -2\rangle$ states and permanently leave the trap. As the evaporation process goes on, we continuously ramp down ν_{rf}, forcing the ellipsoidal surface to shrink, and keep removing the higher energy atoms until the remaining atoms reach the BEC transition temperature. Fig. 4.12 shows the absorption images of the atoms inside the Z-trap after 10 s of forced RF evaporation starting from 10 MHz. As seen, the atom cloud shrinks as the stopping frequency decreases.

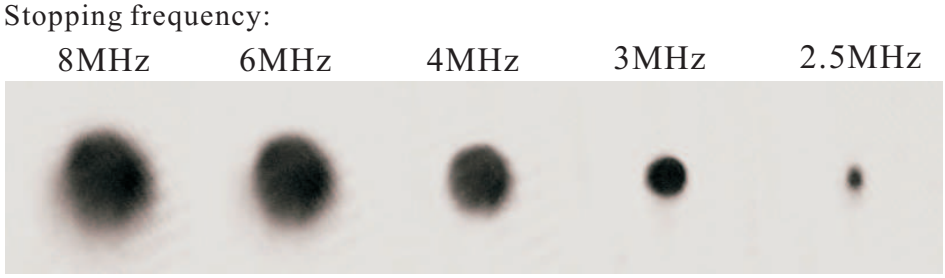

Figure 4.12: The in-trap images of the atoms after 10 s forced RF evaporation. The RF signal starts from 10 MHz and linearly decreases to 8 MHz, 6 MHz, 4 MHz, 3 MHz and 2.5 MHz respectively.

The RF signal is generated by an arbitrary function generator, Agilent 33220A. It can output two types of frequency sweep, a linear sweep and a logarithm sweep, upon an external trigger. Both sweeps work in our experiment to achieve a BEC,

which will be discussed later. The signal is then passed through a Mini-circuit RF switch before sent to a Mini-circuit 1W amplifier. A home-made 3-loop coil takes this amplified RF signal and delivers it to the atoms. The coil, about 2 inches in diameter, is made from normal 15 gauge magnetic wire and soldered directly to a BNC connector. A BNC cable is used to connect between the amplifier and the coil. Before we set up the coil, we make sure the coil itself has no obvious resonant frequencies within the evaporation frequency range, which is typically from 17 MHz $\rightarrow$ 500 kHz. The coil is placed right outside one of the large windows with the axis of the coil tilted 10^o relative to the center bar of the "Z" wire. This is not an ideal position for the coil since only the component of the RF field perpendicular to the local quantization axis can cause a spin-flip. However, considering the RF field will reflect multiple times in all directions inside the vacuum chamber, this should not pose a serious problem for us.

A more serious problem posed by this radiation RF field is that it interferes with both our diode laser systems and power supplies. In general we find it is helpful to ground the case of the laser driver through a thick wire and connect certain capacitors between the $\pm$ outputs of power supplies. The RF amplifier itself is also contained in an aluminum box. Although some interference is still present in our experiment, it does not affect the production of the BEC.

4.4 Experimental Measurement of the Z-Trap Frequency

It is important to know the Z-trap frequencies when we start the evaporative cooling. Although as pointed out in section, we can calculate trap frequencies from simulations, we want experimental measurements to verify the simulation results. With the absorption image setup and the forced RF evaporation working, it is pos-

sible to measure the Z-trap frequencies in x- and z-directions experimentally. The

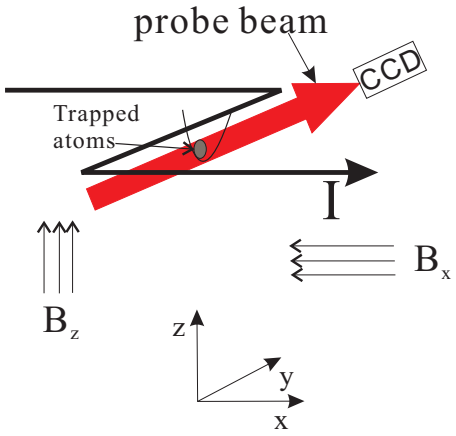

Figure 4.13: Relative position between the Z-wire and the absorption image beam.

relative position between the Z-wire and the absorption image beam is shown in Fig. 4.13. Based on the observation perspective, oscillations in x- and z-directions can be seen on absorption images. We apply a sudden small change to the z (y) bias magnetic field B_z (B_y), which causes a small displacement of the Z-trap from its initial location in the x- (z-) direction. The atom cloud inside the Z-trap cannot follow the sudden shift and will undergo subsequent oscillations. Since the displacement is normally in the order of 100 μm, to observe this oscillation we need an atom cloud with a size much less than the oscillation amplitude, which requires a functional evaporative cooling. After the displacement, we take absorption images at different times and stack them as shown in Fig. 4.14. The time difference between neighboring images is 2 ms. From Fig. 4.14, the oscillation frequency in x-direction is $\sim$56 Hz. The measurement of the z-directional oscillation frequency yields a similar result.

4.5 Experimental Procedure towards BEC

The procedure of producing the BEC can be divided into five stages: collection, compression, transfer, evaporation and detection.

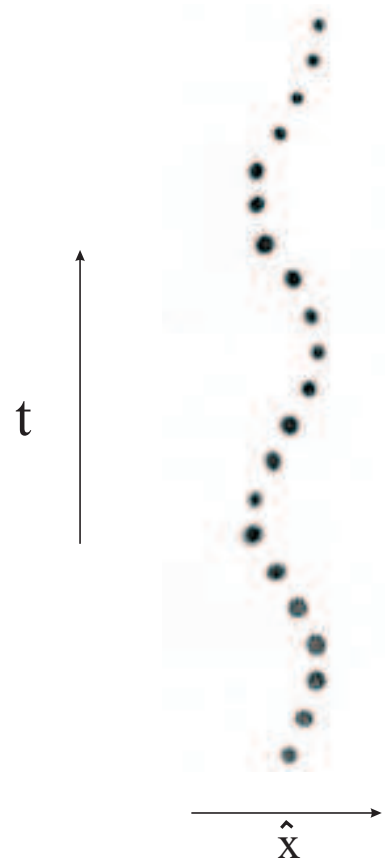

Figure 4.14: Oscillation of the cold atom cloud inside the Z-trap. The time interval between adjacent images is 2 ms.

The first stage involves collecting as many as possible atoms using the double-MOT setup discussed in section 4.2.2. Both the pyramidal MOT and the intermediate MOT are continually on for 16 s, during which about 10^9 atoms are loaded into the intermediate MOT located 3 mm below the mirror. After the collection stage, we shut the pyramidal MOT beam off and perform the MOT compression in the secondary chamber. This is done by turning off the external MOT coils and switching the U-trap on simultaneously, while keeping the MOT beams on. The U-trap has a current of 45 A and a x-bias field of 20 G. Although we use step functions to switch magnetic fields, the real transfer from the intermediate MOT to the U-MOT is adiabatic due to the inductance of the external MOT coils. It takes about 50 ms

for atoms to be reloaded into the U-MOT. This process moves the atom cloud up by 1.5 mm and compresses its size to about 2 mm in diameter. No significant atom loss is observed during the procedure. To further compress the U-MOT, the detuning of the MOT beams is increased from 2 Γ to 4 Γ for an additional 20 ms.

Now we have a large number of atoms in a high density region. Before we transfer the atoms into the Z-trap, we need to further cool atoms down to about 50 μK to ensure a good transfer efficiency. A 3 ms molasses cooling stage is therefore applied. We switch off the U-MOT magnetic field and use the MOT beams as a 3D corkscrew optical molasses. Since it takes about 500 μs to turn off magnetic fields, it is necessary for the MOT beams to be off during this period. Otherwise, the atoms would pick up too much momentum during the sudden switch of magnetic fields. When the MOT beams are turned back on, their detuning is increased to 7 Γ and the total power drops to 30 mW. Since the optical molasses is very sensitive to any stray magnetic field, we also use it to minimize the stray field in the vicinity of the atom cloud by adjusting three pairs of external compensation coils. When the stray field is less than 100 mG, we see an isotropic expansion of the atom cloud inside the optical molasses. After the 3 ms molasses cooling, the y bias magnetic field for the Z-trap is turned on to define the quantization axis. We then apply a 100 μs optical pumping pulse 300 μs later. Up to this point, the repumper beam is always on. The final step of the transfer stage is to turn on the Z-trap and use the mechanical shutters to block all beams. To optimize the transfer efficiency, the absorption image of the atoms inside the Z-trap is taken right after the transfer. We also maximize the atom number by adjusting the detuning and intensity of both molasses beams and the optical pumping beam as well as the Z-trap location. The final Z-trap has a current of 55 A, a x-bias field of 17 G and a y-bias field of 7 G, which corresponds

to (54 Hz, 15 Hz, 54 Hz) trap frequencies in (x-, y-, z-) directions, respectively.

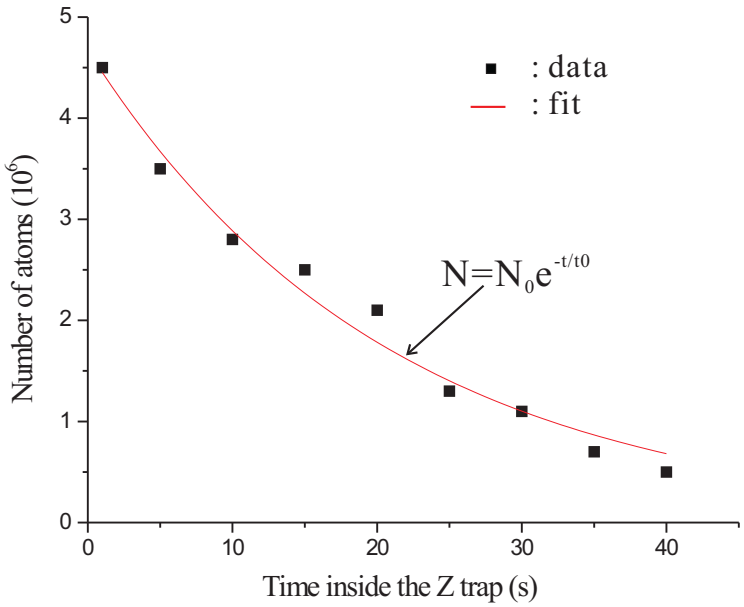

Figure 4.15: The number of atoms inside the Z-trap as a function of time. An exponential decay fitting shows the lifetime t_0 of 21 s.

After the optimization, about 10^7 atoms are loaded into the Z-trap. The next step is to evaporatively cool the atoms to the BEC transition temperature. However, before doing the evaporative cooling, we want to measure the lifetime of the atoms inside the Z-trap, which not only tells us how good the vacuum is or whether there is any stray light problems in the experiment, but also roughly determines the evaporation time. Fig. 4.15 shows the number of atoms inside the Z-trap as a function of time t. We fit the data with an exponential decay function and get the lifetime, $t_0 = 21s$. This data is taken one month after the bake-out of our vacuum chamber and with a black curtain surrounding the chamber to block any stray light. We currently expect a longer lifetime since the vacuum should be improved. During the evaporative cooling, on one hand we want time for the atoms to rethermalize, but on the other we do not want significant atom loss due to background collisions.

Thus, we first set the evaporation time to be 12 s (later on we found 16 s evaporation was optimal.). After the evaporation time is set, we try to determine the starting frequency, which is done by looking at the in-trap image of the atom cloud after a two-second evaporation with a constant frequency. We want the starting frequency to be such that the RF signal just evaporates the edge of the atom cloud. In our case, we measure the starting frequency to be around 16 MHz. With these two predetermined parameters and a RF power of 1 Watt, we first try an evaporative cooling with a linear frequency sweep, starting at 16 MHz and with different stopping frequencies. At the same time, the x-bias magnetic field is ramped up linearly from 20 G to 55 G, which results in a final Z-trap frequency of (500 Hz, 60 Hz, 500 Hz). The Z-current drops from 55 A to 53.5 A during the 12 s evaporation due to the heating of the Z-wire.

After the evaporative cooling, we turn off all magnetic fields and let the remaining atoms freefall for 12 ms before taking an absorption image. However, at the beginning when all experimental parameters are not optimized, it is hard to observe anything from the absorption image. Because when the stopping frequency is low, there is hardly any atoms left; but when the stopping frequency is high, the atom cloud expands too much during the 12 ms TOF. We therefore decide to decompress the Z-trap before the TOF since the decompression lowers the temperature of atoms and hence makes the detection of atoms much easier after the TOF. The decompression is done by linearly ramping down the x-bias field to 40 G in 100 ms. With the decompression, we can finally observe the atom cloud after the TOF. Unlike the in-trap image, the TOF image not only provides us with information about the density and temperature of the atom cloud, more importantly, also contains a distinctive signature of the BEC transition–an atom cloud with two density distributions due to

the fact that the BEC expands much more slowly than the thermal cloud. Once we observed the atom cloud after the 12 ms TOF, we lowered the stopping frequency of the evaporative cooling until the atom cloud was barely visible. Then we optimized the visibility by adjusting experimental parameters. If the BEC transition is not reached, we lowered the final frequency and repeated the optimization again. Finally we observed a clear BEC transition at a stopping frequency of 185 kHz as shown in Fig. 4.16.

Our best condition for a linear RF frequency sweep are: 15 s loading of the intermediate MOT, 16 s evaporation from 18 MHz to 800 kHz with a RF power of 1 W, although we never try more than 1 W RF power due to the limitation of the instrument. With these conditions, we can achieve a BEC of more than 100,000 atoms. We also find that multiple stages of a frequency sweep does not help in our case.

To reduce the BEC production time, we explored other approaches to reach the BEC transition. One successful way is to use a logarithm RF frequency sweep. In this method, after the atoms are loaded into the Z-trap, we compress the Z-trap to (500 Hz, 60 Hz, 500 Hz) trapping frequencies in 150 ms before the evaporative cooling. In this case, the starting collision rate of the atoms is much higher and since the atom cloud is very close to the mirror surface, surface cooling also plays a role. The RF frequency is then swept from 16 MHz to 800 kHz in a logarithm form in 5 s. With this RF sweep, we can achieve a BEC of about 80,000 atoms. The initial collection stage can also be greatly reduced. We have successfully achieved a BEC of 50,000 atoms with only 6 s intermediate MOT loading. For experiments discussed in the next chapter, the BECs are all produced with 10 s loading time and 5 s of evaporation.

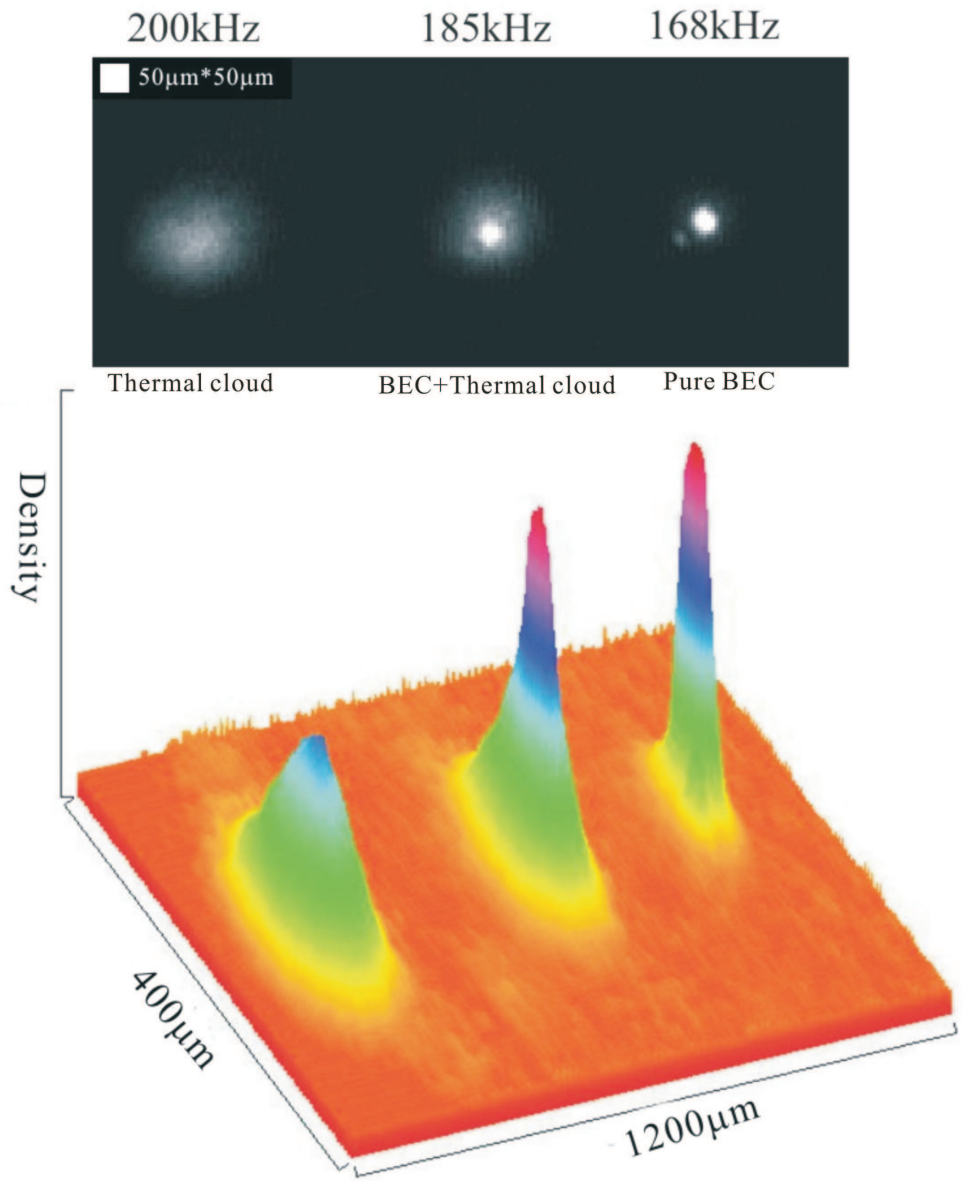

Figure 4.16: Top panel: absorption images of the atom cloud after 12 ms TOF for different final evaporation frequencies. The center image shows a clear BEC transition – there are two density distributions of the atom cloud. The right image is a pure BEC of about 30,000 atoms. The bottom panel is the 3-D plot of the top panel with the height representing the density.

4.6 Conclusion

In this chapter, I have described our experimental setup to achieve a Bose-Einstein condensate of ^{87}Rb atoms. A new vacuum chamber, with three main compartments, is constructed for the BEC experiment. The ^{87}Rb atoms are first collected from the background vapor inside the primary chamber and then transported to the secondary chamber, where the vacuum pressure is three orders of magnitude lower. This pressure difference is maintained by a differential pumping stage. Inside the secondary chamber, the atoms are recaptured, compressed, further cooled, optically pumped and eventually tranfered into an Ioffe-Pritchard type magnetic trap formed by a Z-shaped current. Finally the BEC is achieved inside the Z-trap after the forced RF evaporative cooling.

CHAPTER V

Bose-Einstein Condensate in Optical Lattices

The realization of Bose-Einstein condensation in dilute alkali gases has opened exciting new frontiers in physics research. Subsequent investigations have involved fundamental properties of BECs, such as vibrational excitations of BECs [50, 51] and the role of the scattering length and its modification by Feshbach resonances [52, 53]. Being macroscopic quantum ensembles, BECs also provide an unprecedented platform to study quantum phenomena, such as vortices in BECs [54] and BEC interference [55], which ultimately leads to a wide range of research involving atom interferometers [57–60]. Moreover, the combination of BECs with optical lattices can be used to simulate traditional condensed matter systems. Compared with electrons in solid state crystals, BECs in optical lattices not only offer excellent control over experimental parameters, but also are easy to probe in laboratories. In addition, since optical lattices are perfect periodic potentials, there are no complicated impurity effects present in the BEC-optical lattice experiment. As a result, many condensed matter phenomena have been observed in this system, including Bragg scattering [71], Bloch oscillation [72], the superfluid to Mott-insulator transition [12, 73, 74] and tunneling of BECs between [75] and out of lattice wells [76].

In this chapter, we study the behavior of BECs inside a far-detuned 1-D op-

tical lattice. The starting point of lattice experiments is a BEC of about 60,000 atoms inside the Z-trap. The potential depths of optical lattices are calibrated using Kapitza-Dirac diffraction. The interference effects of both thermal clouds and BECs are discussed. Quantum phenomena, such as Bloch oscillations and superfluid to Mott-insulator transitions, are investigated.

5.1 The 1-D Optical Lattice Setup

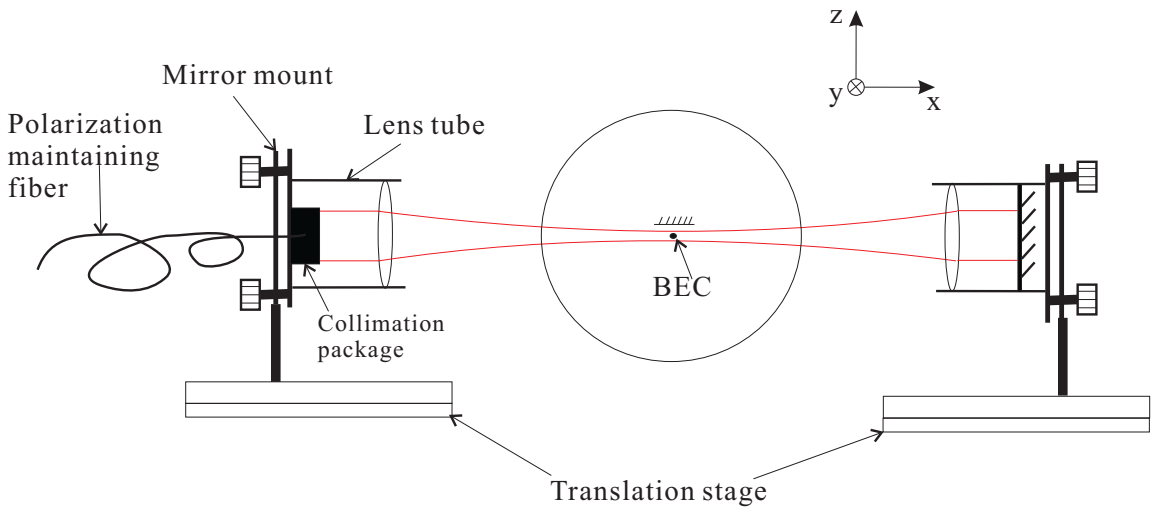

Figure 5.1: The 1-D lattice beam setup

The lattice beam comes from a Tapered Amplifier System (TAS) built by Sacher Lasertechnik. The master laser of the TAS is a Cheetah distributed feedback (DFB) diode laser, with a wavelength fixed at 852 nm. The maximum power output of the TAS is 900 mW. Since the frequency of the lattice laser is far away from any atomic transitions, frequency-stabilization is not needed. Out of the TAS, the beam is passed through an acousto-optic modulator (AOM) and then coupled into a polarization maintaining optical fiber. After the fiber, the lattice beam is first collimated to a FWHM of 0.75 mm and then focused into the vacuum chamber by an achromatic lens with 30 cm focal length. On the other side of the chamber, the beam is collimated

again by another achromatic lens with the same focal length and then retro-reflected by a mirror. The lattice beam is delivered to the atoms in the x-direction. As shown in Fig. 5.1, the fiber output, the collimation package and the achromatic lens are mounted together inside a Thorlab 1" lens tube, which is then attached to a mirror mount. The whole package is set up on top of a translation stage so that fine-adjustment of the focus location of the beam is possible. A retro-reflection unit with a similar design is set up on the other side of the chamber. We arrange the optics such that the two counter-propagating beams overlap and the BEC is located at the focus of the lattice beams. The size of the focal spot is about 100 μm. The relative position between the lattice beam and the rest of the experimental setup is shown in Fig. 5.2. This optical lattice configuration is used in all experiments discussed in the following sections.

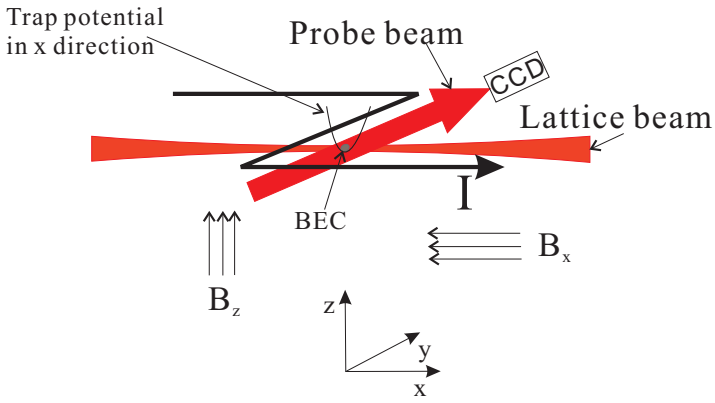

Figure 5.2: The relative position between the lattice beam and the Z-trap.

The alignment of the lattice beam with respect to the BEC is a non-trivial procedure. Fortunately in our experiment the BEC is created underneath a mirror, which works as a reference for our alignment. First, the distance between the mirror and the BEC can be measured from the absorption image. Then we align the lattice beam to be about the same distance away from the mirror. Since the lattice beam has a Rayleigh range of about 9 mm and the BEC should be located at the center of

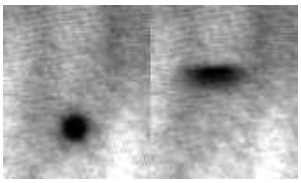

Figure 5.3: Absorption images of the BEC without lattice beams (left) and with a continuous lattice beam (right). Both images are taken after 10 ms TOF.

the vacuum chamber, the alignment in x direction can be roughly done by placing the lens 30 cm away from the center of the chamber. Then only walking the beam in the y-direction is necessary.

We first set the lattice beam to be continuous and look for the effect of the input lattice beam from the absorption image after 10 ms TOF of the BEC. When the lattice beam intensity is high enough, we expect it work as an optical dipole trap. The BEC will be distorted and its position after 10 ms TOF will be shifted upwards since the optical dipole trap holds the BEC against the gravity. These two effects are seen as shown in Fig. 5.3 when the single beam power is over 120 mW. Once the input beam hits the BEC, the alignment of the returning beam is not as hard.

5.2 Kapitza-Dirac Diffraction

One of the most important parameters of an optical lattice is its potential depth, which is proportional to the intensity of the lattice beam. However, at the location of the atoms, it is hard to know the local intensity accurately especially when the beam is focused down to such a tiny spot. A small misalignment of the lattice beam relative to the atoms can cause a large intensity difference. Hence, we depend on an experimental method to determine the local potential depth of the lattice.

Consider what happens to a BEC exposed to an optical lattice. We assume that

the BEC wavefunction at time t=0 is given by

$$\psi(t=0) = 1, \tag{5.1}$$

and the BEC experiences a lattice potential

$$V(z) = -\frac{V_0}{2}\cos^2(k_L z), \tag{5.2}$$

where $k_L = \frac{2\pi}{\lambda}$ with λ being the lattice beam wavelength. If the lattice duration τ is sufficiently short, the lattice potential can be treated as a phase modulation, given by $e^{iV(z)\tau/\hbar}$, to the initial BEC wavefunction [77]. Using the Jacobi-Anger relation, the propagated wavefunction can be expanded as

$$\psi(z, t>0) = \exp\left(i\frac{V_0\tau\cos(2k_L z)}{2\hbar}\right) \tag{5.3}$$

$$= \sum_{n=-\infty}^{\infty}(i)^n J_n\left(\frac{V_0\tau}{2\hbar}\right)e^{i2nk_L z}, \tag{5.4}$$

where J_n are Bessel functions of the first kind. Each term in the expanded wavefunction represents one diffraction order of the BEC. The nth order has a momentum of $n2\hbar k_L$ and a population of $[J_n(\frac{V_0\tau}{2\hbar})]^2$. This phenomenon is similar to the diffraction of electrons by a standing wave, predicted by Kapitza and Dirac in 1933, with the role of electrons played by the BEC. Note that the above argument also applies to thermal atoms. Therefore the Kapitza-Dirac diffraction effect can also be observed with thermal atoms as long as their temperature is low enough to allow different diffraction orders to separate.

Since the population of the nth diffraction order is directly related to the local potential depth V_0 of the optical lattice, we can measure V_0 experimentally by this diffraction method. In the experiment, we apply optical lattices with different durations to the BEC and take absorption images after 15 ms time-of-flight to allow different diffraction orders to separate. The TOF images are shown in Fig. 5.4. The

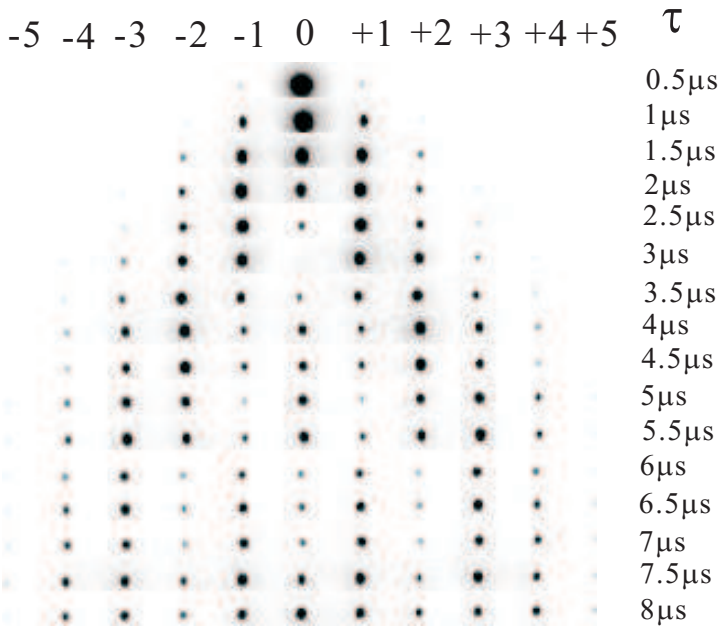

Figure 5.4: The 15ms TOF images of BECs after exposed to an optical lattice with different durations indicated on the right side.

atom numbers of 0th, 1st, and 2nd orders are calculated and plotted as a function of τ in Fig. 5.5. To compensate for the fluctuation of the initial condensate atom number, the total population of each shot is normalized to 1. In order to calculate V_0, we fit $J_0(c\tau)^2$ to the first 10 data points in Fig. 5.5 (a) and achieve a fitting parameter $c = 0.804\mu s^{-1}$ for the maximum lattice beam power of 180 mW. Based on Eq. 5.4, $V_0 = 2\hbar c = h \times 256$kHz. To check the accuracy of the fitting parameter, we plot $J_1(c\tau)^2$ and $J_2(c\tau)^2$ in Fig. 5.5 (b) and (c) with the same parameter $c = 0.804\mu s^{-1}$. As seen, up to 5 μs, all three experimental data stay close to the predicted values. However, after 6 μs, they start to deviate from the fitting curve, which means a breakdown of the "short" pulse assumption. The effect of the optical lattice can no longer be treated as a phase modulation due to the breathing motion of the BEC inside the optical lattice [77].

Now that we have established an experimental method to measure the local potential depth for the maximum lattice beam power, the potential depths can be

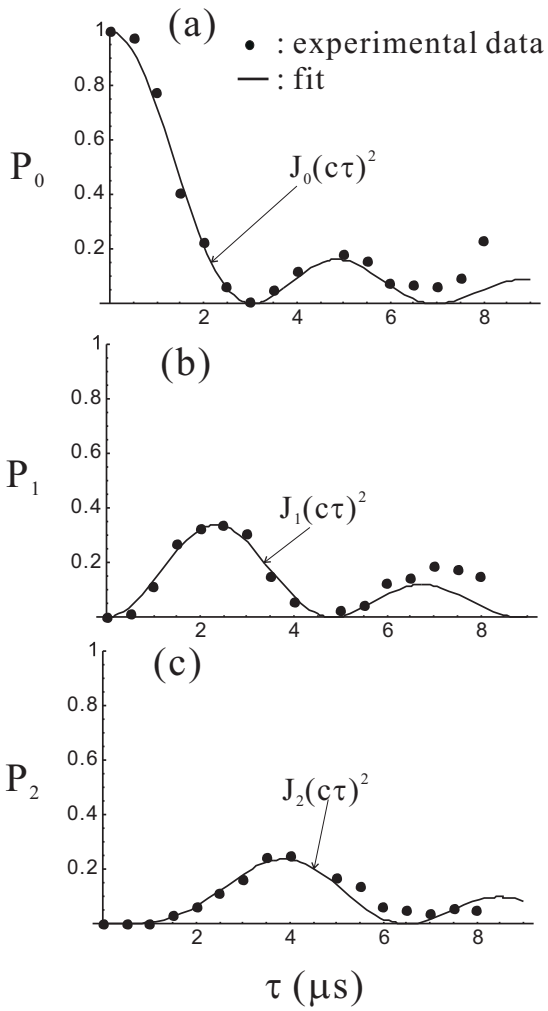

Figure 5.5: The normalized population of atoms in 0th (a), 1st (b), 2nd (c) diffraction orders as a function of the optical lattice duration. The fitting is only for the first 10 data points of (a). After obtaining the fitting parameter c, the theoretical results are plotted in (b) and (c) with the same c value.

calculated for any power based on the linear relationship between the power and the potential depth. In the following experiments, all of the quoted lattice depths are calibrated by this method. The Kapitza-Dirac diffraction phenomenon can also be used to fine adjust positions of the lattice beams since it is very sensitive to the local intensity change, especially for a lattice duration of about 2 μs .

5.3 Interference of Thermal Atoms Using the Kapitza-Dirac Diffraction

The interference of atom clouds is often regarded as the signature of BECs since the long-range coherence is believed to appear only when the atoms are condensed into the same quantum state. However, we know that the interference of two light beams was observed long before the laser was invented. The most famous example is Young's double-slit experiment, where two interfering beams from the same source, the first slit, act as two copies of the source light. As discussed in the previous sec-

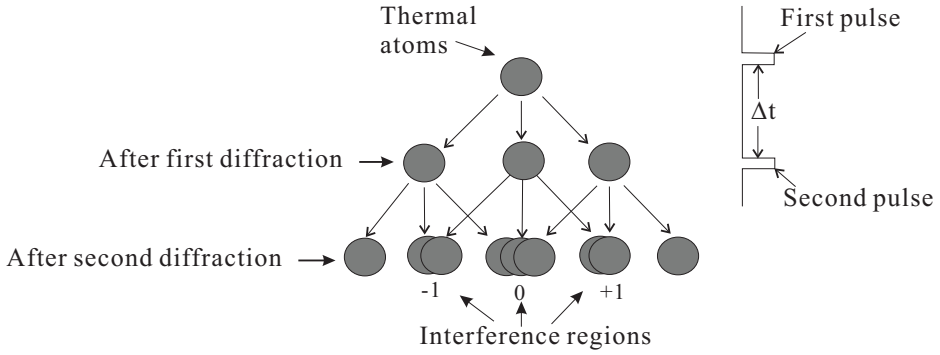

Figure 5.6: Schematic drawing of Kapitza-Dirac diffraction orders produced by two pulses.

tion, a short and intense lattice pulse projects atoms into different velocity groups through Kapitza-Dirac diffraction. When another pulse is applied, it remixes different diffraction orders as shown in Fig. 5.6. We expect to see interference fringes at regions where atom clouds overlap. Since this interfering behavior originates from the overlapping of two copies of a single-atom wavefunction, the interference pattern can show up regardless of whether the atoms are in condensate or thermal states.

The fringe visibility of the whole thermal atom cloud, however, depends on the temperature of the atoms since it is an incoherent sum over all atoms.

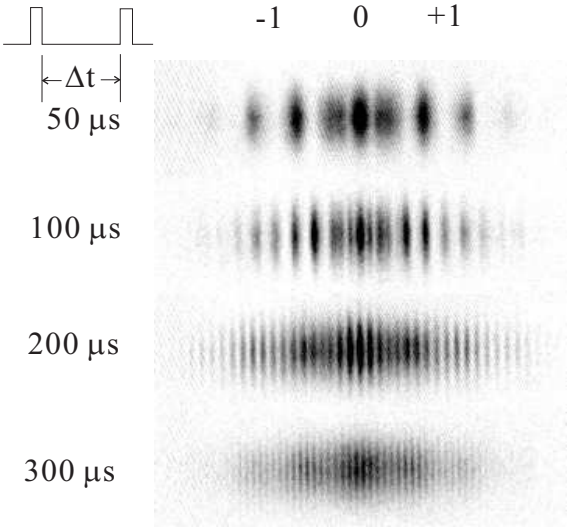

Figure 5.7: The interference images after 20 ms TOF for Δt =50 μs, 100 μs, 200 μs and 300 μs.

In the experiment, the cold thermal atom cloud is created by choosing the final RF-evaporation frequency to be 40 kHz above the BEC transition. Each lattice pulse has a potential depth $V_0 = h \times 256$ kHz and a duration of 2 μs. After the second pulse is applied, the Z-trap is switched off to allow the atom cloud to free fall for 20 ms before an absorption image is taken. The interference images for different pulse separations, Δt, are shown in Fig. 5.7. As seen, the interference pattern around the 0th diffraction order is different from other regions because it involves three atom clouds as indicated in Fig. 5.6. We also notice that, with an increasing Δt, the period of the interference fringe decreases. According to Ref. [78], the fringe period λ_f for two-cloud interference is given by

$$\lambda_f = \frac{C}{\Delta t}, C = \frac{h t_{\mathrm{TOF}}}{M v_{2\mathrm{rec}}}, \tag{5.5}$$

where t_{TOF} is the time of flight, M is the mass of the atom and $v_{2\mathrm{rec}}$ is the two-photon recoil velocity (the pulse duration is not considered in this equation since it is much

shorter than Δt). From Fig. 5.7, λ_f can be measured as a function of Δt. To be consistent with the Eq. 5.5, where the interference only involves two thermal clouds, we only consider the first diffraction-order region when measuring λ_f. The resulting λ_f vs. $\frac{1}{\Delta t}$ is plotted in Fig. 5.8. It clearly shows a linear relation between λ_f and $\frac{1}{\Delta t}$, which is expected from Eq. 5.5. Fitting the experimental data with a linear function $y = Cx$ gives a slope $C = 9.0 \pm 0.1$ μm·ms. Theoretically C is calculated to be 8.6 μm·ms.

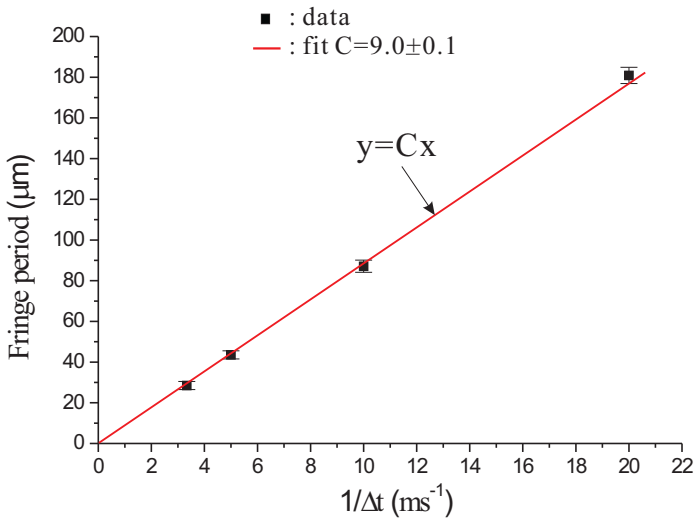

Figure 5.8: The measured λ_f as a function of $\frac{1}{\Delta t}$. A linear fit yields a slope $C = 9.0 \pm 0.1$ μm·ms.

To qualitatively show the dependence of the overall fringe visibility on the thermal temperature, we vary the final evaporation frequency ν_{fRF} and keep Δt =200μs and all other parameters the same as in the previous experiment. The temperature of the atom cloud is determined by ν_{fRF}, where increasing ν_{fRF} leads to higher temperatures. As seen in Fig. 5.9, the visibility drops with an increasing temperature. The quantitative dependence of the fringe visibility on the thermal temperature can be found in Ref. [78].

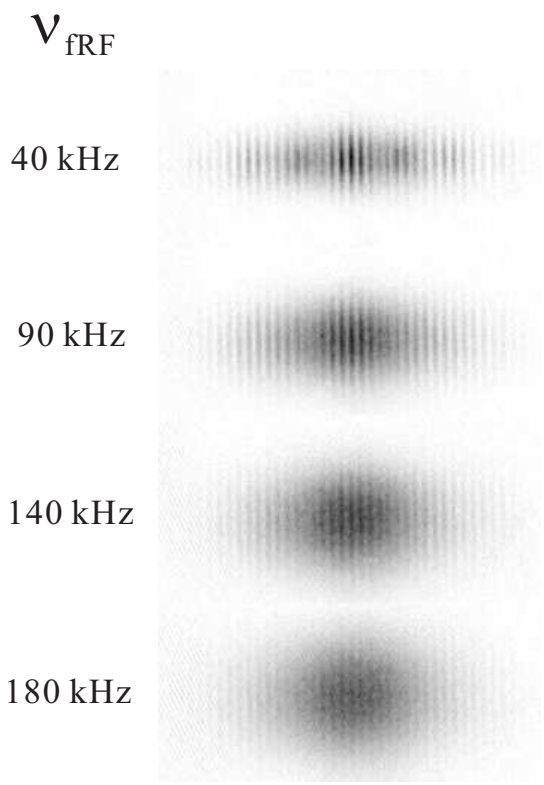

Figure 5.9: Interference images for different temperatures of the atom cloud.

5.4 Atom Interferometer Using the Kapitza-Dirac Diffraction

Due to their long spatial coherence, BECs are promising for applications such as atom interferometer. It has long been demonstrated that overlapping of two BEC clouds produces interference fringes, analogous to the interference of two coherent light beams. To make an atom interferometer, the only other requirement is that the two BECs undergo different paths before overlapping.

An atom interferometer can be realized using Kapitza-Dirac diffraction and a magnetic trap, as schematically shown in Fig. 5.10. The first lattice pulse splits the BEC into different momentum components. As a result, the non-zero momentum components undergo oscillations inside the magnetic trap. After half an oscillation period, all BEC components meet again at the center of the trap, and interference fringes should be produced. However, since the fringe period is inversely propor-

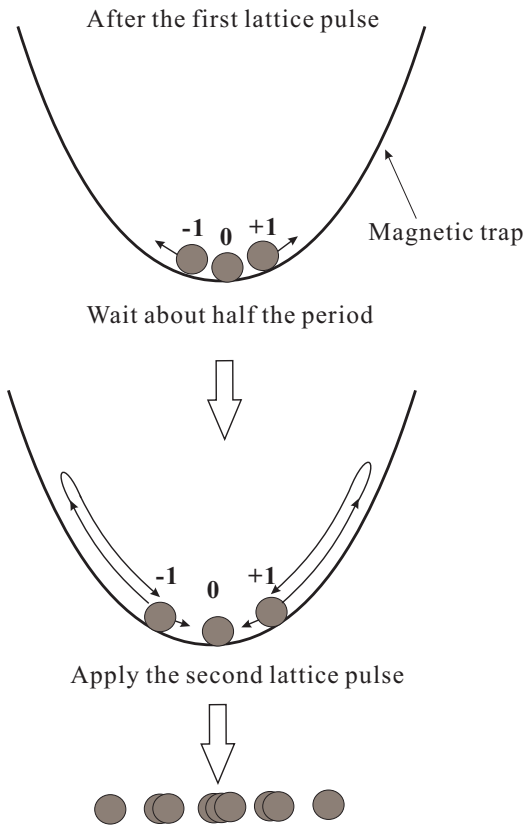

Figure 5.10: Atom-interferometer scheme using Kapitza-Dirac diffraction and a magnetic trap.

tional to the velocity difference between two BEC components, it is too small to be observable in the experiment. Therefore, another diffraction pulse is applied to the BECs, which remix different momentum components as in the previous experiment. Note that thermal clouds are not good for this interferometry scheme, even though their interference is demonstrated in the previous section. Because different thermal states develop different phases during the oscillation, the interference fringes are completely washed out. For BECs, this atom interferometer, in principle, works for multi oscillations.

In the experiment, the lattice pulses have a 2 μs duration and the oscillation period, T, of the magnetic trap is about 17 ms. After the second lattice pulse, we turn off the magnetic trap and allow the BECs to free fall for 25 ms before taking an

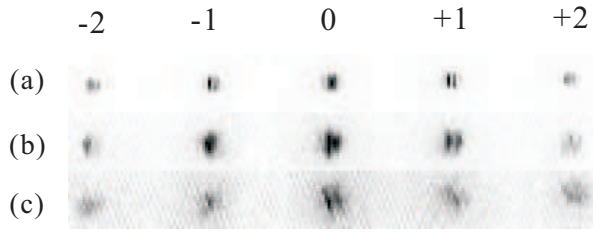

Figure 5.11: Interference fringes produced by the atom interferometer for pulse separations of (a) 1 ms, (b) 7.8 ms and (c) 16.5 ms.

absorption image. Figure 5.11 shows experimental results for the pulse separation, Δt, of (a) 1 ms, (b) 7.8 ms ($\sim T/2$) and (c) 16.5 ms ($\sim T$). The interference fringes are clearly present in all three cases. In Fig. 5.11 (a), the situation is similar to what is discussed in the previous section except that now we use a BEC instead of a thermal cloud. Figure 5.11 (b) and (c) demonstrate the atom interferometer described in Fig. 5.10.

The interference fringes in Fig. 5.11 (c) are obviously tilted. This may be due to the fact that the BEC is contained in a 3-D magnetic trap and the trap frequencies in the x- and z-directions are slightly different. If the projection of the lattice beam in the z-direction is non-zero, BECs also oscillate in the z-direction after the first lattice pulse. Since oscillations in the x- and z- directions do not exactly synchronize, interfering momentum components will have non-zero relative velocity perpendicular to the lattice direction, causing tilting fringes. Based on the simulations, the x- and z-oscillation frequencies have $\sim 3\%$ difference, which means that the longer the separation between two lattice pulses (within our experimental time scale), the larger the relative velocity becomes perpendicular to the lattice direction. That is why the tilting is most prominent in Fig. 5.11 (c), where the pulse separation is the largest.

Close to half an oscillation period, the relative velocity between interfering BEC components becomes small, which leads to a larger spatial period of the interference fringes. In Fig. 5.12, Δt is 7.2 ms, 7.8 ms and 8.4 ms for (a), (b) and (c), respectively.

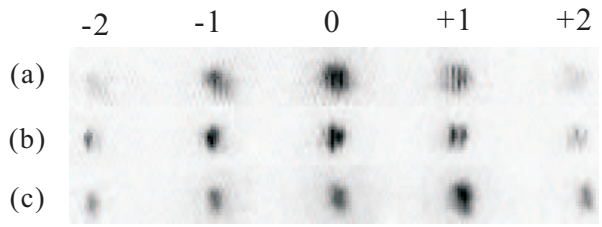

Figure 5.12: Interference fringes produced by the atom interferometer for pulse separations of (a) 7.2 ms, (b) 7.8 ms and (c) 8.4 ms.

The spatial period of the interference fringes increases as Δt approaches $T/2$. When this spatial period becomes larger than the size of the BEC, instead of fringes, the interference shows up as a population difference between $\pm$ momentum components, as seen in Fig. 5.12 (c).

5.5 Bloch Oscillation of BECs

One of the most striking predications made by early quantum theory is the Bloch oscillation of electrons in a solid state crystal. When a homogeneous static electric field is applied, electrons undergo oscillatory instead of accelerated motion inside the crystal (see [79] for detailed discussion). This Bloch oscillation phenomenon, however, is almost impossible to observe experimentally in solid state systems becauset the scattering time of electrons by defects in the crystal is much shorter than the oscillation period. Cold atoms in an optical lattice mimic electrons in a crystal, but due to the extremely low temperature of atoms and the perfect periodic potential created by the optical lattice, the coherence time of atoms is much longer. This makes the experimental observation of the Bloch oscillation possible. So far, Bloch oscillations have been observed for cold atoms [80] and BECs [81] in the rest frame of accelerated optical lattices.

In this section, we present the Bloch oscillation of a BEC in the laboratory frame. Unlike previous Bloch experiments where the Bloch oscillation is induced by accel-

erating the optical lattice, in our experiment we initiate the oscillation by a small displacement of the BEC from the trap center, as shown in Fig. 5.13 (a). Following the displacement, the BEC is accelerated towards the trap center. Since it also experiences an optical lattice potential, according to the Bloch oscillation theory, the BEC can not be accelerated beyond a certain velocity. This velocity limit corresponds to one recoil velocity, where Bragg reflection of the BEC by the optical lattice occurs. At the end of the Bragg reflection, the BEC velocity is reversed, but maintains its magnitude. The BEC then comes back to its initial location at the end of one oscillation. The system shown in Fig. 5.13 (a) can also be viewed as an atom cavity with the optical lattice acting as a mirror to reflect atoms.

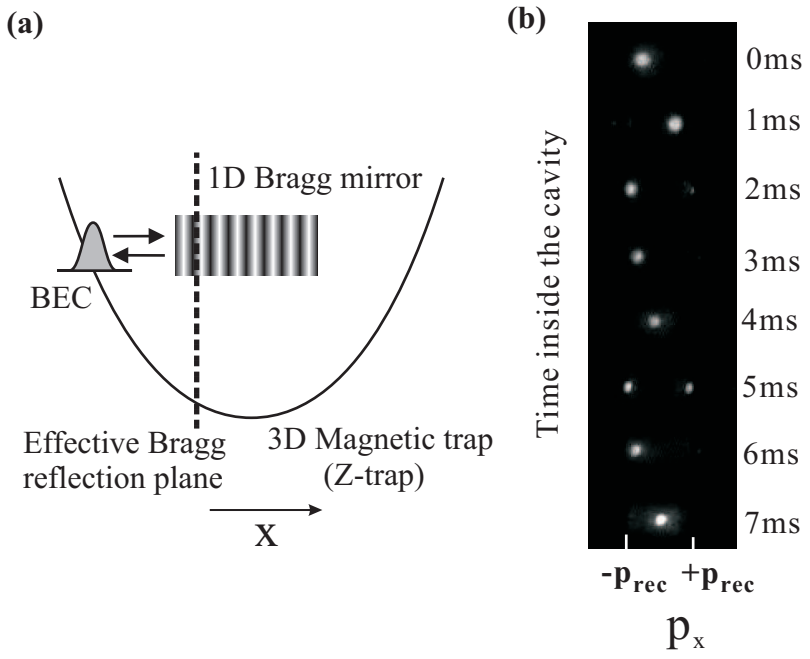

Figure 5.13: (a) A schematic drawing of the setup to realize Bloch oscillations of the BEC inside the combination of a magnetic trap and an optical lattice. (b) Momentum of the BEC inside the cavity.

In the experiment, the BEC is prepared in a trap with frequencies of 45 Hz, 15 Hz and 45 Hz in the x-, y- and z-directions, respectively. An optical lattice with a full potential depth of about one recoil energy is applied to the BEC with a turn-on time

of about 1 μs. Three milliseconds after the lattice is applied, the vertical bias field (z-direction), is ramped up by 100 mG in 2 μs, corresponding to a 44 μm translation of the equilibrium position of the Z-trap in the x-direction, parallel to the optical lattice. The translation occurs quickly enough that the BEC does not have time to move. In this way, we experimentally create initial conditions equivalent to those in Fig. 5.13 (a).

The momentum of the BEC is measured using a time-of-flight (TOF) method. In the TOF method, the BEC is released after a certain evolution time by suddenly switching off both the Z-trap and the optical lattice. We then allow the BEC to expand freely for 15 ms before taking an absorption image, at which point the momentum of the BEC at the time of release can be determined by its measured position in the x-direction.

After the decompression, the BEC often exhibits a small, random momentum that we attribute to magnetic field fluctuations. The random momentum leads to a phase shift in the Bloch oscillation, which causes a time jitter of up to ± 0.5 ms in the observed Bragg reflections. To minimize the effect of this jitter, we take five separate TOF images for each time step, compare the BEC momenta, and choose the median image for presentation.

Figure 5.13 (b) shows TOF images of the BEC after different evolution times. The horizontal axis of the image represents the momentum in the x-direction. Generally, as the evolution time increases, the momentum of the BEC increases in an approximately linear fashion due to the magnetic force. The momentum reversals at 2 ms and 5 ms are due to Bragg reflection; these reflections occur at times when the BEC reaches a momentum of $+p_{\mathrm{rec}}$. During the Bragg reflection process, both momentum components, $+p_{\mathrm{rec}}$ and $-p_{\mathrm{rec}}$, are present in the BEC, as seen in Fig. 5.13 (b). From

the point of view of energy band theory, the BEC moves along the lowest energy band in the first Brillouin zone, indicated in Fig. 5.14. Assuming no excitation to higher energy bands, whenever the BEC leaves one edge of the first Brillouin zone, it comes back from the other edge. This is confirmed by our experimental data in Fig. 5.13 (b) since $+p_{\mathrm{rec}}$ and $-p_{\mathrm{rec}}$ correspond to the two edges of the first Brillouin zone.

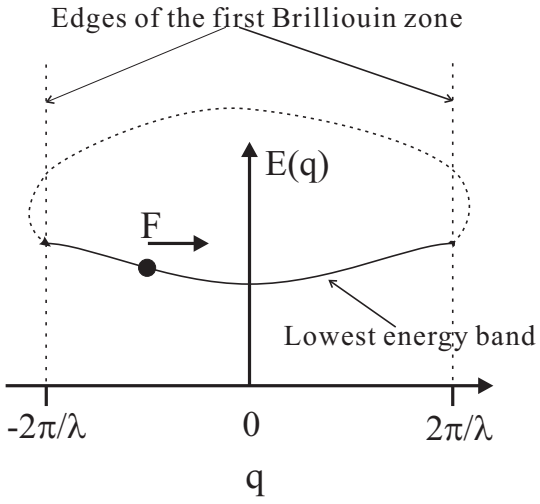

Figure 5.14: Schematic drawing of the BEC moving in the lowest energy band in the first Brillouin zone.

The data in Fig. 5.13 (b) indicate a momentum oscillation of the BEC and clearly show the mirror effect of the optical lattice when the BEC momentum reaches $+p_{\mathrm{rec}}$. In addition, the data demonstrate that it is possible for the BEC to oscillate more than once. Based on the above observations, the optical lattice with a magnetic trap works as an atom cavity.

To characterize this Bragg-reflecting atom cavity, we apply different Z-trap displacements. Since the BEC will experience different forces at different locations in the Z-trap, the atoms will reach $+p_{\mathrm{rec}}$ at different times, leading to a change in oscillation frequency of the atoms. In the experiment, the BEC is placed 30 μm, 44 μm, 60 μm and 74 μm away from the center of the Z-trap. The corresponding

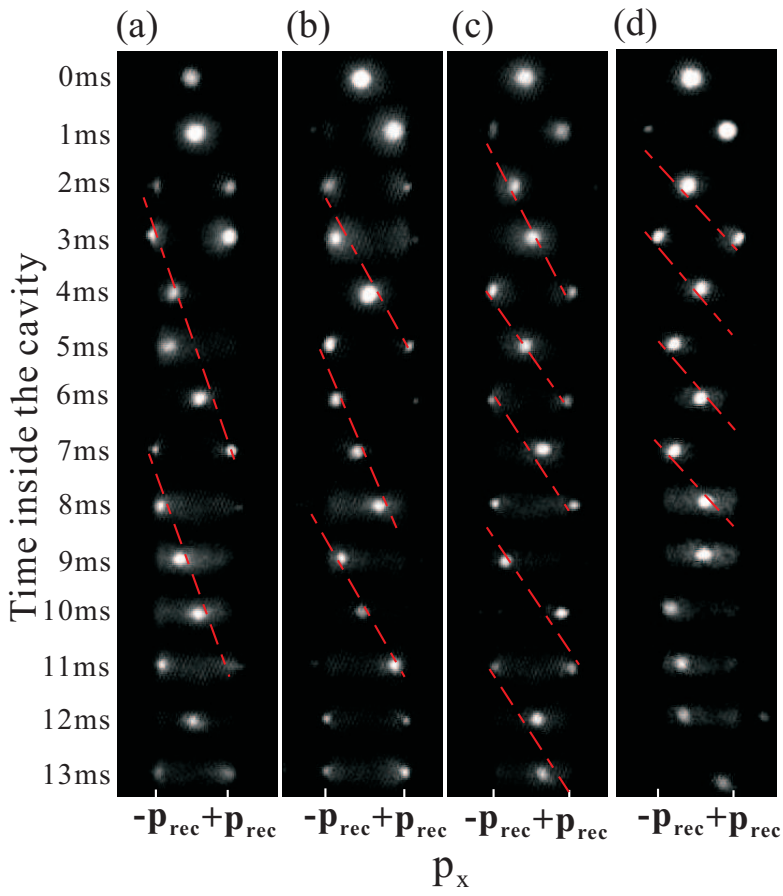

Figure 5.15: Momentum distribution of the BEC inside the atom cavity (linear gray-scale representation). The BEC is initially displaced by different amounts from the center of the Z-trap. (a)-(d) correspond to 30 μm, 44 μm, 60 μm and 74 μm displacements, respectively.

data are shown in Fig. 5.15 (a)-(d), respectively. As can be seen, the oscillation period decreases with increasing displacement. Qualitatively, this is because the BEC experiences a larger force farther away from the trap center, so it accelerates faster, taking less time to change its momentum from 0 to $+p_{\rm rec}$. As many as five oscillations are observed, as in Fig. 5.15 (c). Considering the regularity with which images containing both momentum components, $+p_{\rm rec}$ and $-p_{\rm rec}$, are seen in Fig. 5.15, we conclude that the Bragg reflection takes on the order of 1 ms, which is confirmed by simulation results presented later in the this section.

We calculate the oscillation period, T, based on the assumption that the optical lattice only acts as a Bragg mirror and does not affect the BEC elsewhere. There-

fore, $T/2$ corresponds to the time it takes for the BEC to accelerate to one recoil momentum in the Z-trap under the initial conditions that the BEC is stationary and located at a distance of x_0 from the center. For small x_0, as in this experiment, the Z-trap can be approximated by a harmonic potential, which leads to the following equation for the period T:

$$M\omega x_0 \sin\left(\omega\frac{T}{2}\right) = p_{\text{rec}} = \frac{h}{\lambda}, \tag{5.6}$$

where M is the atom mass, $\omega = 2\pi\times 45$ Hz is the frequency of the harmonic trap in the x-direction, and $\lambda = 852$ nm is the lattice-beam wavelength. Since

$$T = \frac{2}{\omega}\sin^{-1}\left(\frac{h}{M\omega x_0\lambda}\right) \simeq \left(\frac{2h}{M\omega^2\lambda}\right)\frac{1}{x_0} = \frac{A}{x_0}\,, \tag{5.7}$$

T approximately is a linear function of $1/x_0$ with a slope $A = 147$ ms μm.

Equation 5.7 can also be obtained by assuming that the Bloch oscillation occurs under constant force, $F_{\text{ext}} = \omega^2 M x_0$. In that case, the time derivative of the quasi-momentum, q, is given by $\hbar\dot{q} = F_{\text{ext}}$. The period T equals the time it takes for q to scan the first Brillouin zone, which has a full width of $4\pi/\lambda$. Therefore, $\dot{q} = 4\pi/(\lambda T)$, leading to Eq. 5.7.

From Fig. 5.15, we can measure T experimentally for different displacements x_0. The resulting period as a function of $1/x_0$ is plotted in Fig. 5.16. Also shown in Fig. 5.16 is a linear fit of the experimental data. The fit yields a slope of 137 ms μm. Based on the error bars of the data points, the uncertainty of the slope is estimated to be ± 15 ms μm. Within this uncertainty, experimental and theoretical values of the slope agree with each other.

We simulate the approximate BEC motion inside the cavity by solving the time-dependent 1-D Gross-Pitaevskii equation [82] using the Crank-Nicholson method (Appendix B). Figure 5.17 (a) shows the simulated momentum distribution with

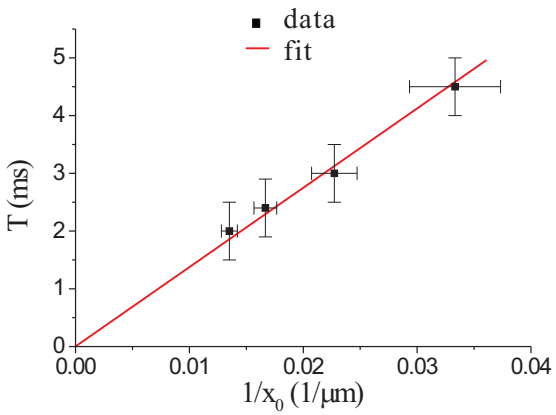

Figure 5.16: Oscillation period T as a function of $1/x_0$. A linear fit of the experimental data yields a slope of 137 ms μm.

parameters chosen to match the experimental conditions in Fig. 5.15 (b). The simulation reproduces the experimentally observed Bragg reflection and momentum oscillation of the BEC in the cavity; the experimental and simulated oscillation periods agree. Figure 5.17 (b) shows the simulated spatial distribution. During the Bragg reflection, a "standing-wave" is formed due to the interference between incoming and reflected wavefunction components. The duration of the Bragg reflections is of order 1 ms, in agreement with the experiment, and increases with successive Bragg reflections due to wavepacket dispersion.

A notable feature in Fig. 5.15 is that the momentum of the atoms appears to diffuse over the first Brillouin zone, $-p_{\rm rec} \leq p_{\rm x} \leq +p_{\rm rec}$, with no detectable diffusion beyond this range. There are several possible mechanisms for the diffusion. One mechanism is s-wave scattering of condensate atoms with opposite momenta during the Bragg reflection, when the BEC is split into two components, $|-p_{\rm rec}\hat{\mathbf{x}}\rangle$ and $|+p_{\rm rec}\hat{\mathbf{x}}\rangle$ ($\hat{\mathbf{x}}$ is the x unit vector). Since s-wave scattering amounts to processes of the type $|+p_{\rm rec}\hat{\mathbf{x}}\rangle + |-p_{\rm rec}\hat{\mathbf{x}}\rangle \rightarrow |-\mathbf{p}'\rangle + |+\mathbf{p}'\rangle$, where $|\mathbf{p}'| = p_{\rm rec}$, it generates a circular halo between the two momentum components. This halo spans the first

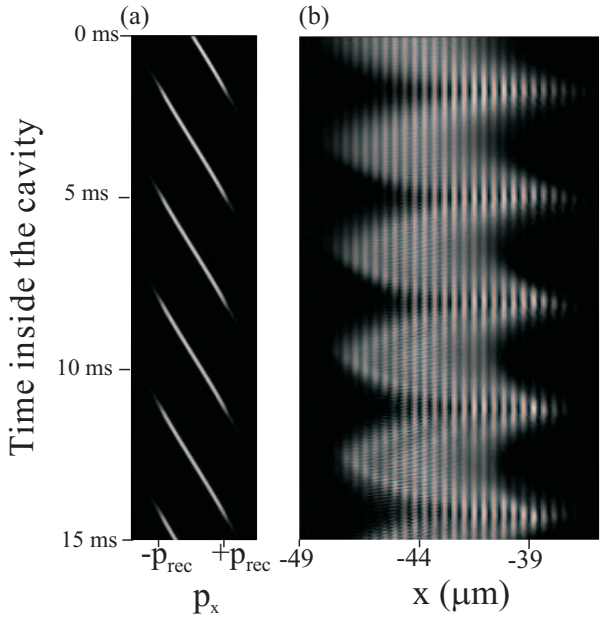

Figure 5.17: (a) Momentum distribution of the BEC inside the atom cavity obtained from the simulation (b) Corresponding wavefunction of the BEC.

Brillouin zone of the lattice and is sometimes observed at the first Bragg reflection. A second contributing factor is the dynamic instability of the BEC [83–85], which can be qualitatively explained as follows. The atom's effective mass is negative near the edges of the first Brillouin zone, where Bragg reflection occurs. Negative effective mass means an attractive force between condensate atoms, which leads to an instability of the BEC. Another diffusion mechanism is Landau instability [85] due to the BEC moving faster than the local sound speed. A fourth possible mechanism is the creation of solitons and vortices [48] by the Bragg reflection.

5.6 Superfluid to Mott-insulator Transition in a 1-D Optical Lattice

One of the most phenomenal accomplishments involving BECs in optical lattices is the observation of the quantum phase transition from superfluid to Mott-insulator. When adiabatically loaded into periodic potential wells created by optical lattices, BECs still maintain the long-range coherence if the potential depth of the lattice is

small. From another prospective, inside optical lattices condensate atoms localized around individual potential wells are connected through tunneling, which enables the atoms to possess a global phase. Thus, atoms are still in a superfluid state. However, when the lattice depth is increased, the tunneling rate decreases. At a certain point, condensate atoms can be considered isolated at each lattice site. Although atoms still occupy the lowest quantum state in each potential well, the whole atomic ensemble loses its long-range coherence. It is because the lowest quantum state in each lattice well now becomes a number state [12], which possesses a random phase. The resulting non-superfluid state is called Mott-insulator, in reference to a similar phenomenon in condensed matter physics.

The loss of the coherence in the Mott-insulator state is different from other decoherence mechanisms of BECs, such as thermal excitation. In fact, the lost coherence can be re-achieved through tunneling when the lattice depth is lowered back down. This phenomenon, in the case of a 1-D optical lattice, will be demonstrated in this section.

In the experiment, the BEC is first prepared in a magnetic trap with a 200 Hz frequency in the x-direction. Next, the lattice potential is ramped up from zero to its final value over 10 ms. This is realized using the amplitude modulation of an AOM. At its final value, the lattice is kept on for 5 ms before we simultaneously turn off the lattice and the magnetic trap, and take a TOF measurement (12 ms expansion). As can be seen in Fig. 5.18 (b), for small lattice depths the BEC is only slightly modulated by the lattice, corresponding to the appearance of only two weak side peaks, at $\pm 2\hbar k_{\mathrm{L}}$. As the depth of the lattice is increased, the transition to Mott insulator occurs. The typical signature of the transition is that the side peaks disappear and the central peak broadens, reflecting the momentum distribution of

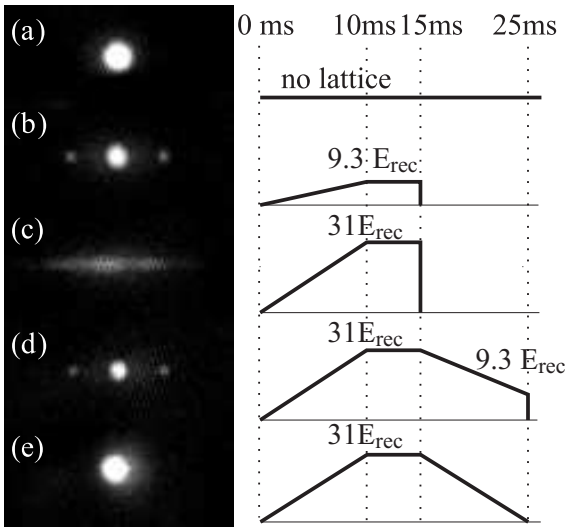

Figure 5.18: Left: TOF images. Right: lattice depth as a function of time for (a) BEC with no lattice, (b) superfluid phase, (c) 1-D Mott insulator, (d) superfluid phase recovered after Mott insulator, and (e) BEC with no lattice, recovered after Mott insulator.

the localized wavefunction in a single lattice well [12]. Here, we find that the system fully reaches the 1-D Mott insulator state around 30 E_{rec}.

The Mott insulator transition is a quantum phase transition, and thus is reversible; to be certain that we have seen the Mott transition, as opposed to a lattice-induced heating effect, we must show that we can reverse it. To demonstrate this, we ramp the lattice to 31 E_{rec} over 10 ms, hold it there for 5 ms, and then ramp back down over 10 ms. As can be seen in Figs. 5.18 (d) and (e), we obtain a modulated superfluid and BEC when we ramp down to a weak lattice and no lattice, respectively. Thus, the effect we see is fully reversible, providing strong evidence that it is the 1-D Mott insulator transition.

In the 1-D Mott-insulating state (Fig. 5.18 (c)), the quantum gas loses phase coherence in the direction of the optical lattice while retaining its superfluidity in the other two directions. The 1-D Mott insulator can thus be thought of as a stack of uncorrelated pancake BECs, each containing $\sim$3000 atoms under the conditions of Fig. 5.18 (c). As can be seen in Fig. 5.18 (c), the 1-D Mott insulator expands much

farther in the direction of insulation than in the directions of superfluidity. This is largely due to the momentum spread of the pancake BECs in the lattice-beam direction. Examining the TOF image in Fig. 5.18 (c), we find a velocity spread of $\Delta p/m_{\mathrm{Rb}} = 8$ mm/s. Using the Heisenberg uncertainty relation, $\Delta x \Delta p \geq \hbar/2$, this corresponds to a localization $\Delta x = 46$ nm, or 11% of the lattice period. Neglecting mean-field effects and using the fact that the lattice wells are approximately harmonic near their minima, we find an oscillation frequency of $2\pi \times 35$ kHz for a lattice with a depth of 30 E_{rec}, and velocity and position uncertainties of 8.9 mm/s and 41 nm, respectively, for the ground state. These numbers match the values derived from Fig. 5.18 (c) quite well, showing that the expansion in the lattice-beam direction is mostly driven by the kinetic energy of the pancake BECs in the optical-lattice wells.

A more subtle effect is that in the insulating case the expansion transverse to the lattice-beam direction is considerably slower than in the lattice-free BEC: about 1.5 mm/s and 2.5 mm/s, respectively. We attribute the difference to a variation in the manifestation of the repulsive mean-field potential (estimated to be $\lesssim 1$ kHz for our BECs in 200 Hz magnetic traps). Without the lattice, the BEC expansion is driven by a combination of the mean-field pressure and the kinetic energy of the BEC in the magnetic trap, leading to a final expansion speed of about 2.5 mm/s in all directions in Fig. 5.18 (a). After application of the deep, Mott-insulating lattice in Fig. 5.18 (c), the expansion is mostly driven by the comparatively high kinetic energy of the BEC pancakes in the optical-lattice wells, leading to a much faster expansion in the lattice direction. The faster expansion leads to a reduction of the time over which a substantial mean-field pressure exists, leading to a reduced final expansion speed transverse to the lattice, as observed.

5.7 Conclusion

In this chapter, BECs in far-detuned 1-D optical lattices are studied. Many interesting phenomena are observed, such as Kapitza-Dirac diffraction, thermal atom interference, atom interferometer, Bloch oscillation and the superfluid to Mott-insulator transition.

CHAPTER VI

Conclusions and Future Plans

6.1 Conclusions

In this thesis, I present work regarding cold neutral atoms in optical lattices. In the first half, a new type of optical lattice, which is referred to as a Raman Optical Lattice (ROL), is studied. When applied to laser-cooled ^{87}Rb atoms in a magneto-optic trap (MOT), the ROL drives Raman transitions between two ground states of the atoms and creates an atomic density distribution with a period of $\lambda/4$. This is a factor of two smaller than that of traditional optical lattices. We investigate this ROL scheme both theoretically (Chapter II) and experimentally (Chapter III). In the second half of the thesis, instead of cold thermal atoms, we load optical lattices with Bose-Einstein condensates (BEC). I first describe our work towards forming a BEC (Chapter IV) and then show several experiments involving BECs in optical lattices (Chapter V).

The thesis begins with a general introduction to optical lattices in Chapter I. Then in Chapter II, a reduced-period ROL configuration is proposed. The theoretical work shows that there is a novel sub-Doppler laser-cooling mechanism present in the ROL. The cooling prediction is based on a semi-classical treatment of the ROL, where the laser beams are regarded as classical fields and the internal levels

of the atoms are treated quantum-mechanically. The calculated friction force of the ROL is similar to that associated with the traditional Sysphus cooling. However, the cooling mechanism of the ROL is different. The ROL is further investigated from an approach of quantum Monte-Carlo wavefunction (QMCWF) simulations. The QMCWF simulation confirms the theoretical predictions about the ROL: a $\lambda/4$ periodicity and a sub-doppler laser cooling.

In Chapter III, the ROL is demonstrated experimentally. First, the sub-doppler cooling of the ROL is verified using a time-of-flight (TOF) method. From the TOF signal, the momentum distribution of the atoms cooled by the ROL is obtained and fitted to calculate the temperature of the atoms. The data show a temperature of about 8 μK, well below the doppler limit. Once the cooling effect is established, the ROL cooling is further characterized by investigating the cooling dependence on different lattice parameters. The experimental data agree well with the QMCWF simulations. In the second part of Chapter III, an optical-mask technique is used to probe density distributions of the atoms in optical lattices. The optical mask is applied to both a $\lambda/2$-period optical lattice and the ROL. The comparison between experimental data in these two cases yields a clear signature of the $\lambda/4$ periodicity of the ROL.

Chapter IV concerns the experimental setup to achieve the BEC. The BEC apparatus, including the vacuum chamber, the laser system, the timing-control system and the powersupply system, is discussed in detail. To achieve a BEC, ^{87}Rb atoms are first collected from the background vapor inside the primary chamber and then transported to the secondary chamber, where the vacuum pressure is three orders of magnitude lower. This pressure difference is maintained by a differential pumping stage. Inside the secondary chamber, the atoms are recaptured, compressed, fur-

ther cooled, optically pumped and eventually tranfered into an Ioffe-Pritchard type magnetic trap formed by a z-shaped current. Finally the BEC is achieved inside the z-trap after the forced RF evaporative cooling.

After the achievement of the BEC, in Chapter V, BECs in far-detuned 1-D optical lattices are studied. When a short and intense lattice pulse is applied to the BEC, Kapitza-Dirac diffraction is observed. The BEC is coherently split into several momentum components. Using Kapitza-Dirac diffraction, the interference of thermal atoms and an atom interferometer are realized. On the other hand, inside a long and weak optical lattice, the BEC behaves differently. With an additional force introduced by displacing the BEC from the center of the magnetic trap, the BEC undergoes Bloch oscillation. When the lattice depth is increased gradually, the BEC eventually loses its long-range coherence. However, the lost coherence can be recovered by gradually reducing the lattice depth. This famous quantum phase transition from the superfluid to Mott-insulator is also discussed in the case of a 1-D optical lattice.

6.2 Future Plans

In the future, it is planed to apply 2-D and 3-D optical lattices to BECs and study their consequent behaviors. Especially we are interested in the dependence of the superfluid to Mott-insulator transition on the dimensionality of the optical lattice.

We also would like to investigate the interaction between BECs and impurities. An interesting impurity is ions. It has been shown theoretically [49, 86, 87] that ions sparsely immersed into a BEC can capture up to several hundreds of condensate atoms. The captured atoms are in loosely bound states of a polarization potential induced by the ion.

Many aspects of this unique system can be explored experimentally, including the effective mass of ions in a BEC, spatial structures in the BEC wavefunction caused by the ion-BEC interaction, the rate of charge exchange of the ions with the surrounding BEC atoms and the effect of optical lattices on ions embedded in a BEC. Despite all these theoretical works and interesting subjects involved, this area is almost unexplored experimentally [88]. The main challenge of this ion-BEC experiment is the difficulty of minimizing the stray electric field around the BEC down to 2 mV/cm so that ions have an efficient interaction time with the BEC to cause any noticeable effect. Therefore, to study the ion-BEC interaction, the current BEC chamber will be modified to include compensation electrodes around the BEC. Furthermore, a microchannel plate (MCP) will be mounted inside the vacuum chamber for ion-detection.

APPENDICES

APPENDIX A

Branching Ratios of 87Rb D2-line

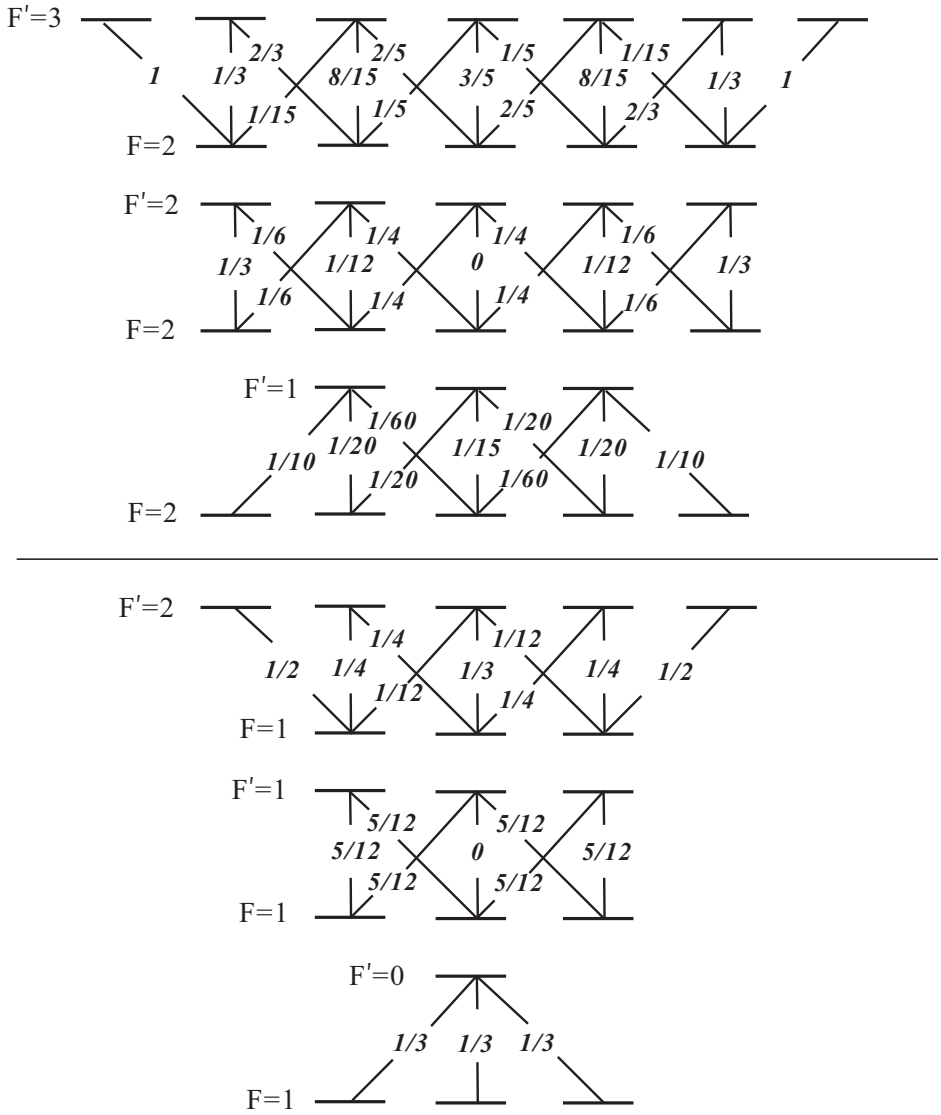

Figure A.1: Branching ratios for ^{87}Rb D2-line.

APPENDIX B

Crank-Nicholson Algorithm

We begin the discussion by writing down the time-dependent Schrödinger equation in one dimension

$$i\hbar\frac{\partial\psi(x,t)}{\partial t} = -\frac{\hbar^2}{2m}\frac{\partial^2\psi(x,t)}{\partial x^2} + V(x)\psi(x,t)\,. \tag{B.1}$$

We consider a spatial domain $x \in [a,b]$ with a boundary condition

$$\psi(a,t) = \psi(b,t) = 0\,. \tag{B.2}$$

The solution to the Schrödinger equation is uniquely determined given the initial wavefunction $\psi(x,0) = \Psi(x)$.

To obtain the solution numerically, we consider the wavefunction $\psi(x,t)$ on a regular grid of $\Delta x = (b-a)/N_x$ in space x and Δt in time t. The value of the wavefunction at a certain grid (j, k) is given by $\psi_j^{(k)} = \psi(a + j\Delta x, k\Delta t)$. The derivatives can then be replaced by finite differences:

$$\begin{aligned} \tfrac{\partial\psi(x,t)}{\partial t} &= \tfrac{\psi_j^{(k)} - \psi_j^{(k-1)}}{\Delta t} \text{ backward difference} \\ \text{or} &= \tfrac{\psi_{\mathrm{j}}^{(\mathrm{k}+1)} - \psi_{\mathrm{j}}^{(\mathrm{k})}}{\Delta \mathrm{t}} \text{ forward difference} \\ \tfrac{\partial^2\psi(x,t)}{\partial x^2} &= \tfrac{\psi_{j+1}^{(k)} + \psi_{j-1}^{(k)} - 2\psi_j^{(k)}}{\Delta x^2}\,. \end{aligned} \tag{B.3}$$

The right hand side of the Schrödinger equation then becomes

$$-\frac{\hbar^2}{2m\Delta x^2}(\psi_{j+1}^{(k)} + \psi_{j-1}^{(k)} - 2\psi_j^{(k)}) + V(a+j\Delta x)\psi_j^k = \sum_{m=0}^{N_x} H_{j,m}\psi_m^{(k)}\,, \tag{B.4}$$

where H is a tridiagonal matrix

$$H = \begin{pmatrix} \frac{\hbar^2}{m\Delta x^2} + V(a) & -\frac{\hbar^2}{2m\Delta x^2} & 0 & 0... & ...0 \\ -\frac{\hbar^2}{2m\Delta x^2} & \frac{\hbar^2}{m\Delta x^2} + V(a+\Delta x) & -\frac{\hbar^2}{2m\Delta x^2} & 0... & ...0 \\ 0 & -\frac{\hbar^2}{2m\Delta x^2} & \frac{\hbar^2}{m\Delta x^2} + V(a+2\Delta x) & -\frac{\hbar^2}{2m\Delta x^2} & ...0 \\ ... & ... & ... & ... & ... \\ ... & ... & ... & ... & ... \\ ... & ... & ... & ... & ... \end{pmatrix} \tag{B.5}$$

Combined with the left-hand site of the Schrödinger equation with a forward difference, we get

$$\psi^{(k+1)} = (1 - \frac{i}{\hbar} H\Delta t)\psi^{(k)}\,; \tag{B.6}$$

or, with a backward difference, we get

$$(1 + \frac{i}{\hbar} H\Delta t)\psi^{(k)} = \psi^{(k-1)}\,. \tag{B.7}$$

The average of Eq. B.6 and Eq. B.7 gives the Crank-Nicholson algorithm

$$(1 + \frac{i}{2\hbar} H\Delta t)\psi^{(k+1)} = (1 - \frac{i}{2\hbar} H\Delta t)\psi^{(k)}\,. \tag{B.8}$$

According to Eq. B.8, we can propagate the wavefunction forward in time steps of Δt, starting from the initial wavefunction $\Psi(x)$. Each propagation step involves solving a tridiagonal-matrix problem. Using LU decomposition, this problem can be efficiently solved. The Crank-Nicholson algorithm is a unitary operation in time, which assures that the wavefunction preserves its norm throughout the calculation.

BIBLIOGRAPHY

BIBLIOGRAPHY

[1] C. Salomon, J. Dalibard, A. Aspect, H. Metcalf, , and C. Cohen-Tannoudji. Channeling atoms in a laser standing wave. *Phys. Rev. Lett.*, 59(15):1659, 1987.

[2] G. Birkl, M. Gatzke, I. H. Deutsch, S. L. Rolston, and W. D. Phillips. Bragg scattering from atoms in optical lattices. *Phys. Rev. Lett.*, 75(15):2823, 1995.

[3] M. Weidemuller, A. Hemmerich, A. Gorlitz, T. Esslinger, and T. W. Honsch. Bragg diffraction in an atomic lattice bound by light. *Phys. Rev. Lett.*, 75(25):4583, 1995.

[4] Maxime Ben Dahan, Ekkehard Peik, Jakob Reichel, Yvan Castin, and Christophe Salomon. Bloch oscillations of atoms in an optical potential. *Phys. Rev. Lett.*, 76(24):4508, 1996.

[5] S. R. Wilkinson, C. F. Bharucha, K. W. Madison, Qian Niu, and M. G. Raizen. Observation of atomic Wannier-Stark ladders in an accelerating optical potential. *Phys. Rev. Lett.*, 76(24): 4512, 1996.

[6] G. Raithel, W. D. Phillips, and S. L. Rolston. Collapse and revivals of wave packets in optical lattices. *Phys. Rev. Lett.*, 81(17):3615, 1998.

[7] S. K. Dutta, B. K. Teo, and G. Raithel. Tunneling dynamics and gauge potentials in optical lattices. *Phys. Rev. Lett.*, 83(10):1934, 1999.

[8] D. L. Haycock, P. M. Alsing, I. H. Deutsch, J. Grondalski, and P. S. Jessen. Mesoscopic quantum coherence in an optical lattice. *Phys. Rev. Lett.*, 85(16):3365, 2000.

[9] Gavin K. Brennen, Carlton M. Caves, Poul S. Jessen, and Ivan H. Deutsch. Quantum logic gates in optical lattices. *Phys. Rev. Lett.*, 82(5):1060, 1999.

[10] D. Jaksch, H.-J. Briegel, J. I. Cirac, C. W. Gardiner, and P. Zoller. Entanglement of atoms via cold controlled collisions. *Phys. Rev. Lett.*, 82(9):1975, 1999.

[11] C. Monroe. Quantum information processing with atoms and photons. 416(0):238, 2002.

[12] M. Greiner, O. Mandel, T. Esslinger, T. W. Hansch, and I. Bloch. Quantum phase transition from a superfluid to a mott insulator in a gas of ultracold atoms. 415(0):39, 2002.

[13] G. Grynberg and C. Robilliard. Cold atoms in dissipative optical lattices. *Physics Reports*, 355(5-6):335, 2001.

[14] P. R. Berman, G. Raithel, R. Zhang, and V. S. Malinovsky. Sub-doppler cooling in reduced-period optical lattice geometries. *Phys. Rev. A*, 72(3):033415, 2005.

[15] P. R. Berman, B. Dubetsky, and J. L. Cohen. High-resolution amplitude and phase gratings in atom optics. *Phys. Rev. A*, 58(6):4801, 1998.

[16] B. Dubetsky and P. R. Berman. $\lambda/4$, $\lambda/8$, and higher order atom gratings via Raman transitions.

[17] B. Dubetsky and P. R. Berman. $\lambda/8$-period optical potentials. *Phys. Rev. A*, 66(4):045402, 2002.

[18] M. Weitz, G. Cennini, G. Ritt, and C. Geckeler. Optical multiphoton lattices. *Phys. Rev. A*, 70(4):043414, 2004.

[19] V. Finkelstein, P. R. Berman, and J. Guo. One-dimensional laser cooling below the doppler limit. *Phys. Rev. A*, 45(3):1829, 1992.

[20] J. Dalibard, Y. Castin, and K. Molmer. Wave-function approach to dissipative processes in quantum optics. *Phys. Rev. Lett.*, 68(5):580, 1992.

[21] P. Marte, R. Dum, R. Taieb, and P. Zoller. Resonance fluorescence from quantized one-dimensional molasses. *Phys. Rev. A*, 47(2):1378, 1993.

[22] W. Demtroder. Laser sectroscopy. *Springer, New York, NY, 2nd edition*, 1998.

[23] P. D. Lett, R. N. Watts, C. I. Westbrook, W. D. Phillips, P. L. Gould, and H. J. Metcalf. Observation of atoms laser cooled below the doppler limit. *Phys. Rev. Lett.*, 61(2):169, 1988.

[24] S. K. Dutta, N. V. Morrow, and G. Raithel. Enhancement of sisyphus cooling using a bichromatic standing wave. *Phys. Rev. A*, 62(3):035401, 2000.

[25] P. S. Jessen and I. H. Deutsch. Optical lattices. *Adv. At. Mol. Phys.*, 37:95, 1996.

[26] V. Finkelstein, P. R. Berman, and J. Guo. One-dimensional laser cooling below the doppler limit. *Phys. Rev. A*, 45(3):1829, 1992.

[27] Jun Guo and Paul R. Berman. One-dimensional laser cooling with linearly polarized fields. *Phys. Rev. A*, 48(4):3225, 1993.

[28] B. Sheehy, S-Q. Shang, P. van der Straten, S. Hatamian, and H. Metcalf. Magnetic-field-induced laser cooling below the doppler limit. *Phys. Rev. Lett.*, 64(8):858, 1990.

[29] G. Raithel, G. Birkl, A. Kastberg, W. D. Phillips, and S. L. Rolston. Cooling and localization dynamics in optical lattices. *Phys. Rev. Lett.*, 78(4):630, 1997.

[30] Andrey Turlapov, Alexei Tonyushkin, and Tycho Sleator. Optical mask for laser-cooled atoms. *Phys. Rev. A*, 68(2):023408, 2003.

[31] Alexei Tonyushkin and Tycho Sleator. Direct imaging of periodic subwavelength patterns generated by optical phase masks. *Phys. Rev. A*, 74(5):053615, 2006.

[32] Andrey Turlapov, Alexei Tonyushkin, and Tycho Sleator. Talbot-Lau effect for atomic de Broglie waves manipulated with light. *Phys. Rev. A*, 71(5):043612, 2005.

[33] R. Zhang, N. V. Morrow, P. R. Berman, and G. Raithel. Laser cooling in an optical lattice that employs Raman transitions. *Phys. Rev. A*, 72(4):043409, 2005.

[34] R. Zhang, R. E. Sapiro, N. V. Morrow, and G. Raithel. Transition of laser cooling between standard and Raman optical lattices. *Phys. Rev. A*, 74(3):033404, 2006.

[35] R. Zhang, N.V. Morrow, R.E. Sapiro, P.R. Berman, and G. Raithel. Analysis of atomic density distributions in optical lattices using an optical mask. *Opt. Comm.*, 275(2):311, 2007.

[36] M.H. Anderson, J.R. Ensher, M.R. Matthews, C.E. Wieman, and E.A. Cornell. Observation of Bose-Einstein condensation in a dilute atomic vapor. *Science*, 269(5221):198, 1995.

[37] K.B. Davis, M.-O. Mewes, M.R. Andrews, N.J. van Druten, D.S. Durfee, D.M. Kurn, and W. Ketterle. Bose-Einstein condensation in a gas of sodium atoms. *Phys. Rev. Lett.*, 75(22): 3969, 1995.

[38] C.C. Bradley, C.A. Sackett, J.J. Tollett, and R.G. Hulet. Evidence of Bose-Einstein condensation in an atomic gas with attractive interactions. *Phys. Rev. Lett.*, 75(9):1687, 1995. *ibid.* **79**, 1170 (1997).

[39] V. Bagnato, D. E. Pritchard, and D. Kleppner. Bose-Einstein condensation in an external potential. *Phys. Rev. A*, 35(10):4354, May 1987.

[40] E. P. Gross. Structure of quantized vortex. *Nuovo. Cimento*, 20:454, 1961.

[41] L. P. Pitaevskii. Vortex lines in an imperfect Bose gas. *Zh. Eksp. Teor. Fiz.*, 40:646, 1961.

[42] Mark Edwards, R. J. Dodd, C. W. Clark, P. A. Ruprecht, and K. Burnett. Properties of a Bose-Einstein condensate in an anisotropic harmonic potential. *Phys. Rev. A*, 53(4):1950, 1996.

[43] M. Holland and J. Cooper. Expansion of a Bose-Einstein condensate in a harmonic potential. *Phys. Rev. A*, 53(4):1954, 1996.

[44] R. J. Dodd, Mark Edwards, C. J. Williams, C. W. Clark, M. J. Holland, P. A. Ruprecht, and K. Burnett. Role of attractive interactions on Bose-Einstein condensation. *Phys. Rev. A*, 54 (1):661, 1996.

[45] R. Dum, J. I. Cirac, M. Lewenstein, and P. Zoller. Creation of dark solitons and vortices in Bose-Einstein condensates. *Phys. Rev. Lett.*, 80(14):2972, 1998.

[46] Kirstine Berg-Sorensen and Klaus Molmer. Bose-Einstein condensates in spatially periodic potentials. *Phys. Rev. A*, 58(2):1480, 1998.

[47] Dae-Il Choi and Qian Niu. Bose-Einstein condensates in an optical lattice. *Phys. Rev. Lett.*, 82(10):2022, 1999.

[48] R. G. Scott, A. M. Martin, T. M. Fromhold, S. Bujkiewicz, F. W. Sheard, and M. Leadbeater. Creation of solitons and vortices by bragg reflection of Bose-Einstein condensates in an optical lattice. *Phys. Rev. Lett.*, 90(11):110404, 2003.

[49] P. Massignan, C. J. Pethick, and H. Smith. Static properties of positive ions in atomic Bose-Einstein condensates. *Phys. Rev. A*, 71(2):023606, 2005.

[50] D. S. Jin, J. R. Ensher, M. R. Matthews, C. E. Wieman, and E. A. Cornell. Collective excitations of a Bose-Einstein condensate in a dilute gas. *Phys. Rev. Lett.*, 77(3):420, 1996.

[51] M.-O. Mewes, M. R. Andrews, N. J. van Druten, D. M. Kurn, D. S. Durfee, C. G. Townsend, and W. Ketterle. Collective excitations of a Bose-Einstein condensate in a magnetic trap. *Phys. Rev. Lett.*, 77(6):988, 1996.

[52] S. Inouye, M. R. Andrews, J. Stenger, H.-J. Miesner, D. M. Stamper-Kurn, and W. Ketterle. Observation of Feshbach resonances in a Bose-Einstein condensate. *Nature*, 392(6672):151, 1998.

[53] Ph. Courteille, R. S. Freeland, D. J. Heinzen, F. A. van Abeelen, and B. J. Verhaar. Observation of a feshbach resonance in cold atom scattering. *Phys. Rev. Lett.*, 81(1):69, 1998.

[54] M. R. Matthews, B. P. Anderson, P. C. Haljan, D. S. Hall, C. E. Wieman, and E. A. Cornell. Vortices in a Bose-Einstein condensate. *Phys. Rev. Lett.*, 83(13):2498, 1999.

[55] M. R. Andrews, C. G. Townsend, H.-J. Miesner, D. S. Durfee, D. M. Kurn, and W. Ketterle. Observation of interference between two bose condensates. *Science*, 275(5300):637, 1997.

[56] O. Morsch and M. Oberthaler. Dynamics of Bose-Einstein condensates in optical lattices. *Rev. Mod. Phys.*, 78(1):179, 2006.

[57] S. Gupta, K. Dieckmann, Z. Hadzibabic, and D. E. Pritchard. Contrast interferometry using Bose-Einstein condensates to measure h/m and alpha. *Phys. Rev. Lett.*, 89(14):140401, 2002.

[58] T. Schumm, S. Hofferberth, L. M. Andersson, S. Wildermuth, S. Groth, I. Bar-Joseph, J. Schmiedmayer, and P. Kruger. Matter-wave interferometry in a double well on an atom chip. *Nature*, 1(1):57, 2005.

[59] Ying-Ju Wang, Dana Z. Anderson, Victor M. Bright, Eric A. Cornell, Quentin Diot, Tetsuo Kishimoto, Mara Prentiss, R. A. Saravanan, Stephen R. Segal, and Saijun Wu. Atom Michelson interferometer on a chip using a Bose-Einstein condensate. *Phys. Rev. Lett.*, 94(9):090405, 2005.

[60] O. Garcia, B. Deissler, K. J. Hughes, J. M. Reeves, and C. A. Sackett. Bose-Einstein-condensate interferometer with macroscopic arm separation. *Phys. Rev. A*, 74(3):031601 (R), 2006.

[61] C. J. Myatt, E. A. Burt, R. W. Ghrist, E. A. Cornell, and C. E. Wieman. Production of two overlapping Bose-Einstein condensates by sympathetic cooling. *Phys. Rev. Lett.*, 78(4):586, 1997.

[62] A. G. Truscott, K. E. Strecker, W. I. McAlexander, G. B. Partridge, and R. G. Hulet. Observation of Fermi pressure in a gas of trapped atoms. *Science*, 291(5513):2570, 2001.

[63] K. Xu, T. Mukaiyama, J. R. Abo-Shaeer, J. K. Chin, D. E. Miller, and W. Ketterle. Formation of quantum-degenerate sodium molecules. *Phys. Rev. Lett.*, 91(21):210402, 2003.

[64] H. J. Lewandowski, D. M. Harber, D. L. Whitaker, and E. A. Cornell. Simplified system for creating a BosecEinstein condensate. *Journal of Low Temperature Physics*, 132(516):309, 2003.

[65] A. Camposeo, A. Piombini, F. Cervelli, F. Tantussi, F. Fuso, and E. Arimondo. A cold cesium atomic beam produced out of a pyramidal funnel. *Opt. Comm.*, 200(1-6):231, 2001.

[66] M. A. Clifford, G. P. T. Lancaster, R. H. Mitchell, F. Akerboom, and K. Dholakia. Realization of a mirror magneto-optical trap. *Journal of Modern Optics*, 48(6):1123, 2001.

[67] Albrecht Haase, Donatella Cassettari, Bjorn Hessmo, and Jorg Schmiedmayer. Trapping neutral atoms with a wire. *Journal of Modern Optics*, 64(4):043405, 2001.

[68] S. Schneider, A. Kasper, Ch. vom Hagen, M. Bartenstein, B. Engeser, T. Schumm, I. Bar-Joseph, R. Folman, L. Feenstra, and J. Schmiedmayer. Bose-Einstein condensation in a simple microtrap. *Phys. Rev. A*, 67(2):023612, 2003.

[69] A. Kasper, S. Schneider, Ch. vom Hagen, M. Bartenstein, B. Engeser, T. Schumm, I. Bar-Joseph, R. Folman, L. Feenstra, and J. Schmiedmayer. A Bose-Einstein condensate in a microtrap. *J. Opt. B*, 5(2):S143, 2003.

[70] R. A. Nyman, G. Varoquaux, B. Villier, D. Sacchet, F. Moron, Y. Le Coq, A. Aspect, and P. Bouyer. Tapered-amplified antireflection-coated laser diodes for potassium and rubidium atomic-physics experiments. *Rev. Sci. Instrum.*, 77(3):033105, 2006.

[71] M. Kozuma, L. Deng, E. W. Hagley, R. Lutwak J. Wen, K. Helmerson, S. L. Rolston, and W. D. Phillips. Coherent splitting of Bose-Einstein condensed atoms with optically induced Bragg diffraction. *Phys. Rev. Lett.*, 82(5):871, 1999.

[72] O. Morsch, J. H. Mller, M. Cristiani, D. Ciampini, and E. Arimondo. Bloch oscillations and mean-field effects of Bose-Einstein condensates. *Phys. Rev. Lett.*, 87(14):140402, 2001.

[73] T. Stoferle, H. Moritz, C. Schori, M. Kohl, and T. Esslinger. Transition from a strongly interacting 1d superfluid to a mott insulator. *Phys. Rev. Lett.*, 92(13):130403, 2004.

[74] I. B. Spielman, W. D. Phillips, and J.V. Porto. Mott-insulator transition in a two-dimensional atomic bose gas. *Phys. Rev. Lett.*, 98(8):080404, 2007.

[75] C. Sias, A. Zenesini, H. Lignier, S. Wimberger, D. Ciampini, O. Morsch, and E. Arimondo. Resonantly enhanced tunneling of Bose-Einstein condensates in periodic potentials. *Phys. Rev. Lett.*, 98(12):120403, 2007.

[76] B. P. Anderson and M. A. Kasevich. Macroscopic quantum interference from atomic tunnel arrays. *Science*, 282(5394):1686, 1998.

[77] Yu. B. Ovchinnikov, J. H. Muller, M. R. Doery, E. J. D. Vredenbregt, K. Helmerson, S. L. Rolston, and W. D. Phillips. Diffraction of a released Bose-Einstein condensate by a pulsed standing light wave. *Phys. Rev. Lett.*, 83(2):284, 1999.

[78] D. E. Miller, J. R. Anglin, J. R. Abo-Shaeer, K. Xu, J. K. Chin, and W. Ketterle. High-contrast interference in a thermal cloud of atoms. *Phys. Rev. A*, 71(4):043615, 2005.

[79] Michael P. Marder. *Condensed Matter Physics.* John Wiley & Sons, Inc., 2000 edition.

[80] Maxime Ben Dahan, Ekkehard Peik, Jakob Reichel, Yvan Castin, and Christophe Salomon. Bloch oscillations of atoms in an optical potential. *Phys. Rev. Lett.*, 76(24):4508, 1996.

[81] O. Morsch, J. H. Mller, M. Cristiani, D. Ciampini, and E. Arimondo. Bloch oscillations and mean-field effects of Bose-Einstein condensates in 1d optical lattices. *Phys. Rev. Lett.*, 87(14): 140402, 2001.

[82] Sadhan K. Adhikari. Collapse of attractive Bose-Einstein condensed vortex states in a cylindrical trap. *Phys. Rev. E*, 65(9):016703, 2001.

[83] S. Burger, F. S. Cataliotti, C. Fort, F. Minardi, M. Inguscio, M. L. Chiofalo, and M. P. Tosi. Superfluid and dissipative dynamics of a Bose-Einstein condensate in a periodic optical potential. *Phys. Rev. Lett.*, 86(20):4447, May 2001.

[84] J. C. Bronski, L. D. Carr, B. Deconinck, J. N. Kutz, and K. Promislow. Stability of repulsive Bose-Einstein condensates in a periodic potential. *Phys. Rev. E*, 63(3):036612, 2001.

[85] Biao Wu and Qian Niu. Landau and dynamical instabilities of the superflow of Bose-Einstein condensates in optical lattices. *Phys. Rev. A*, 64(6):061603 (R), 2001.

[86] R. Cote, V. Kharchenko, and M. D. Lukin. Mesoscopic molecular ions in Bose-Einstein condensates. *Phys. Rev. Lett.*, 89(9):093001, 2002.

[87] Hao Fu and A. G. Rojo. Tonks-Girardeau gas in an optical lattice: Effects of a local potential. *Phys. Rev. A*, 74(1):013620, 2006.

[88] D. Ciampini, M. Anderlini, J. H. Muller, F. Fuso, O. Morsch, J. W. Thomsen, and E. Arimondo. Photoionization of ultracold and Bose-Einstein-condensed Rb atoms. *Phys. Rev. A*, 66(4): 0043409, 2002.